DCT 257

Holistic Rehabilitation of Fatigue-Cracks in Steel Bridge Members Using Carbon Nanotube-Based Composites: A Feasibility Study

By

Jordan Wynn
Shafique Ahmed
Thomas Schumacher (PI)
Jennifer McConnell (Co-PI)
Erik Thostenson (Co-PI)

May, 2016

Delaware Center for Transportation
University of Delaware
355 DuPont Hall
Newark, Delaware 19716
(302) 831-1446

The Delaware Center for Transportation is a university-wide multi-disciplinary research unit reporting to the Chair of the Department of Civil and Environmental Engineering, and is co-sponsored by the University of Delaware and the Delaware Department of Transportation.

DCT Staff

Christopher Meehan *Director*	Jerome Lewis *Associate Director*

Ellen Pletz *Business Admin I*	Earl “Rusty” Lee *T^2 Program Coordinator*	Matheu Carter *T^2 Engineer*	Sandra Wolfe *Event Coordinator*	Mingxin Li *Scientist*

The research reported in this document was prepared through participation in an Agreement sponsored by the State of Delaware’s Department of Transportation and the Federal Highway Administration. The views and conclusions contained in this document are those of the author(s) and should not be interpreted as presenting the official policies or position, either expressed or implied, of the State of Delaware’s Department of Transportation or the U.S. Federal Government unless so designated by other authorized documents.

Delaware Center for Transportation
University of Delaware
Newark, DE 19716
(302) 831-1446

DelDOT Final Report

HOLISTIC REHABILITATION OF FATIGUE-CRACKS IN STEEL BRIDGE MEMBERS USING CARBON NANOTUBE-BASED COMPOSITES: A FEASIBILITY STUDY

Jordan Wynn
Shafique Ahmed
Thomas Schumacher (PI)
Jennifer McConnell (Co-PI)
Erik T. Thostenson (Co-PI)

May 2016
University of Delaware

TABLE OF CONTENTS

LIST OF TABLES

LIST OF EQUATIONS

LIST OF FIGURES

ABSTRACT

Nationwide, a significant amount of bridges within the National Bridge Inventory (NBI) have been found to develop fatigue cracks. Typically, section(s) in and surrounding welded connection details are particularly prone to the development of fatigue cracks as a result of the significant stress concentration. Existing flaws and/or discontinuities caused by notches, corners, welding toes etc., under the presence of tensile stresses will encourage the initiation and propagation of these cracks. Fatigue cracks found in bridge members can become potential areas of concern for bridge owners, as if not mitigated, continued cyclically applied loading to the bridge encourages the propagation of these cracks at these connection details. Ultimately, these cracks can lead to possible gross deformation, loss of function or serviceability, or complete separation of the component known as fracture. Although fatigue inherently does not always lead to fracture of a structural component, it must be considered as potential consequence of the development of fatigue cracks if not rehabilitated. As a result of this propagating issue, a holistic approach to the rehabilitation of cracks found in these steel bridge members has been developed and evaluated in the laboratory. This approach is based on an integrated strengthening and sensing (ISS) approach using composite materials in addition to a carbon nanotube (CNT)-based sensing layer in order to create a structural layer to be applied over a fatigue crack. This layer not only rehabilitates damaged sections but also continuously monitors its progress through use of the CNT sensing layer. If employed properly, this new methodology will inevitably decrease the overall stress concentration exhibited around the crack/crack mouth, which ultimately prolongs the general fatigue life of the structural member.

1 Introduction

1.1 Background

When subjected to repetitive loading conditions, many materials are prone to the development of what is known as fatigue cracks. These series of cracks have been found to be detrimentally to the overall strength and integrity of the material. The phenomena identified as fatigue, is a condition whereby a material cracks or fails attributed to recurring stresses applied below the ultimate strength of the material when loaded monotonically. When examined in the Civil Engineering discipline, fatigue is one of the primary reasons for the failure of structural components, particularly bridge structures. Commonly, many fatigue conditions occur in or around welded details due to the introduction of microstructure imperfections inherent with the welding process. Additionally, these cracks can develop at the focal location of discontinuities, typically from microstructure flaws and defects in the structure. All fatigue cracks have an associated stress concentration as a consequence of notches, corners, welding toes, etc. Research has shown there is a correlation between these concentrations of stress and the fatigue life.

As a result of continued cyclical loading, cracks will continue to propagate, ultimately leading to possible gross deformation, loss of function or serviceability, or complete separation of the component known as fracture. Although fatigue inherently does not always lead to fracture of a structural component, it must be considered as a potential consequence of the development of fatigue cracks, if not mitigated.

1.2 Problem Statement and Research Objective

Currently, bridges all throughout the country contain connection details that are susceptible to the development of fatigue cracks. The Delaware Department of Transportation (DelDOT) has a number of steel bridges in its inventory that have fatigue cracks such as the one shown in **Figure 1**. However, in spite of these continued deteriorating structural elements, measures can be taken to retrofit and preserve existing cracked bridge members if fatigue cracks are detected in early stages of propagation.

This project is part of a larger effort to develop an overall strategy for the rehabilitation and monitoring of fatigue-prone and deteriorated steel members, with the goal to prolong the life and safety of those bridges. Currently, there are a number of rehabilitation methods that are commonly employed in order to retard the propagation of these cracks. These techniques include but are not limited to: surface grinding of shallow cracks, drilling holes at the tips of cracks, welding of the cracks, metal reinforcements, reinforcements using composite materials, and/or modifying the connection details to decrease the stress concentration. Of these, the most commonly utilized procedure used by most bridge owners drilling a 2 to 3 in (51 to 76 mm) diameter hole at the end of the crack, a so-called crack-stop hole. The idea is that the stress concentration at the crack tip is decreased by simultaneously introducing a larger smooth curved surface into the stress field and removing the strain-hardened material. Once a crack-stop-hole is drilled, frequent inspections or monitoring are needed to ensure the procedure performs as intended. Even though this is common practice, there is currently no standard on how to precisely size these holes or how to maintain and inspect them. Furthermore, there is a lack of understanding of the conditions under which the holes are effective in stopping the fatigue crack from further propagating. This project is aimed at the development of an innovative holistic approach for the rehabilitation and monitoring of bridge members with fatigue cracks.

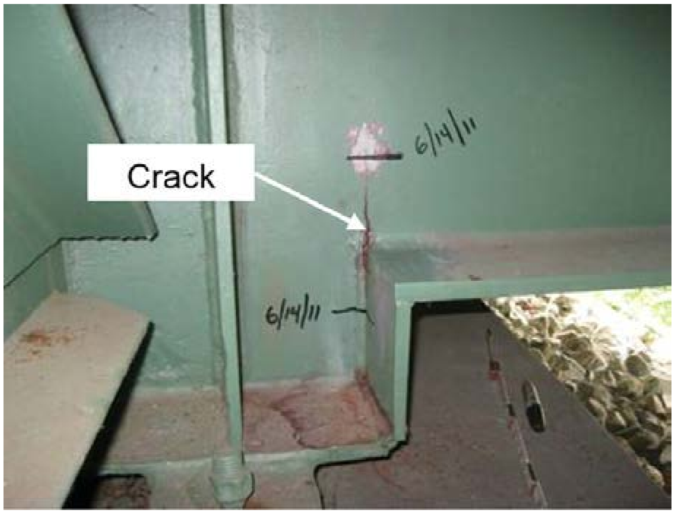

Figure 1. Sample fatigue crack developed on DelDOT steel bridge.

The focus of this investigation is on improving the fatigue lives of steel bridge members. This project explored and evaluated the use of a novel integrated rehabilitation and monitoring techniques employing structural carbon nanotube (CNT) infused sensing composites.

1.3 Overview of Approach

In order to develop a method to prolong the fatigue life of steel bridge members, this research was divided into two phases. The initial phase involved the recording of strain using a wireless sensing network (WSN) from ambient traffic on an in-service bridge. Data taken from bridge was subsequently analyzed in order to determine the current state of the structural member in question. The next phase involved laboratory testing incorporating the proposed holistic rehabilitation method. The overall purpose was to determine its effectiveness at prolonging the fatigue life of a damaged specimen.

In-service bridge monitoring was performed on DelDOT Bridge 1678-006. This structure was monitored for a period of just under two weeks. Four individual sampling sessions were carried out, each of which recorded about 48 hours of data. Conventional strain gauges were welded at various locations on the web near an existing fatigue crack. In addition, a neighboring girder with no fatigue damage was also instrumented in order to compare damaged vs. undamaged conditions. Upon culmination of sampling, data was analyzed in order to determine the fatigue life of the member. A number of cycle counting algorithms, including Rainflow and Simple Range counting methods, were employed as detailed in ASTM Standard E1049-85. These values could then be used in conjunction with Miner's Rule (Miner 1924) to estimate the cumulative damage (or remaining life) due to fatigue of the structure at each individual gauge location.

Laboratory fatigue testing was performed, adopting the approach set forth in the ASTM Standard E647. A standard single edge-notch compact (CT) specimen was employed as steel specimen for all laboratory testing. Per ASTM E647, a short fatigue crack was initiated prior to actual fatigue testing. Several tests were conducted; the first of which involved simple baseline testing of a CT specimen. The primary purpose of this test was to provide a reference against which to assess the progress and effectiveness of all other succeeding test specimens. Subsequent experiments involved testing a specimen with a drilled crack-stop hole, as employed in the field, the novel integrated structural sensing (ISS) patch, and a final specimen that had both a crack-stop hole and the novel ISS patch.

1.4 Organization of Report

This report is organized into five chapters. Chapter 1 provides a basic introduction to fatigue and fatigue cracking as it relates to steel bridge members. It also provides a statement of the problem that inevitably led to the subsequent research preformed. The justification as well as the objective of the study is described in this chapter.

Chapter 2 reviews past work performed on fatigue cracking in steel bridge members. Specific details pertaining to current rehabilitation practices employed in the field of civil engineering are highlighted. Moreover, the emerging innovative use of composite materials for the purpose of rehabilitating steel bridges is discussed. In addition, this chapter presents background information related to carbon nanotube-based sensing and its applications.

Chapter 3 describes all aspects related to experimental research performed for this study. The initial portion of this chapter focuses on the field monitoring of an in-service bridge and the components involved in the wireless sensing network (WSN) system employed. The instrumentation plan used is presented as well as the actual field installation of the strain gauges. The subchapters discuss the data analysis executed as well as the laboratory testing of the ASTM steel specimens. The purpose of this chapter is to provide step-by-step procedures as to the methodology engaged in this study.

Chapter 4 presents the findings from the field monitoring, data analysis and laboratory testing. Sample plots and tables of the data recorded throughout the length of the in-service monitoring period are also included herein.

Chapter 5 summarizes the results for the entire project and provides overall conclusions drawn from this investigation. General recommendations are described in reference to rehabilitation as well as possible concentration for future research involving rehabilitation of fatigue cracks in steel in bridge members.

2 Literature Review

2.1 Introduction

2.1.1 Fatigue Cracking

The development cracks in fatigue-prone regions is an issue that plagues a significant number of steel bridges throughout the nation and is a major concern when considering the continued safe operation of a bridge. According to 2014 current data gathered by the Federal Highway Administration (FHWA), nearly one-fourth of total of the bridges listed in National Bridges Inventory (NBI) inventory have been designated as structurally deficient and/or functionally obsolete (http://www.fhwa.dot.gov). The development of fatigue cracks has greatly contributed to the deterioration of these structures. The fundamental phenomenon behind the development of fatigue cracks in steel bridges is a direct result of cyclic loading. Typically, these cracks originate from welds which may cause stress concentrations. These cracks also develop as a result of an existing flaw under the presence of tensile stresses (Mertz 2012). These flaws are typically poor weld details that eventually initiate a crack when tensile stresses are applied or with the introduction of abrupt cross-sectional changes. As a result of repetitive loading, these microscopic cracks develop into macro cracks as they are continually loaded, and may further propagate. Fatigue crack propagation may eventually lead to fracture of the member and potentially to catastrophic failure of the structure for non-redundant structures. Bridges that are of this type or often referred to as fracture critical. As stated in the Clarification of Requirements for Fracture Critical Members, “fracture critical” bridge/structure is defined by the FHWA as a steel member in tension whose failure would result in possible section of or the entire bridge to collapse (Lwin 2012). This is due to lack of redundant elements in the structure. Although it is unlikely to cause collapse, any fracture is undesirable. Although some cracking may be tolerable, it is certainly not desired and requires close attention and action to be taken.

2.1.2 Rehabilitation

As fatigue cracking has the ability to lead to fracture or loss of serviceability if not mitigated, the cracks must be effectively rehabilitated in order to restore section to its full nominal properties. Numerous methods have been researched and employed to mitigate the propagation of fatigue cracking in steel bridge members. In some cases, particularly with redundant bridges, it has been found that the most effective method is to quite often simply monitor the crack rather than repair it (Dexter 2013). This is mainly true for bridges with cracking due to distortion induced fatigue. However, for bridges that have developed fatigue cracks as a result of typical cyclic loading, a number of methods exist that can be employed to rehabilitate a member.

Sections 2.2 and 2.3 present some commonly used rehabilitation methods. Additionally, a relatively new approach to repair fatigue cracks through the use of composite materials is discussed. These methods aim at extending the fatigue life for these structures. Some methods are strictly tailored to repairing fatigue details. While others’ intention is to improve fatigue resistance in order to prevent future fatigue cracking incidences. Nevertheless, each method has its own unique characteristics with a similar objective of improving the fatigue detail. Ultimately it is the responsibility of the individual to consider all methods and apply the procedure that will most effectively rehabilitate and extend the life of the structure for a given scenario.

2.2 Conventional Rehabilitation Methods

2.2.1 Current Rehabilitation Methods

The question of how to appropriately and effectively repair damaged girders/weld details/connections is a major concern for many bridge owners. There are currently various rehabilitation methods that are employed in different states that aim to reduce stress concentrations and/or cease the propagation of fatigue cracks, aiming to improve and increase the fatigue lives of these structures.

As discussed in the Federal Highway Administration's Manual for Repair and Retrofit of Fatigue Cracks in Steel Bridges, rehabilitation methods can be divided into three major retrofit techniques categories: (1) Surface treatments, (2) repairs of through-thickness cracks and (3) modification of the connection or the global structure to reduce the cause of cracking (Dexter 2013). Surface treatments are generally repair methods that can be described as "weld improvement" retrofits used to increase the fatigue strength of un-cracked welds. These include surface grinding, plasma re-melting of weld toe and impact treatments. Some examples of through-thickness cracks repairs are drilling holes, vee-and-weld, adding doubler/splice plates over crack and post-tensioning. Finally, Dexter's third major category is that of modification of the actual connection detail. Connection can be retrofitted and altered using a few different methods but inevitably that detail is altered in some matter in order to reduce stress in the joint (Dexter 2013).

2.2.1.1 Surface Treatments

Surface treatments to welds plagued with fatigue cracking issues can lead to a reduction in stress concentration and the elimination of discontinuities from which fatigue cracks propagate. Weld improvement techniques, such as toe grinding, have been shown to increase the fatigue life by a factor of two or more, equivalent to an increase in the allowable stress range of 30% (Rutherford 2006). In scenarios where cracks are located at the edges of flanges or other plates, grinding can be employed in order to completely remove portions of a detail containing small cracks. (Dexter 2013). The issue associated with grinding is that much confidence is placed in the operator. If not careful, the operator can remove too much material and/or gouge the material. In addition, grinding can only be used in order to rehabilitate 'shallow' cracks found to be less than 3 mm (0.118 in) in depth. Furthermore, extensive grinding can become an expensive repair method for bridges.

One of the easiest and least expensive surface treatments is hammer peening, which is a very effective and commonly used impact treatment. This method of impacting the surface allows for the introduction of compressive residual stress near the weld toe. These compressive residual stress "lower the effective tensile stress range locally on crack-like defect" (Dexter 2013). Peening is the process of working a metal's surface to improve its material properties, usually by mechanical means such as hammer blows. It tends to expand the surface of the cold metal, thereby inducing compressive stresses or relieving tensile stresses already present. Peening can also result in strain hardening of the surface metal. According to Branco (2004), air hammer peening is a reliable technique for repairing welds with shallow surface cracks up to 3 mm (0.118 in) in depth. Generally speaking, the depth of the crack refers to the distance through the thickness of the material that the crack has penetrated. Typically, this is the smallest of the three dimensions. While crack length refers to the actual extension of crack growth from end to end; commonly the greatest of the three dimensions of a body. For cracks with depths beyond 3 mm (0.118 in), only a very small increase in fatigue life was found. For crack depths above 5 mm (0.197 in), there is almost no benefit. Therefore, hammer peening is generally found to only be effective for cracks with depths below 2.5 mm (0.098 in). This study also found that a second hammer-peening treatment applied for repair of an existing crack does not provide any significant improvement in fatigue life.

Another quite effective impact treatment is ultrasonic impact treatment (UIT). Dexter states that UIT is considered one of the most effective methods for improving the reliability and fatigue strengths of welded joints (Dexter 2013). Similar to that of hammer peening, UIT introduces beneficial compressive residual stresses at the weld toe by plastic deformation of the surface and reduces stress concentration by smoothening of the weld toe profile (Gunther 2005). In Gunther's research this was performed by simultaneous mechanical hammering in order to deform the weld toe at a frequency of around 200 Hz and ultrasonic treatment at a frequency of 27 kHz. In comparison to hammer peening, UIT is less noisy and equipment is easier to handle. But with required equipment licensing agreements it tends to be more expensive than conventional hammer peening (Gunther 2005). Overall, there is a significant enhancement of the fatigue resistance by UIT compared to the as-welded state. Therefore, UIT can be considered as a viable rehabilitation method for shallow fatigue cracks particularly for high strength steels. Additional research into the effectiveness of the method on full-scale welded bridge girders is needed as UIT technology is still proprietary (Dexter 2013).

2.2.1.2 Through-Thickness Crack Repairs

As previously stated, fatigue cracks initiate from locations of high stress concentrations. These cracks continue to propagate as a result of repetitive loading and ultimately can penetrate the steel plate in the thickness direction (through the depth), commonly known as through-thickness cracks. Through-thickness cracking can be a result of typical, cyclic loading or out-of-plane bending known also as distortion-induced fatigue. Limited research has explored out-of-plane bending in reference to crack propagation behavior (Ju 2012). Nevertheless, some research has been conducted on methods that can be applied in order to rehabilitate bridges plagued with through-thickness fatigue cracking issues.

2.2.1.2.1 Crack-Stop Holes

The most common and widely used technique used to prevent the propagation of cracks in bridge girders is drilling crack-stop holes at the crack tips. The idea behind this technique is that by drilling the hole at the tip the stress concentration at the tip of the cracks are reduced and strain hardened material is removed. Thus the fatigue life of the bridge is extended. According to the *Manual for Repair and Retrofit of Fatigue Cracks in Steel Bridges*, in order for the hole to be sufficient enough to successfully arrest the crack the diameter needs to be 51 to 102 mm (2 to 4 in). Theoretically, the diameter of the hole required to arrest crack growth can be calculated from a formula developed by Rolfe and Barsom (1977), Fisher *et al.* (1980, 1990) and Dexter (2013). The relationship to determine the diameter of a crack-stop hole is based on linear-elastic fracture-mechanic theory, and as follows:

$$D = \frac{S_r \pi a}{8\sigma_y} \geq 1.0\ in \qquad \textbf{Equation 1}$$

In this equation, S_r is the nominal stress range where the crack tip is located, σ_y (ksi) is the yield stress of the material and a (inches) is the half-crack length (the distance between crack tips is $2a$) (Dexter 2013). The issue associated with using the above equation is that the equation often generates a hole diameter that is larger than what can be practically drilled. In addition, many owners are not comfortable with placing large holes in members. These limitations often result in undersized holes used in the field to arrest cracks (Crain 2010).

A viable solution to this problematic restriction is to strengthen these undersized crack-stop holes. This can be done in a number of ways, the most common being the use of cold expansion. The use of cold expansion allows for the incorporation of compressive residual stress around the hole. After the hole is drilled, a hammer is used to drive a tapered mandrel (also referred as a drift pin) that is slightly larger than the hole through it. This creates a compressive field as a result of the hole plastically deforming (Dexter 2013). Research conducted at the University of Kansas investigated the use of piezoelectric impact compressive kinetics (PICK) technique on ‘mild’ steels in order to determine its possibility to enhancement undersized, drilled crack-stop holes. “The PICK tool is used to apply a compressive pre-stress coupled with grain refinement around holes used to arrest fatigue cracks in steel bridges” (Crain 2010). Ultimately this study found that this tool has shown the ability to improve fatigue life of crack-stop holes by a factor of four than that of the untreated specimens. Further research in needed in order to design a new PICK tool for application in field conditions in addition to testing this tool on scaled bridge members subjected to a realistic crack-stop hole’s out of plane stress environment (Crain 2010).

In a similar investigation the effectiveness of drilled stop holes was explored. An innovative method that has previously been employed by the aerospace industry, that radially expands a high interference bushing into the hole, was employed. This method is intended to induce residual compressive stresses around the hole (Reid 2014). The magnitude of the residual stress was approximately equal to 2/3 of the tensile yield stress of the material (A36 steel with yield stress of

321 MPa (46.6 ksi) and tensile strength of 483 MPa (70.1 ksi)). Inducing these stresses around the hole theoretically is an effective way to prolong crack growth. Shown below in **Figure 2** is this proprietary procedure known as *StopCrackEx Process*. Seven dogbone-type specimens composed of A36 steel with a small initial 0.38 mm (0.015 in) starter notch for natural fatigue propagation were tested. Half the specimens were repaired employing the crack-stop hole drilling method and the other half with the new StopCrackEx process. Each specimen was cycled until a new crack initiated on the opposite side of the repair. Results showed at least a 12 times improvement in fatigue life for the new method compared to the conventional hole drilling method. In addition, an over 60 times fatigue life improvement was observed for one coupon specimen that was subsequently cycled to 20 million cycles with no evidence of any crack initiation. Ultimately both methods proved to be effective at retarding fatigue crack growth. But from the study, this new technique known as StopCrackEx demonstrated exceptional properties at completely discontinuing crack propagation in addition to long-term fatigue life improvements.

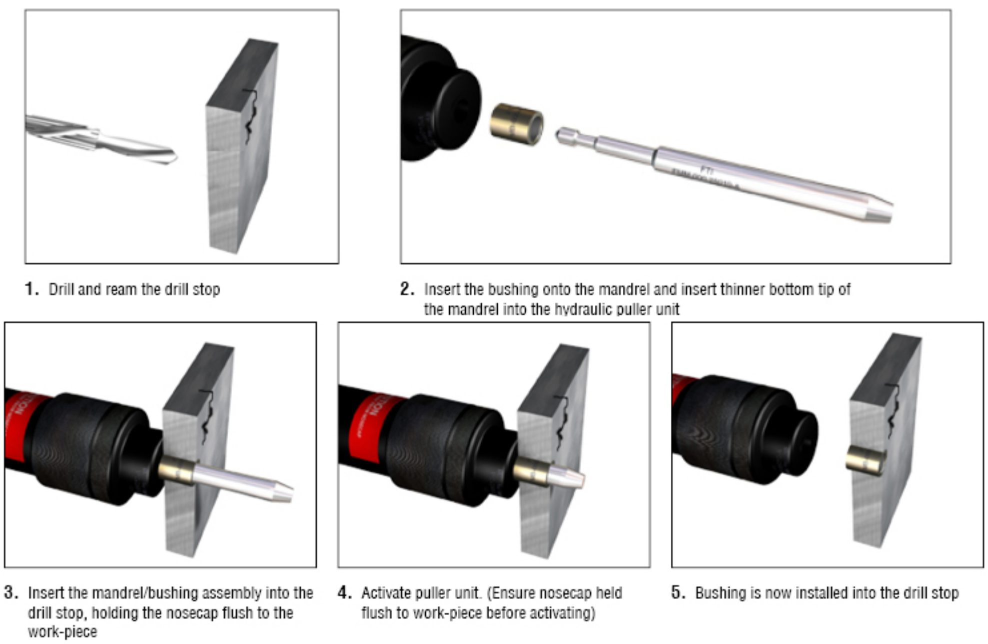

Figure 2. Schematic of StopCrackEx process (Source: fatiguetech.com).

2.2.1.2.2 Doubler and Splice Plates

The addition of doubler or splice plates is another through-thickness cracks repair. Adding doubler plates for fatigue crack repair essentially allows for additional cross-sectional area, which in turn results in reduces stress ranges (Dexter 2013). These plates are intended to restore the full cross-sectional properties of the uncracked girder. This method can be used in conjunction with weld repairs and crack-stop hole drilling as shown in **Figure 3**. The philosophy behind this is that this will ensure the weld repair will have adequate fatigue resistance. Doubler plates can be added after the repair is made. Ideally this will decrease the stress range that originally contributed to the development of cracking. An issue associated with this repair method is maintaining alignment of the two sides of the cracked section. “The cracked surface usually develops buckles, making alignment difficult” (Dexter 2013). Nevertheless, the addition of a doubler plate has been shown to improve fatigue crack life, particularly for full-depth cracks in bridge girders.

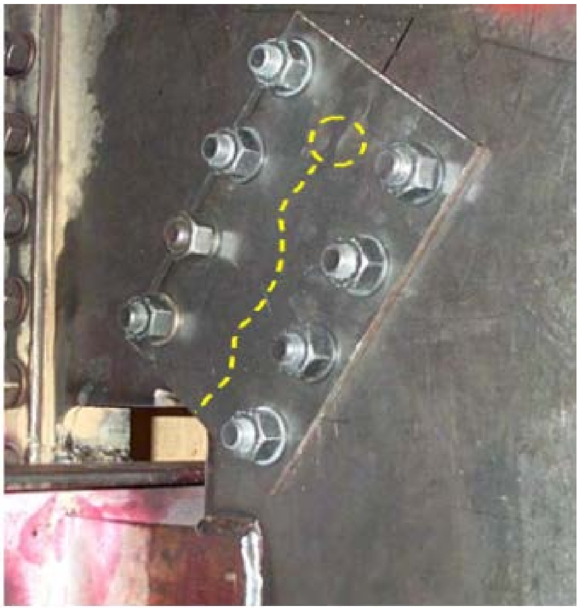

Figure 3. Bolted doubler plate repair. Dashed line represents crack beneath doubler plate and circle is the hole drilled to reduce the stress concentration at the crack tip (Source: Dexter 2013).

2.2.1.3 Connection Modification

Connection modification must be considered in cases where the rehabilitation method employed requires the stress ranges to first be decreased before the method can effectively repair the fatigue cracking issue. This could be done by through means of the addition of doubler plates or “introducing a soft-toe or radius” (Dexter 2013) in details compromised of sharp corners, as a means of decreasing local stresses. Although this can be extensive, it can result in a reduction of peak stresses in the joint and thus effectively correct the issue.

2.2.2 Conventional Methods Summary

Table 1 contains a comparison the previously discussed current rehabilitation methods. These are the most commonly employed techniques for fatigue crack repairs in the civil engineering industry.

Table 1. Comparison currently fatigue crack rehabilitation methods.

	Rehabilitation Method	Description/ Process	Advantages	Limitations
Surface Treatment	**Surface Grinding**	Use of a rotating abrasive wheel to smooth surface or totally remove portions of a detail containing small cracks	- Shown to increase fatigue life by factor of two or more - Could increase allowable stress ranges 30%	- Only applicable for shallow cracks (≤ 3 mm) - Extensive grinding can be expensive - Only viable for crack penetration ≤ 30% of plate thickness
	Hammer Peening	Use of mechanical means (hammer blows) to work a metal's surface to improve its material	- Easy - Inexpensive - Encourages strain hardening	- Only effective for shallow cracks (≤ 3mm)
	Ultrasonic Impact Treatment (UIT)	Cold mechanical treatment consisting of impacting surface to release tensions and add beneficial compressive stresses	- Automated - Effective - Less noisy than hammer blower - User friendly Equipment	- Requires equipment licensing agreements - More expensive than conventional hammer peening
Through-Thickness Repair	**Drilling Crack-Stop Holes**	Use of a circular drill bit in order to remove portion of material containing fatigue crack	- Quick and Simple - Removes stress concentration at crack tip	- Holes may be undersized - Hole must be precisely drilled
	Addition of Doubler or Splice Plates	Addition of plate over damaged portion in order to increase cross sectional area	- Can be used in conjunction with other techniques - Effective for full-depth cracks	- Difficult to maintaining alignment of two sides of cracked section

2.3 Composite Materials

A relatively new and innovative technique to address fatigue cracking issues in steel girders is the use of composite materials. These materials have mainly been used in aerospace and military applications but are beginning to emerge in civil engineering applications. When bonded to a surface, composites have the ability to stiffen and possibly extend the service life of deficient bridge girders. Fiber-reinforced polymer (FRP) composites have the advantage of high stiffness-to-weight and strength-to-weight ratios, superior environmental durability, fatigue resistance, flexibility, high chemical corrosion resistance, and ease of handle and maintenance (Karbhari 1995). As a result, they have been deemed a promising material to be used in structural rehabilitation. FRP composites consist of a polymer matrix material such as epoxy or polyester plastic reinforced with fibers made of, e.g. glass, carbon, or aramid. With their physical properties and endless conceivable ways in which to orient these fibers, composites have the ability to be tailored to specific material needs.

2.3.1 Fiber Reinforced Polymers (FRP)

Fiber reinforced polymers (FRP) (also known as fiber-reinforced plastic, and today as fiber reinforced composites) were not developed until the early 1940's (Tang 1997). Early applications began after World War II in the production of fiberglass for use in composite boat hulls and radar covers. The navy later began using these materials for pressure vessels in mine sweeping vessels, crew boats and submarine parts. In addition, composites began to emerge as a result of consumer demand for recreation products such as composite fishing rods, tennis rackets, ski equipment and golf clubs. The aerospace industry began to use composites in pressure vessels, containers, and non-structural aircraft components (Tang 1997). In 1968, composites were introduced into the civil engineering field in the form of a dome structure built in Benghazi.

FRPs are anisotropic where the stiffness and strength depends on the direction of the fibers. These fibers can be oriented in a variety on directions enabling composites to be tailored to the material/mechanical properties needed. The fibers can be chopped, woven, stitched, and/or braided (Tang 1997) to form sheets or fabrics. In order to obtain the desired strength and/or stiffness, several sheets can be laminated together.

As discussed by Benjamin Tang in the FHWA's article entitled *Fiber Reinforced Polymer Composite Applications in USA*, fiber reinforced polymer composites are composed of fiber reinforcements, resin, fillers, and additives. The fibers occupy between 30% and 70% of the matrix volume and have the ability to provide increased stiffness and tensile capacity. Fibers are bound together in a stable matrix through the resin which offers high compressive strength. The purposes of the fillers are to reduce cost and shrinkage. The additives assist in improvement to mechanical and physical properties of the composite. In addition, they help with workability (Tang 1997).

2.3.1.1 Reinforcing Fibers

The most common types of fibers used in advanced composites for structural applications are made of aramid, glass, and carbon. Composites based on these fibers have been used in numerous applications from planes and luxury vehicles to orthopedic products and fishing rods.

2.3.1.1.1 Aramid Fibers

Aramid fibers are strong synthetic fibers that are commonly used in aerospace and military applications, for ballistic rated body armor fabric and ballistic composites. In the civil engineering industry, the most common commercial grades used for structural applications are Kevlar 29 and Kevlar 49 (Tang 1997). These fibers have been found to have exceptional fatigue and creep resistance. Other properties include: abrasion resistance, non-conductivity, tremendously high melting point, low flammability, outstanding strength-to-weight ratio, high Young's Modulus (see **Table 2**), and high ultimate tensile strength. As a result, aramid fibers are good candidates for retrofitting materials.

Table 2. Aramid Fiber Material Properties (Source: Zweben 1989).

<table>
<tr><th colspan="2">Typical Properties</th><th>Kevlar 29</th><th>Kevlar 49</th></tr>
<tr><td rowspan="2">Density</td><td>(g/cm^3)</td><td>1.44</td><td>1.44</td></tr>
<tr><td>(lb/ft^3)</td><td>89.9</td><td>89.9</td></tr>
<tr><td rowspan="2">Young's Modulus</td><td>(GPa)</td><td>83/100</td><td>124</td></tr>
<tr><td>(ksi)</td><td>12,040/14,500</td><td>17,984</td></tr>
<tr><td rowspan="2">Tensile Strength</td><td>(GPa)</td><td>2.27</td><td>2.27</td></tr>
<tr><td>(ksi)</td><td>329</td><td>329</td></tr>
<tr><td colspan="2">Tensile Elongation (%)</td><td>2.80</td><td>1.80</td></tr>
</table>

2.3.1.1.2 Glass Fibers

Glass fibers have been found to be the least expensive of the three most commonly used fibers for civil engineering applications (Tang 1997). Three compositions of glass fibers are commonly used in composite materials: E-glass, S-glass and C-glass. The E-glass is elected for electrical uses while the S-glass for high strength. The C-glass is designated for high corrosion resistance, and it is generally uncommon for civil engineering applications. Among these three glass fibers, E-glass is the most common reinforcement material used in civil structures (Tang 1997). One of the drawbacks of glass fibers is that with increasing temperature, strength and stiffness decrease (Badawy 2012). Also, Young's modulus is relatively low compared to that of steel, which makes it ineffective for applications on steel. A summary of the material properties for glass fibers is presented in **Table 3**.

Table 3. Glass Fiber Material Properties (Source: Zweben 1989).

Typical Properties	E-Glass	S-Glass
Density (g/cm^3)	2.60	2.50
Young's Modulus (GPa)	72	87
Tensile Strength (GPa)	1.72	2.53
Tensile Elongation (%)	2.4	2.9

2.3.1.1.3 Carbon Fibers

As shown in **Table 4**, carbon fibers are divided into three main classifications: high strength, high modulus and ultra-high modulus. Similar to aramid fibers, carbon fibers have very high fatigue and creep resistance. Some of these properties include high strength-to-weight ratios and the ability to provide stiffness and strength. In addition, of the previously discussed fibers, carbon fiber is the most expensive.

Table 4. Carbon Fiber Material Properties (Source: Zweben 1989).

Typical Properties	High Strength	High Modulus	Ultra-High Modulus
Density (g/cm^3)	1.8	1.9	2.0 - 2.1
Young's Modulus (GPa)	230	370	520 - 620
Tensile Strength (GPa)	2.48	1.79	1.03 - 1.31
Tensile Elongation (%)	1.1	0.5	0.2

2.3.1.2 Composite Action

As previously stated, when a polymer matrix material is reinforced with one of these fibers, such as carbon fiber, composites are formed. For instance, carbon fiber-reinforced polymers (CFRP) are a subcategory of FRP that is composed of carbon fibers. In the civil engineering industry CFRP is most renowned for its use as a rehabilitation method for bridges. Its high strength-to-weight ratio make it quite useful in applications such as, increasing the load capacity of older under-designed structures, seismic retrofitting, and repair of damaged structure resulting from fatigue cracking (**Figure 4**).

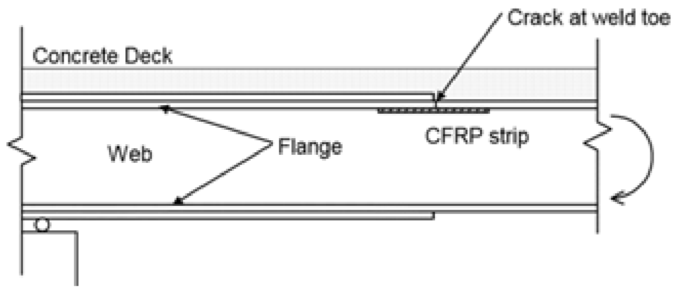

Figure 4. Rehabilitation of Fatigued Tension Flange with Bonded CFRP Strip (Source: Shield 2003).

Many researchers have examined the use of carbon fiber composites to rehabilitate steel bridges. In a 2001 study conducted at the University of Delaware, CFRP plates were tested in order to determine the effectiveness of strengthening steel bridge girders. The rehabilitation method developed consisted of bonding advanced composite material plates to the tension flange of steel bridge girders. The overall objective was to provide additional stiffness and strength (Miller 2001). Four full-scale 6.40 m (21 ft) long bridge girders were retrofitted and tested for effectiveness in the laboratory. These girders were rehabilitated with a single layer of CFRP bonded to inner and outer faces of tension flange and loaded in three-point bending to failure. In addition, two field load tests were performed (one before and one after CFRP rehabilitation) using loaded 3-axle dump trucks driving directly above the rehabilitated girder. Ultimately, this study found that the retrofit increased the elastic stiffness from 10% to 37% in the lab study and an 11.6% increase was found in the field testing. In addition, it was estimated that strain decreased by 10% as a result of the increased stiffness (Miller 2001).

From **Table 4** and research using CFRP strips, ultra-high modulus carbon fiber composites are suitable candidates for rehabilitation of steel structures. The carbon fibers, however, introduce the potential for reduction, which can result in corrosion due to galvanic interaction between steel and composite plates. In addition, composites are vulnerable when exposed to ultraviolet (UV) light, i.e. sunlight, as well as moisture. The UV radiation, as well as exposure to moisture, have been shown to develop adverse effects on the mechanical properties of the polymer matrix of the composite, resulting in the degradation of the composite. The actual carbon fibers however are not significantly affected by either environmental condition (Kumar 2002).

2.3.2 Debonding

Debonding and delamination are failure mechanisms that are associated with adhesives. Such failures, unless adequately considered, may significantly decrease the effectiveness of the strengthening approach. Debonding occurs when a reinforcing plate detaches from a parent member at the steel/adhesive interface shown in **Figure 5**. Typically, debonding of FRP strengthened members occurs in regions of high stress concentrations (Buyukozturk 2004). It is often associated with the presence of cracks. Finite element modeling has shown that deep cracks have been found to have a significantly higher strain energy release. This energy, as defined by Aggelopoulos, is a “measure of crack driving force” (Aggelopoulos 2011). It was established that this force increases as the modulus and thickness of composite patch are increased. In a similar study done in Italy by Colombi of Milan Technical University, sensitivity of debond crack strain energy release rate in relation to parameters such as patch stiffness, adhesive thickness and pretension level were investigated (Colombi 2003). Ultimately one conclusion drawn was that the strain energy release rate is not strongly dependent upon patch stiffness. This is mainly due to high stiffness of steel compared to CFRP. In addition, this study found that a thin adhesive layer produces a larger debonded area, which in return reduces the effectiveness of the reinforcement. Finally, the research was able to confirm that there is a fundamental contribution to effectiveness of the patch when it is pretensioned. Pretensioning the patch causes a compressive load applied to steel plate. This in return reduces the crack strain energy release rate (Colombi 2003). Also, there was a reduction in load transferred from the steel plate to the composite strip. Because the prestressed specimen stopped crack propagation and extend the fatigue life it can be concluded that “pretensioning of the composite patch prior to bonding is strongly recommended in order to maximize effectiveness of the bonded patch on the steel section” (Colombi 2003).

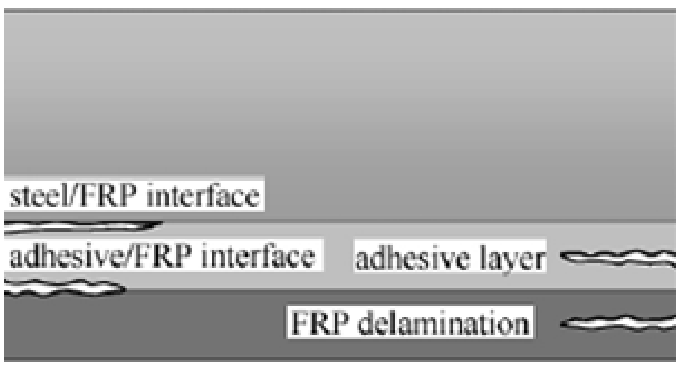

Figure 5. Types of debonding in FRP-strengthened steel members (Source: Buyukozturk 2004).

2.3.3 Adhesive Selection

The polymer matrix material (also referred to as resin) selected plays a significant role in the effectiveness of the composite strip to rehabilitate a bridge plagued with fatigue cracking. As discussed in the Federal Highway Administration's Proceedings of the First Korea/U.S.A. Road Workshop, the resins most commonly employed in composites are the “unsaturated polyesters, epoxies, and vinyl esters” (Tang 1997). In contrast, the least common resins used are the polyurethanes and phenolics.

As previously discussed, research conducted at the University of Delaware examined the used of carbon fiber-reinforced polymer (CRFP) plates to strengthen steel bridge girders. In this research two different adhesives were considered: a two-part high-strength epoxy (Araldite AV8113/HV811) and a methacrylate epoxy (ITW Plexus MA555). In order to select the appropriate adhesive, both shear strength and bond durability were considered. Bond durably must be accounted as these adhesives will be subjected to a number of environmental conditions that could inevitably affect the bond. These conditions include: deicing agents as well as chlorides from saltwater (Miller 2001).

These two structural adhesives, Ciba-Geigy AV8ll3/HV8l13 and Plexus M4555, were used in this rehabilitation project at the University of Delaware to enable examination of the in-field application and long-term durability of both. Each adhesive is applied to half of the tested girder as shown in **Figure 6** (Mertz 1996).

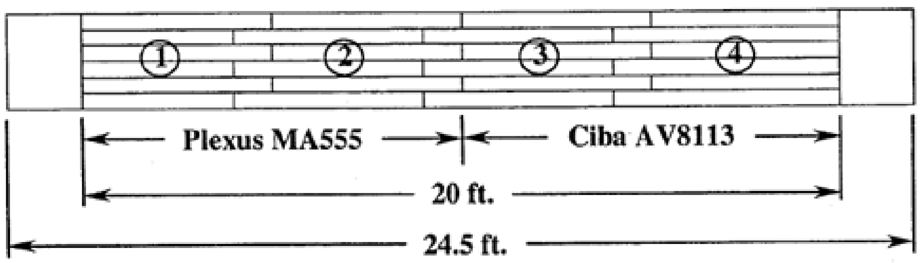

Figure 6. CFRP retrofit Scheme (Source Mertz 1996).

Shear strength results are shown below in **Table 5**. Aside from higher shear strength, Ciba-Geigy's AV8113 adhesive also displayed good durability under several environmental conditions including immersion in 65°C water, a commercial deicing agent, and freeze-thaw conditions (Mertz 1996). Although previous research has shown that either epoxy is acceptable, the Plexus M4555 was found to be more beneficial because of the relatively short cure time and low sensitivity to thick bond lines. This was determined in spite of the findings that Plexus MA555 adhesives have lower shear strength in comparison to Ciba-Geigy AV8113. But ultimately a reduced cure time allows for the bridge to be opened to normal traffic sooner, which limits the impact and significant concern to the public. In reference to the low sensitivity to thick bond lines, this allows for the CFRP plates to be placed over irregular surfaces, such as severely corroded girders, without sacrificing strength (1996).

Table 5. Experimental shear strength results.

Adhesive	Shear Strength (MPa)
Araldite AV8113/HV8113	13.8 - 17.2
Plexus MA555	8.6 - 10.3

2.4 Carbon Nanotube (CNT) Based Sensing

2.4.1 Background Information

As explored by University of Delaware professor Erik Thostenson, carbon nanotubes have been found to possess properties that enable them to functionalize composites. For example, they have the ability to provide real-time monitoring of damages developed in structural members. “The formation of a carbon nanotube network around the structural reinforcement in fiber composites has enabled *in situ* monitoring of matrix damage accumulations” (Gao 2009). In spite of this new found knowledge, only a limited amount of research has been explored on the use of carbon nanotube networks for structural health monitoring (SHM) of structures.

Carbon nanotubes (CNTs) can be viewed as a rolled sheet of graphite that is formed into a cylinder. These nanotubes can exist as either single-walled (SWCNT) or multi-walled (MWCNT) structures as shown in **Figure 7**. Multi-walled nanotubes are simply composed of a number single walled nanotubes held together with relatively weak van der Waals forces (Thostenson 2001). These hexagonal networks of carbon atoms are approximately 1 to 20 nm diameter and 1 to 100 microns in length.

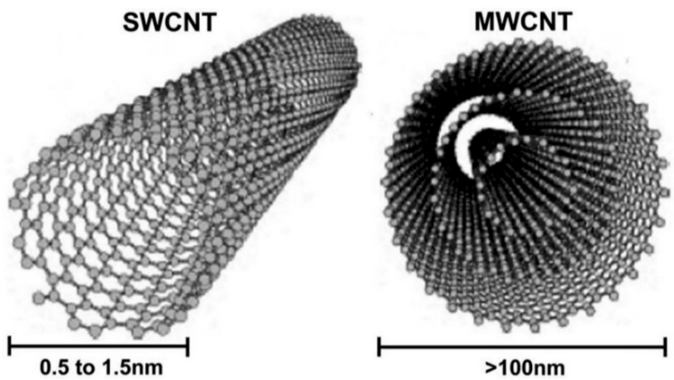

Figure 7. Carbon nanotube structures (Source: Martins-Júnior 2013).

2.4.2 Properties

In Thostenson's 2001 paper, research on several properties of CNTs including mechanical, electrical and thermal were reviewed. As a result of their symmetric structures, "these cage-like forms of carbon have been shown to exhibit exceptional material properties" (Thostenson 2001). Ultimately the review found that both theoretical and experimental results showed that CNTs have a particularly high Young's modulus. Results displayed values greater than 1000 GPa (145,000 ksi) which is comparable (if not greater) to that of diamond which possess a Young's modulus of about 1200 GPa (174,000 ksi). Furthermore, "strengths 10-100 times higher than the strongest steel at a fraction of the weight" were reported (Thostenson 2001). Assuming a Young's Modulus of 1250 GPa (181,000 ksi), the yield strength of closely packed nanotubes was demined to be greater than 45 ±7 GPa (6,527 ± 1015 ksi) by Walters of Rice University (Walter 1999). When compared to that of typical high-strength steels, this value is over 20 times greater. These findings further confirm the concept of carbon nanotube having astonishing mechanical properties.

In a 1999 study conducted by Jean-Paul Salvetat, elastic and shear moduli of single-walled carbon nanotubes (SWCNT) were explored. The inquiry concluded that as the diameter of the tube bundles increases, the axial and shear moduli drastically decrease (Salvetat 1999). This simply demonstrates the issue of slipping that can occur within the bundle of nanotubes.

In addition to the remarkably high Young's modulus of carbon nanotubes, they also possess exceptionally large elastic strain and fracture strain sustaining capability. Aside from the mechanical properties, Thostenson's paper also discussed the superior thermal and electrical properties associated with CNTs. Thermal conductivity was found to be twice as high as diamond while the electric-current carrying capacity is more than 1000 times higher than copper wires (Thostenson 2001). As stated by Zhidong Han, the "unusually high thermal conductivity makes CNTs the best promising candidate material for thermally conductive composites" (Han 2011). An example can be seen in the research conducted by Gao. In this 2009 research, a network of CNTs were applied for use in real-time monitoring of structural elements in order to detect damage development. CNT networks were formed around the structural reinforcements in fiber composites to enable this *in situ* monitoring. It was discovered that bulk conductivity changes occur when fibers break when the formation of matrix cracks prevents intra-fiber contacts (Gao 2009).

The mechanical properties in combination with the electrical properties make CNTs excellent candidates for *in situ* sensing. As a result, it has been reported that these nanotube-based materials have been employed as "electromechanical actuators and in a variety of sensing, applications, including mass sensors, humidity sensors, and strain sensors" (Thostenson 2006). But as previously stated, few studies have research the use of these sensors in applications of structural health monitoring. A study was conducted at the University of Delaware with the application of structural carbon nanotubes on concrete structures (Schumacher 2014). This research focused on the use of an integrated structural composite layer bonded to a concrete beam for distributed sensing. "This layer consisted of carbon nanotubes that are deposited on a carrier, which form a continuous conductive skin that is exceptionally sensitive to changes in strain and the formation of micro-damage and macro damage" (Schumacher 2014). The CNTs enables nerve-like distributed sensing capacities which allow for this damage detection. For this experiment a concrete beam measuring 53.3 cm (21 in) in length, 15.2 cm (6 in) in width and 15.2 cm (6 in) in depth were loaded in three-point bending. Prior to loading, the reinforcing composite sensing layer was fabricated and bonded using an epoxy resin to the bottom portion of the concrete test specimen. When the load is applied in three-point bending, the layer will be under tension. Ultimately this investigation not only affirmed its hypothesis that structural CNTs can be applied to a concrete member for distributed sensing capabilities but also provided a new innovative approach that can be applied to SHM in the future. The use of these embedded nanoscale sensors allows for the detection of damage and deformations along the tensile face (2014). This approach allows for real-time feedback to changes in the structure such as strain and damage propagation/formation in order to evaluate structure's integrity.

In Thostenson's 2006 research along with Schumacher's 2014 study they briefly articulated the multi-functionality of CNTs. Although CNTs generally do not offer increased material strength, when incorporated with composites, CNTs can serve as a platform allowing for sensing within the structural reinforcing (Thostenson 2006). As articulated by Schumacher, the patch act as both reinforcement, provided by the glass fibers, in addition to a sensor as a result of the conductive network formed by the CNTs. (Schumacher 2014). This dual purpose technology has the ability to usher in a new innovative, integrated methodology of addressing SHM in addition to the rehabilitation of fatigued structures.

The theory that CNT composites act as multifunctional reinforcement was further investigated in 2007 when Zhang established that CNT composites can actually play a role in suppressing fatigue crack growth. In this investigation both single walled (provided by Cheap Tubes Inc.) and multi-walled (provided by Nanocyl) carbon nanotubes were dispersed in Epoxy-2000 and used to preform fatigue crack propagation testing using an MTS-858 material testing system following ASTM standard E647-05 (Zhang 2007). This experiment ultimately observed a reduction in crack propagation rate by an order of magnitude. In the case of the epoxy/MWCNT composites a "~1000% reduction in the crack growth rate in the low stress intensity factor amplitude regime" was observed (Zhang 2007). This reduction in crack growth was further enhanced with increasing weight fraction of the nanotube additives. The same could be said for the epoxy/SWCNT composites. The weight faction used for the MWCNT was ~0.5% while the SWCNT was in the range of 0.1% to 0.25%. The weight fraction of the nanotubes as well as the applied stress factor played a significant role in the reduction in crack growth rate (Zhang 2007). As a result of the addition of less than ~0.5 weight percentage of CNT additives, the polymer fatigue performance potential can be increased greatly. This study thus reaffirmed that carbon nanotube composites have the potential to be able to both suppress and detect the initiation of fatigue damage.

The use of CNTs has the potential for continued evaluation of the status of in-service SHM. The formation of these networks can enable real-time response to cracks changes in strain, temperature effects as well as the formation/propagation of damage a result of the electrical response of CNTs. In addition, its abilities when combined with reinforcing fibers, to not only act as a sensor but also the multifunctional enabling the suppression of fatigue damage, allows this integrated patch to be an excellent candidate as composite reinforcement.

2.4.3 Fabrication

One method to fabricate CNT-epoxy composites is to first disperse the CNTs into an epoxy resin. In many cases for uses in SHM, a calendering approach is applied. "The calendering approach utilizes a three-roll mill to untangle the agglomerates by feeding the dispersion through high-precision rollers that impart high shear forces" (Schumacher 2014). As shown in a similar procedure in **Figure 8**, nanotubes are first mixed by hand into the epoxy resin. Typically, a 0.5% weight concentration is added to the epoxy resin prior to processing through a three-roll mill (Thostenson 2006). As discussed previously by Zhang, the addition of less than ~0.5 wt.% of CNT additives has the potential to play a role in suppressing fatigue crack growth.

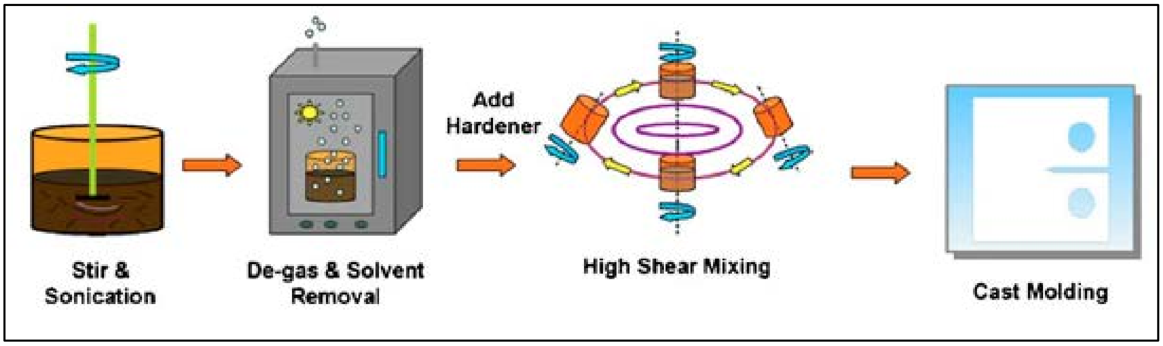

Figure 8. Procedure for composite fabrication (Source: Zhang 2007).

As employed in Gao's 2009 experiment, nanotube/epoxy dispersions were infused and composite laminates were produced with "cross-ply constructions of [0/90$_2$/0], [0/90$_3$/0] and [0/90$_4$/0] using a vacuum-assisted resin transfer molding technique (VARTM)" (Gao 2009). Essentially, the vacuum-assisted resin transfer molding was used to fabricate the fiber–epoxy composites with embedded CNTs (Thostenson 2006).

A fiber sizing agent containing dispersed CNTs can be used alternatively to that of the traditional calendering approach. This leads to the fabrication of a highly electrically conductive glass fiber/epoxy composites. Employing this method, "the distribution of CNTs in the composite can be controlled and substantial amount of CNTs agglomerates on the glass fiber surface which results in a 2 to 3 orders enhancement in the composite electrical conductivity in the axial, transverse and through-thickness directions" (Gao 2010).

CNTs can be also be fabricated as long films. Employing this method to make a sensor, network neural systems are developed in the form of a grid attached to the surface of a structure According to Rainieri, this method has potential applications in the field of structural monitoring of large civil structures (Rainieri 2007).

2.5 Field Instrumentation

2.5.1 Strain Gauge Placement

The placement of strain gauges can play a significant role in the determination of axial strain related to fatigue crack propagation. Strain gauges have been employed for decades in order to determine the applied stresses experienced by in-service bridges. Such as in the case of the monitoring system developed at the University of Delaware in 2000. The small battery operated system and foil strain gauges were able to capture peak stresses that ultimately assisted in load rating of the bridge, fatigue investigations, monitoring the bridge response as overloads crossed, and for general health monitoring of the structure (Shenton 2000). Stresses recorded from a strain gauge can then be plotted and related to AASHTO S-N fatigue curve or the actual design yield strengths of the material in order to draw conclusion about the current state of the structure. Strain gauge locations in reference to a fatigue crack can influence these values obtained. Therefore, gauges should be placed in a manner in which to capture the local strain experienced at the crack tip as well as along the projected crack path. Although there is no 'optimal' strain gauge location in which to capture all pertinent data, much consideration should be taken in order to employ gauges in an appropriate manner to accurately and appropriately monitor the structure, especially when considering fatigue and fatigue crack monitoring.

Ultimately, in order to record the highest strains being experienced by a fatiguing girder, the strain gauge should be placed near the tip of the crack. This technique allows for evaluation of local strain as the crack opens and closes. Moreover, gauges should not be placed too close the tip of the crack. Particularly when employing methodology of evaluating stress intensity factors using strain gauges, placing gauges too close to crack tip should be circumvented "to avoid plasticity and three-dimensional effects" (Sarangi 2010). But employing gauges too far from the crack tip will result in the inability to accurately capture strains are the crack mouth opening. Thus in Sarangi's 2010 research the optimal maximum radial distance (r_{max}) for gauge locations was examined. A finite element approach was implemented in order to determine the upper bound for radial location of the gauges. Ultimately this study found that r_{max} increases as the crack length increases. In addition the result of r_{max} as the ratio of crack length or half the crack length (denoted as a) to half the width (denoted as b) of the plate are shown below in **Table 1** for a tested edge cracked plate shown in **Figure 9**.

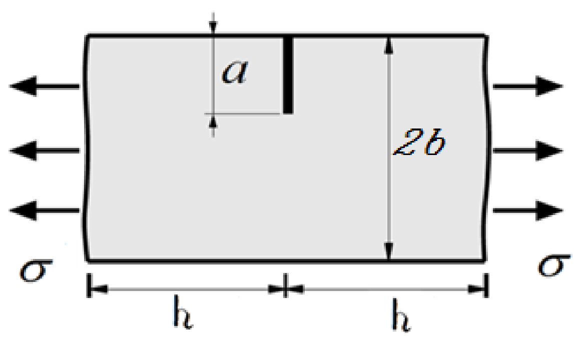

Figure 9. Edge-cracked plate (Source: Sarangi 2010).

Table 6. Variation of r_{max} for edge cracked plate with b = 1200 mm (47.24 in) (Source: Sarangi 2010).

a/b	a (in)	r_{max} (in)
0.00625	0.30	0.07
0.0125	0.59	0.16
0.025	1.18	0.30
0.05	2.36	0.53
0.1	4.72	1.01
0.15	7.09	1.62
0.2	9.45	2.02
0.25	11.81	2.66
0.3	14.17	3.61
0.35	16.54	5.39
0.4	18.90	8.23
0.45	21.26	19.90
0.5	23.62	13.68
0.55	25.98	7.05
0.6	28.35	4.75
0.65	30.71	3.29
0.7	33.07	1.88
0.75	35.43	1.36
0.8	37.80	0.70

As discussed by Sarangi, as the ratio of a/b increases, r_{max} increase initial but begins to decrease after reaching an a/b ratio of 0.45. The decrease in r_{max} values could be attributed to an influence by the bottom edge boundary condition (refer to **Figure 9**). This effect of the boundary condition is absent or insignificant at low values of a/b. This condition becomes more dominate at the ratio of a/b increase and crack length approaches the width b.

Nevertheless, this finite element approach to establish r_{max} can be quite useful in the determination of proper strain gauge placement. When instrumenting a structure one must consider the upper radial distance for gauge placement. In order to record accurate measurements, the radial location of strain gauge should be within this zone (Sarangi 2010).

In situations where a crack-stop hole has been drilled or a large section of the girder has been removed, such as in **Figure 10**, gauges are in many cases positioned at the free edge of the retrofit. But one thing to note is that when a strain gauge is placed near the edge of a hole (as shown in **Figure 10**), the strain gauge is also reading the local strain (Dexter 2013).

Figure 10. Weldable strain gauges applied near free edge of retrofit on Girard Point Bridge, Philadelphia, Pennsylvania (Source Dexter 2013).

Lastly, in addition to the consideration of maximum radial distance from the crack tip to the gauge, the location and amount of remaining gauges to be place should also be considered. Aside from placement at the crack tip, strain gauges should also be placed along the projected path of the crack. This is typical practice and allows for local deformation to be recorded ahead of the crack tip during cycling. The use of a strain gauge rosette can also be taken into account in order to estimate the principal strains at that location. The orientation of gauges is significant as the electrical resistance (stress) of the gauges is sensed in the direction parallel to them. The use of a strain gauge rosette arrangement will allow for the determination of principal stresses and ultimately the direction in which the crack is propagating, which can be quite useful for SHM of fatigue cracks.

3 Experimental Approach

The methodology employed for this research project was broken down into three main components: field monitoring, analysis and laboratory testing. Field monitoring allowed for initial *in situ* data from an in-service bridge structure found to have fatigue cracking issues. The numerical analysis was subsequently performed in order to better understand the structure. Using this knowledge, laboratory testing was executed with an intension of implementing a rehabilitation method that inevitably increases the fatigue life of these specimen.

3.1 Field Monitoring

In order to determine the stresses that the structures of interest experience on a daily basis the initial phase of this research project involved the instrumentation of DelDOT Bridge 1678-006. This structure as shown in **Figure 11** is located in Newport, Delaware and carries two travel lanes of Route 141 headed from Newport, DE towards New Castle, DE. It spans over the northbound lanes of Interstate 95.

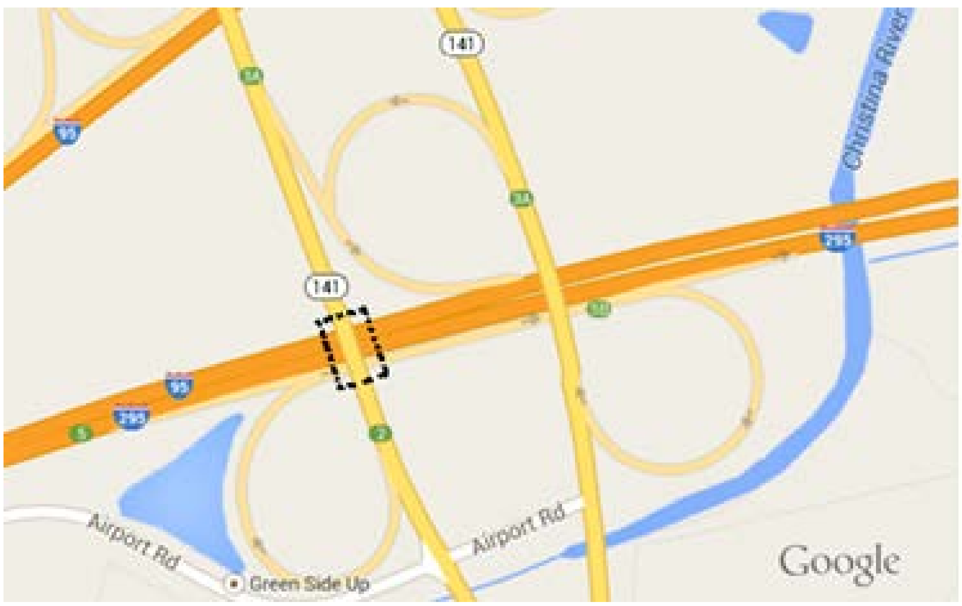

Figure 11. Aerial Location of DelDOT Bridge 1678-006 (Source: Google Maps).

The instrumentation of DelDOT Bridge 1678-006 involved the use of typical strain gauges in order to record the strains experienced by the structure over the course of several typical days. This bridge was chosen as a result of an investigation of structures in Delaware that have been found to have fatigue cracking issues. A time period of two weeks was selected as the duration of the monitoring and data collection of this bridge. The field study of this structure enabled measurement of in-service strains to represent a realistic scenario for laboratory testing.

3.1.1 DelDOT Bridge 1678-006

DelDOT 1678-006 was originally constructed in the early 1960's. As shown in **Figure 12**, this bridge consists of 5 spans with 4 piers located in and near the roadway of Interstate 95. Each span is comprised of six girders that carry the above roadway.

Figure 12. DelDOT Bridge 1678-006 on I-95 Northbound (Source: Google Earth).

Figure 13. North end abutment of DelDOT Bridge 1678-006.

Both the north and south ends of the girders, over the abutments, have developed fatigue cracks. The south end of the girder has a few minor cracks, while the north of the girder was discovered to have developed much more significant fatigue cracks (**Figure 13**). As shown in **Figure 14**, after a 2011 routine bridge inspection, a crack was found in Beam 3 of Span 5 of this bridge. Although other cracks were discovered, the most noteworthy of these, shown in Figure 14, initiated from the weld detail at the web-to-flange connection. After the 2011 inspection, a DelDOT crew drilled two 28.6 mm (1-1/8 in) diameter crack stop holes in an attempt to cease the crack propagation. In addition, a timber block was placed under the beam. A further inspection in 2012 revealed a vertical crack propagating through the previously drilled hole. Most recently, in February of 2013, a larger 51 mm (2 in) diameter crack-stop hole was drilled at the tip of the propagating crack, which has been effective up to the time when we visited the bridge.

Figure 14. Fatigue Crack on DelDOT Bridge 1678-006.

As a result of this fatigue cracking issue, this structure was determined to be a prime candidate for the proposed research. This bridge was instrumented and monitored in order to determine the in-service conditions. Due to its connection type, it has been determined to be fatigue Category E in accordance with the AASHTO LRFD Bridge Design Specification. In addition, Fatigue Category E was chosen based on commentary discussed in FHWA's Bridge Inspector's Reference Manual as shown in **Figure 15**. This information along with the measured data, allowed for a baseline for our research. In addition, this information jointly permitted the determination of the cumulative fatigue damage predictions and comparisons to that of the design life of the bridge. Thus allowing conclusions to be drawn about the current state of the structure and a determination of whether or not the field stresses exceed allowable limits.

Category E and E'

Includes details that have the lowest fatigue strength in comparison to those in other categories. Generally, for welded details in this group with the same configurations, Category E' applies if the flange plate thickness exceeds 20 mm (0.8 inch) or if the attachment plate thickness is 25 mm (1 inch) or more.

- Ends of partial length cover plates on girder or beam flanges.
- Welded attachment, with groove or fillet weld in the direction of the main members, more than 100 mm (4 inches) or 12 times the plate thickness.
- Welded attachment with curved transition radius.
- Welded attachment with loads transverse to welds.
- Intermittent fillet welds
- Shear stress on the throat of a fillet weld (Formerly classified Category F)
- Deck plate at the connection to floorbeam web.

Of all the details, those in Categories E and E' are the most susceptible to fatigue crack growth. These details should be closely examined at every inspection.

Figure 15. Commentary for Fatigue Category E and E' (Source: Bridge Inspector's Reference Manual – Section 8.1.33).

3.1.2 Strain Gauges

Typical CEA-06 series weldable strain gauges manufactured by Micro-Measurements (a division of the Vishay Precision Group) were employed on DelDOT 1678-006 in order to measure the strain experienced by the structure. An image of these typical gauges is shown in **Figure 16**. Strain gauges were welded to web and flange locations as discussed below. The gauges were simple strain gauges used in order to record strain. Images taken during the strain guage welding process of DelDOT Bridge 1678-006 are also presented below in **Figure 17** and **Figure 18**.

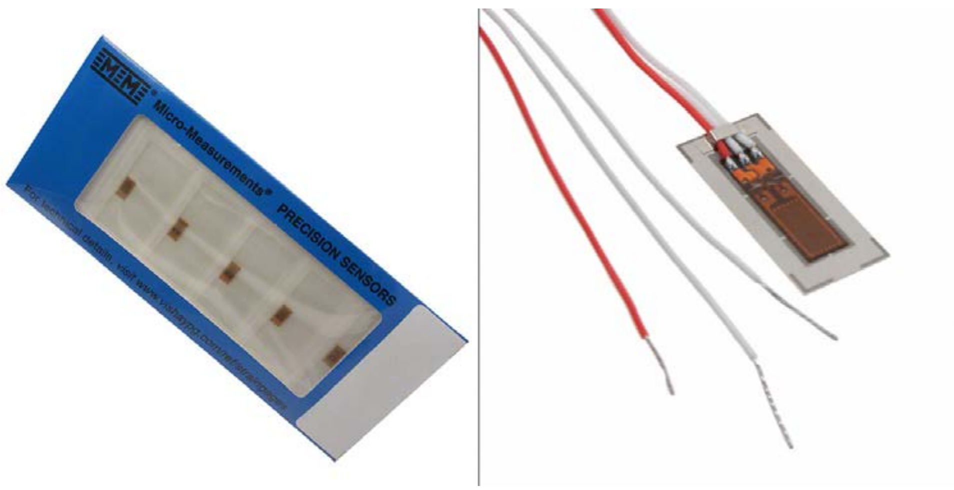

Figure 16. Sample weldable strain gauge (Source: www.digikey.com).

Figure 17. Photographs taken during strain gauge welding process on DelDOT Bridge 1678-006.

Figure 18. Photographs taken during strain gauge welding process of DelDOT Bridge 1678-006.

In total, 12 strain gauges were used between two different girders. Five gauges were employed on the East Face of beam 3 on span 5, two on the West Face of that same girder and one on both the East and West side of the bottom flange (two in total on the flange). Thus, a total of nine gauges were welded on this girder. All gauges welded to girder were wired back to the sensing network. Sketches of these gauge instrumentations are shown in **Figure 19**. As discussed in Section 3.1.1, this girder has previously been drilled with several crack-stop holes after previous bridge inspections.

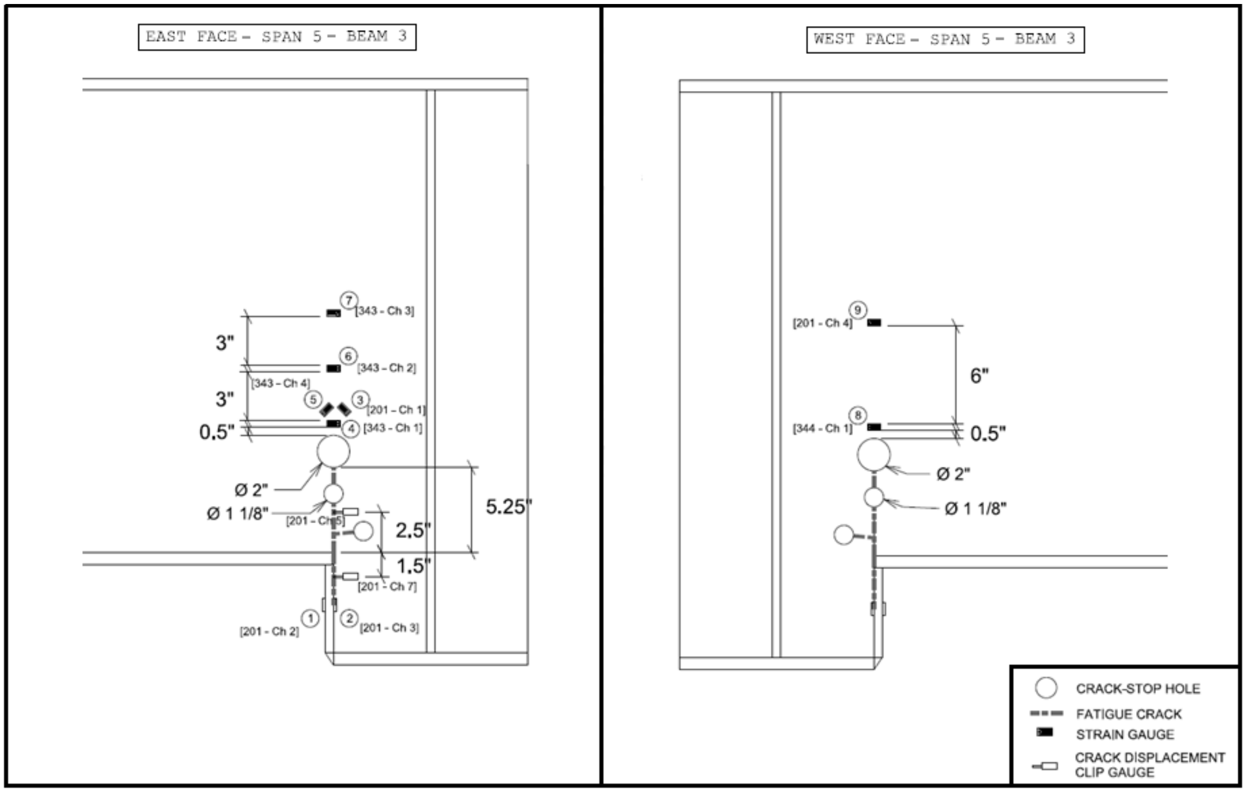

Figure 19. Strain gauge instrumentation plan - Beam 3 of Span 5.

In addition to Beam 3, Beam 4 was also instrumented with strain gauges. This was done in order to compare result of the beam with fatigue damage to that of a “healthy girder.” There were a total of three strain gauges welded to this girder as shown in **Figure 20**.

It should also be noted that gauges 4, 8 and 11 as well as 7, 9 and 12 are in the same vertical position. But these gauges are located on opposite sides of the girder or (8 and 9) or opposite girders (11 and 12). Please refer to **Figure 19** and **Figure 20** for details regarding location of the gauges.

The theory behind placing the strain gauges in the locations shown in **Figure 19** and **Figure 20** was to determine the stresses in the projected path of the fatigue crack. The largest stresses should occur at the tip of the crack and decrease with distance from the crack mouth opening. In addition, gauges 3, 4 and 5 were oriented similar to that of a strain rosette in order to determine the principal direction of the crack.

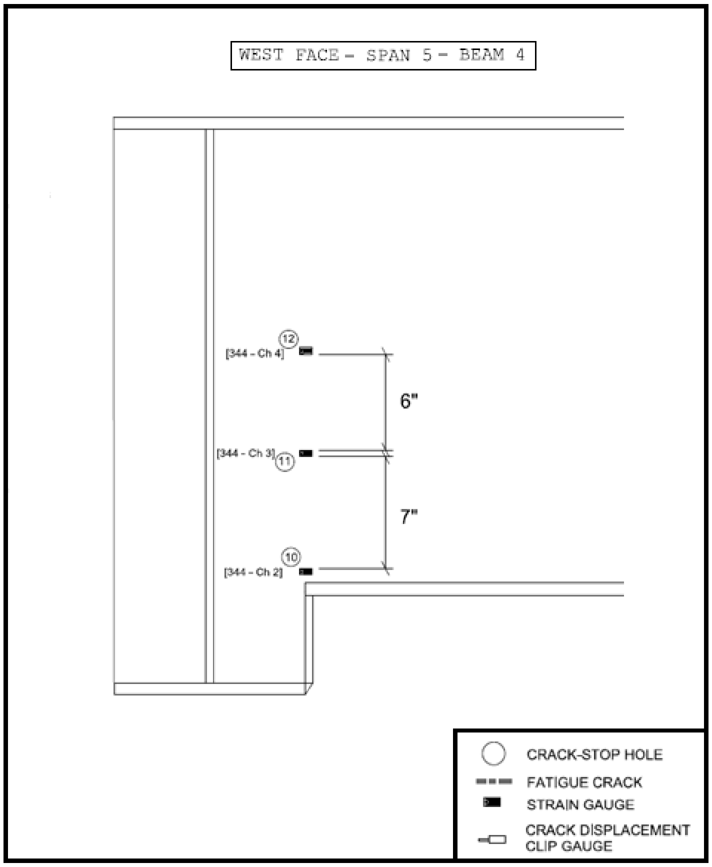

Figure 20. Strain gauge instrumentation plan - West face of Beam 4 on Span 5.

3.1.3 Potentiometer

In addition to the strain gauges, potentiometers were also placed on the girder. These gauges allowed for measurements of the crack motion displacements occurring as vehicles traveled over the girder. These displacements can be correlated to the distance the crack mouth is opening and closing. Two potentiometer gauges, presented in **Figure 19**, were placed on beam 3 of span 5.

3.1.4 Wireless Sensing Network

The wireless sensing network (WSN) employed for this research was developed by LORD Corporation MicroStrain® Sensing Systems. This product known as V-Link® -LXRS®, shown in **Figure 21**, allows for the ability to record simultaneous measurements taken from the strain gauges and wirelessly sync them to a computer to store the data through use of Node Commander ® software.

Figure 21. V-Link® -LXRS® (Source: www.microstrain.com).

As previously discussed, each strain gauge is wired to the WSN. This network is comprised of individual nodes that wirelessly send recorded strains to a data logging element. Each node has four available channels that can be used for gauge inputs. As there are 12 strain gauges employed on the bridge, three nodes were utilized for the project. The identification numbers for the three nodes used in this study are Node 30343, Node 30344 and Node 33201. **Figure 22** depicts two of the three nodes in which gauges were wired.

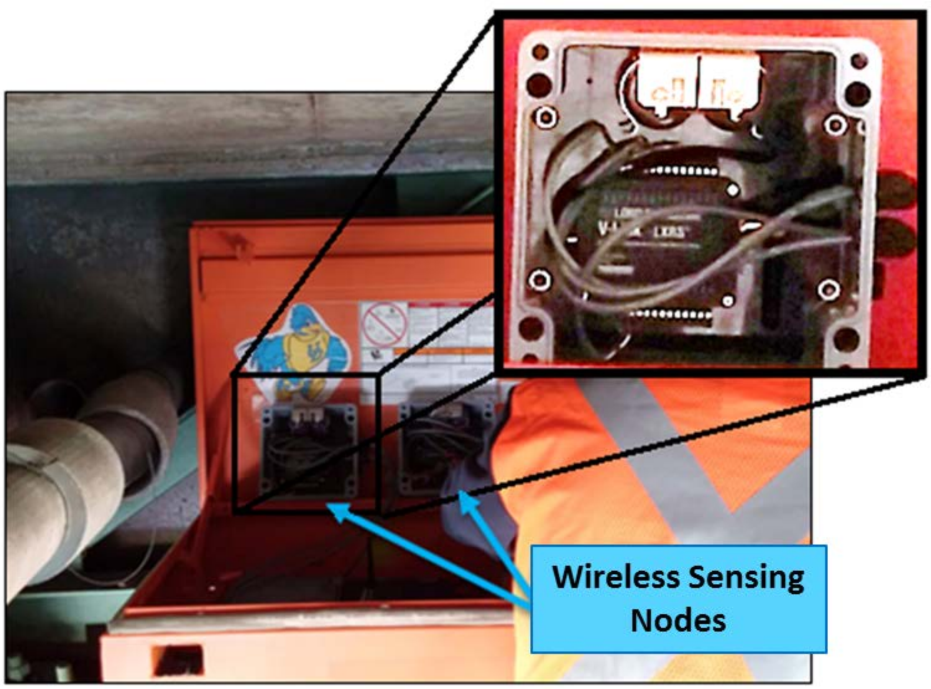

Figure 22. Wireless sensing nodes.

3.1.5 Data Logging

Node Commander® 2.10.0 Software (**Figure 23**) was employed in order to record and store all strain measurements taken during the two-week monitoring period. Software can be set to continuously monitor data or to do burst sampling of a specified time interval. A continuous sampling rate of 32 hertz was implemented for this study. From the software, nodes can be configured and real-time synchronized sampling can be performed from any distance within the range of the individual sensor.

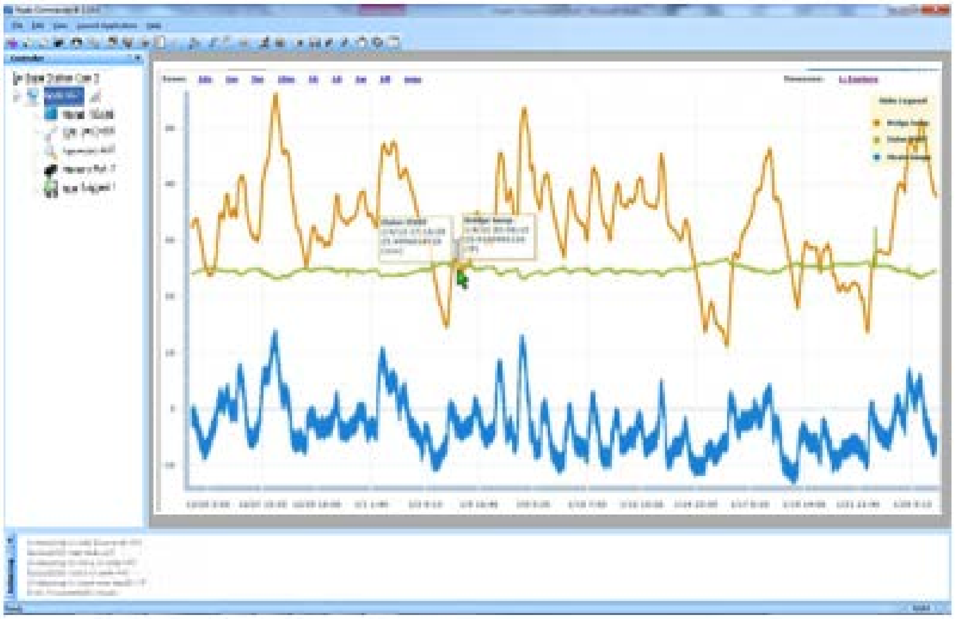

Figure 23. Node commander sampling.

Figure 24, **Figure 25**, and **Figure 26** are a few photographs taken during the instrumentation process. The girder was initially ground to ensure contact with strain gauges. Gauges were then spot welded in their desired positions and wires were run to monitoring system. The final step was to apply a protective coating over strain gauges. This coating acted as a safeguard to protect the gauges from moisture and debris in addition to sealing gauge contacts.

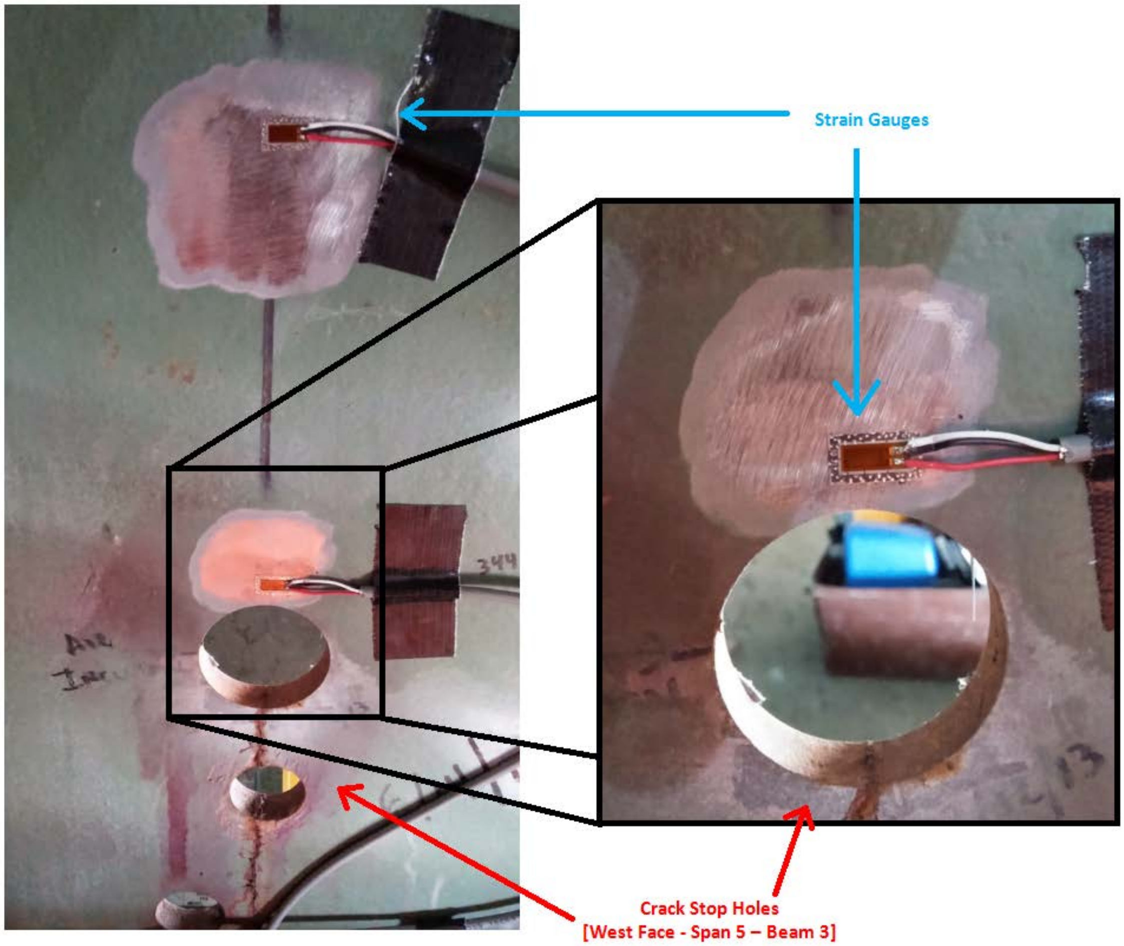

Figure 24. Photographs taken during installation of strain gauges - West face of Beam 3 on Span 5.

Figure 25. Before installation of monitoring network.

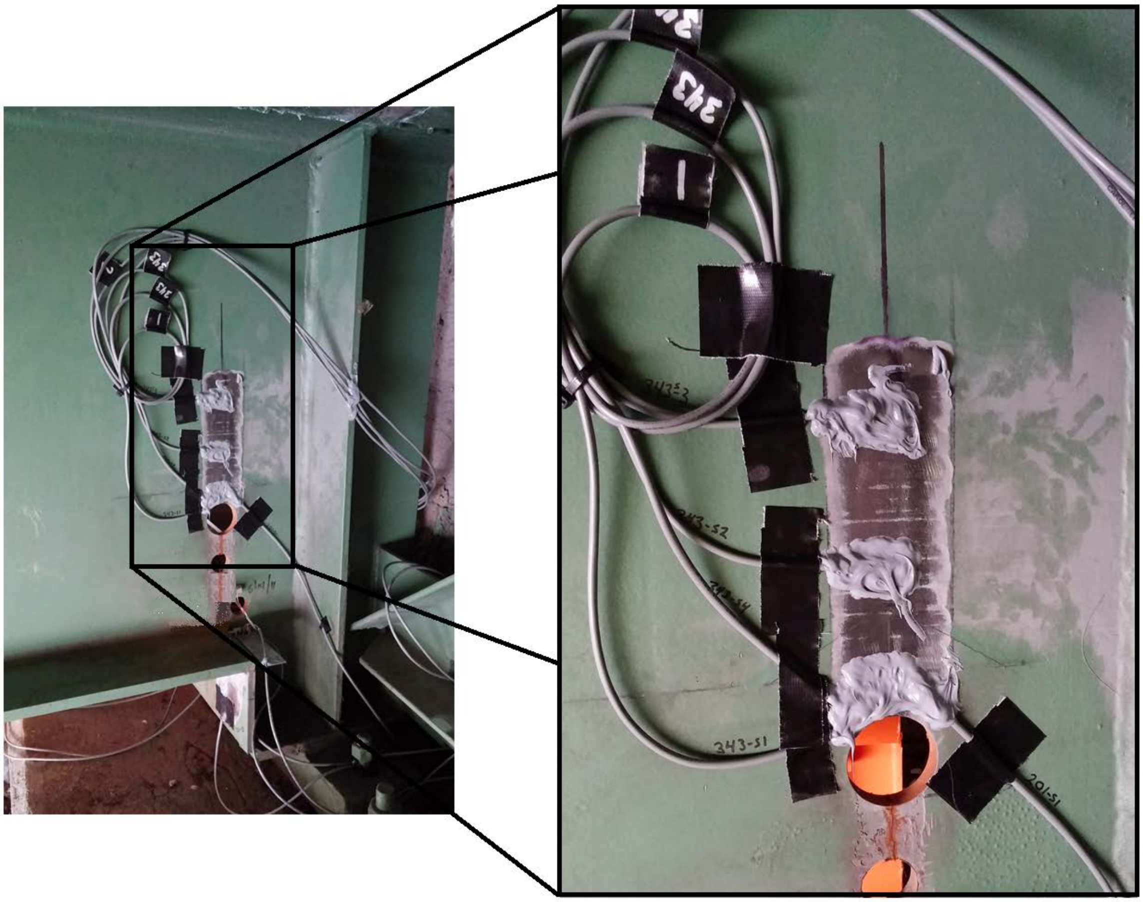

Figure 26. After installation of monitoring network.

Overall, the strain monitoring was a four-part process. As depicted in **Figure 27** initial phase involves the input sensors (strain gauges and potentiometers). These sensors are connected to nodes which wirelessly send recorded readings to data storage device by way of the wireless sensor data aggregator. Finally, data is stored on a computer or other device for operator's convenience.

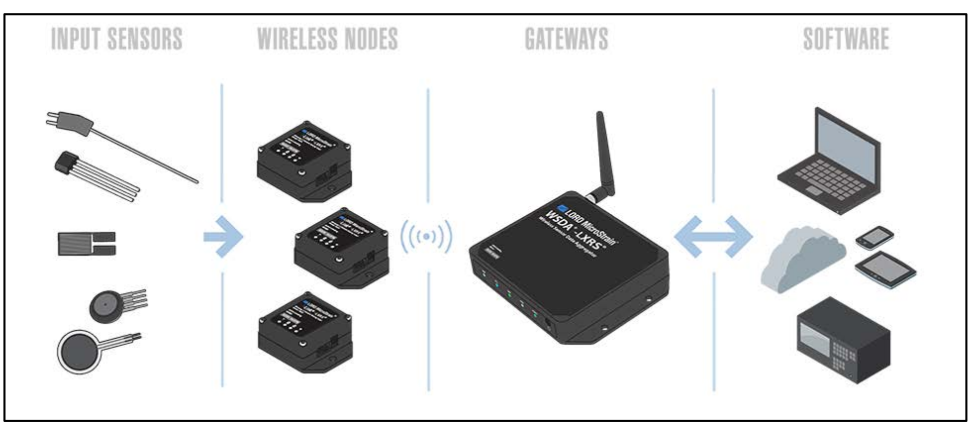

Figure 27. Overall monitoring network process (Source: www.microstrain.com).

3.2 Numerical Data Analysis

In order to better understand data taken in the field and transform it into more functional information that can be used in the second phase of research involving laboratory testing, numerical analysis was performed. The process included individual load cycle counting, generation of histogram plots, statistical analysis, calculations of Miner's Number and fatigue life calculations. Software such as MATLAB, DPlot, and Microsoft Excel were instrumental in the undertaking of these procedures.

It should be noted that the recorded strain data were initially converted to stresses employing the basic mechanics of materials formula assuming a linear-elastic response and (which is valid for the range of recorded strains) and Young's Modulus. This conversion allows for a better overall understanding of the data.

3.2.1 Cycle Counting

The number of cycles a bridge experiences inevitably determine the fatigue life of that structure. Stress range is also a deterministic parameter of fatigue damage. Stress range loading analysis was performed to compare observed stress ranges and cycle counts to AASHTO LRFD fatigue resistance specifications. Using Table 6.6.1.2.3-1 of the AASHTO LRFD Bridge Design Specification, fatigue detail category of E was determined to be associated with the connection experimentally tested. Employing this knowledge with Table 2 of the FHWA Steel Design Handbook Design for Fatigue provided the detail category constant, *A*. This table taken from handbook is shown in **Table 7**. The curve displayed in **Figure 28** represents the fatigue resistance threshold for a given stress range. The AASHTO LRFD fatigue resistance threshold specification provides an additional benchmark to which to compare our experimentally collected data to determine if extrapolated cumulative fatigue damage predictions for the design life of the bridge exceed allowable levels.

Table 7. Detail category constant, *A* (Source: FHWA Steel Deign Handbook: Design for Fatigue).

Detail Category	Constant A
A	250×10^8
B	120×10^8
B′	61×10^8
C	44×10^8
C′	44×10^8
D	22×10^8
E	11×10^8
E′	3.9×10^8

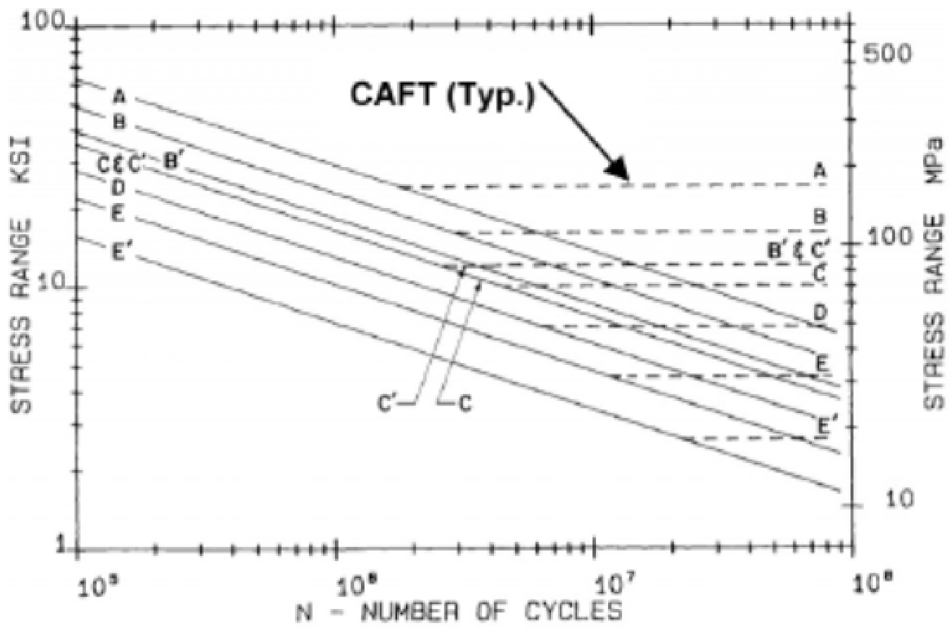

Figure 28. AASHTO fatigue life curve (Source: FHWA Steel Deign Handbook: Design for Fatigue - Figure 21).

The horizontal region of the graph depicted in **Figure 28** represents that of the infinite fatigue life. Within this section, theoretically a structure can withstand a boundless number of loading cycles without development of fatigue damage. For the examined fatigue category E structure in this study, the associated stress range is 31 MPa (4.5 ksi). The sloped region demonstrates an inverse relationship between stress range and allowable number of cycles, indicating a finite design state. LRFD equation 6.6.1.2.5-2 defines the finite-life equation as follows, where ΔF is the stress range for a given number of cycles, N is the number of cycles, and A is the constant defined above:

$$(\Delta F)_n = \left(\frac{A}{N}\right)^{\frac{1}{3}}$$ **Equation 2**

Thus, cycle counting is an integral part in the determination of the fatigue life of the structure. As specified in The American Society of Testing Materials (ASTM), two main counting methods can be employed for the fatigue analysis. These include simple range counting and rainflow counting. Although both are viable cycle counting methods, ultimately rainflow counting has been found to be more accurate in the identifying stress ranges observed by a fatigue detail. Both methods however have been employed for analysis of DelDOT Bridge 1678-006.

3.2.1.1 Simple Range Counting

Simple range counting and its related methodologies essentially compare successive stress reversals to determine the applied stress range. A range represented by the difference between consecutive local maxima and minima is counted as a half cycle, with its corresponding negative range accounting for the second half of the full cycle. An example taken from ASTM E1049-85 is shown in **Figure 29**. Deviations from the simple range counting method may only count positive (valley to peak) or negative (peak to valley) ranges.

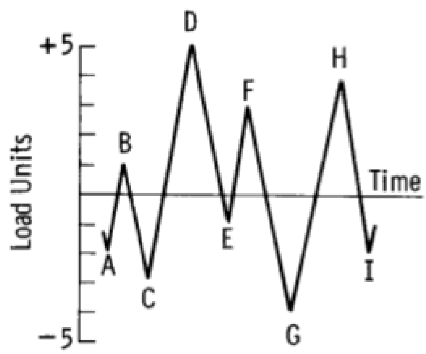

Range (units)	Cycle Counts	Events
10	0	
9	0	
8	1.0	C-D, G-H
7	0.5	F-G
6	1.0	D-E, H-I
5	0	
4	1.0	B-C, E-F
3	0.5	A-B
2	0	
1	0	

Figure 29. Cycle counting using simple ranging counting (Source: ASTM E1049-85).

3.2.1.2 Rainflow Counting

Rainflow counting is quite more complex than that of simple range counting. This algorithm integrates a more refined approach that has been shown to more accurately predict the fatigue life in studies where different methods have been compared. Rainflow counting addresses shortcomings of simple range counting which may underestimate the actual fatigue damage imparted on a structure. One of the main detriments of the simple range counting method is that stress states that do not lie adjacent cannot be compared. Therefore, small oscillatory noise, or vibrations collected by instrumentation between primary stress reversals can hinder the algorithm from recording full amplitude stress cycles. However, rainflow algorithms are able to compare non adjacent stress reversals by relying on strain hysteresis loops. Small oscillations between major stress reversals are counted through linear-elastic loading and subsequent unloading within a closed, larger hysteresis loop. An example of Rainflow counting is shown in **Figure 30**. The actual notion involving hysteresis loops is illustrated in **Figure 31**.

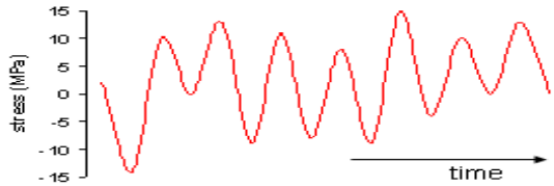

Bin (Sr)	Count
1.0	0
2.0	1 + 1
3.0	0
4.0	1
5.0	0
6.0	0
7.0	0
8.0	0
9.0	1

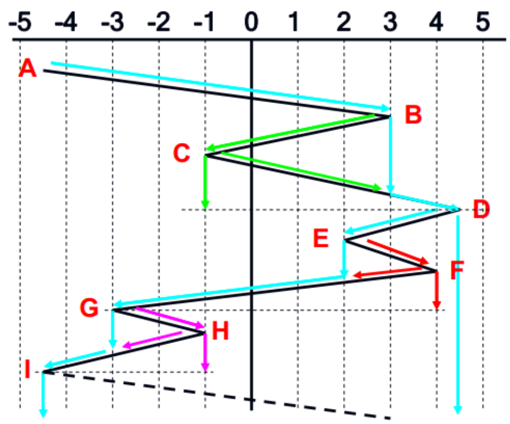

Figure 30. Cycle counting employing Rainflow counting method.

The image above depicts the stress-time history plotted so that the time axis is vertically downward. The lines connecting the stress peaks and valleys are imagined to be a series of pagoda roofs. Several rules are imposed on rain dripping down these roofs so that cycles and half-cycles can be counted as explained in previous section.

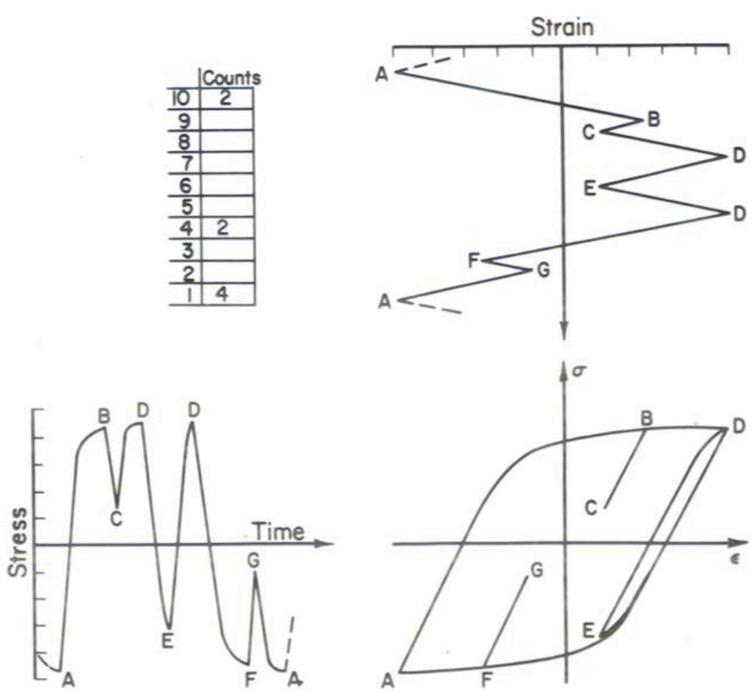

Figure 31. Theory of Rainflow counting (Downing & Socie, 1982).

Rainflow counting algorithms were first introduced in 1968 by Tatsuo Endo and M. Matsuishi in 1968. This theory has since been further research and developed during the subsequent years. It should be duly noted that S.D Downing and D.F. Socie's study published in a 1982 article by the International Journal of Fatigue has henceforth been a major contributor to what we know today as rainflow counting algorithm. These counting algorithms along with Matsuishi & Endo and amongst other cycle counting algorithms have been incorporated into ASTM E 1049-85.

3.2.2 Miner's Number

The cycle counts allow for the application of Miner's Rule. In order to find a cumulative damage model for a spectrum of load range magnitudes, the Palmgren-Miner Rule was applied to the observed experimental stress ranges. The Palmgren-Miner Rule is an empirical approach for calculating the damage caused by stresses of variable amplitudes such as in the data recorded in this study. Miner's rule is expressed as:

$$\sum_{i=1}^{k} \frac{n_i}{N_i} = C \qquad \textbf{Equation 3}$$

This expression is essentially a comparison of the experimental cycles to the allowable cycles. The theory of miner's rule is based on each observed stress range proportionally incurring damage on the total fatigue life of the member. It essentially defines failure, where n_i/N_i is the fractional damage received from the i^{th} stress range. Theoretically, failure ultimately occurs when the additive proportion of the spectrum of stress ranges, $C = 1$. The experimental cycles refer to the previously calculated cycles using both ASTM methods including Rainflow analysis.

3.2.3 Fatigue Life

Upon calculation of Miner's number for each of the 12 individual sensors used in order to monitor DelDOT 1678-006, the corresponding fatigue life can be estimated. To execute this calculation with quantities for which the physical significance was more readily apparent, the cycles counted during the monitoring period were linearly extrapolated to compute the number of cycles that would occur over 25 years (assuming no change in traffic; simply for mathematical purposes). The fatigue life is then the ratio between 25 and Miner's number. This approach to calculate fatigue life is based on the theory of Miner's rule proposed by A. Palmgren in 1924 and further developed by M. A. Miner in 1945. The overall steps involved for fatigue life calculations are illustrated in **Figure 32**. This same process has been outlined for the purposes of this research.

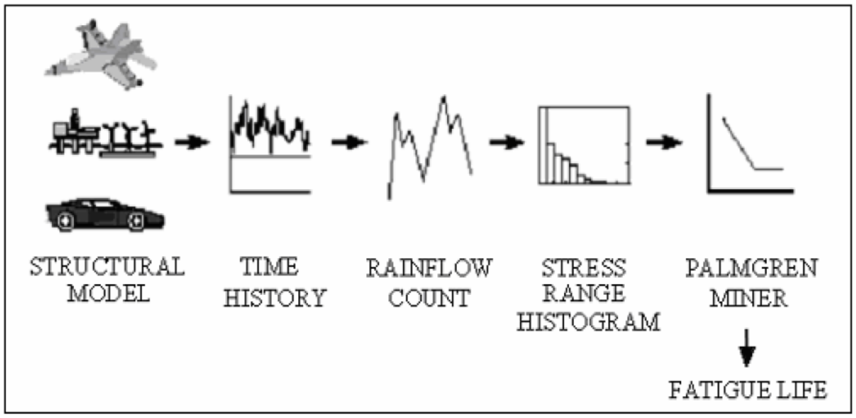

Figure 32. Steps in a fatigue life calculation (Ariduru, 2004).

3.3 Laboratory Testing

Laboratory fatigue testing was performed adopting approach set forth in the *American Society for Testing and Materials* (*ASTM*) Standard E647. A standard single edge-notch, steel, compact tension (CT) specimen, as discussed in Section A1.1 of this standard, was employed as steel specimen for all laboratory testing **Figure 33**. A sketch of the geometry of the standard (CT) specimen used for the experimental work in this work is shown in **Figure 34**.

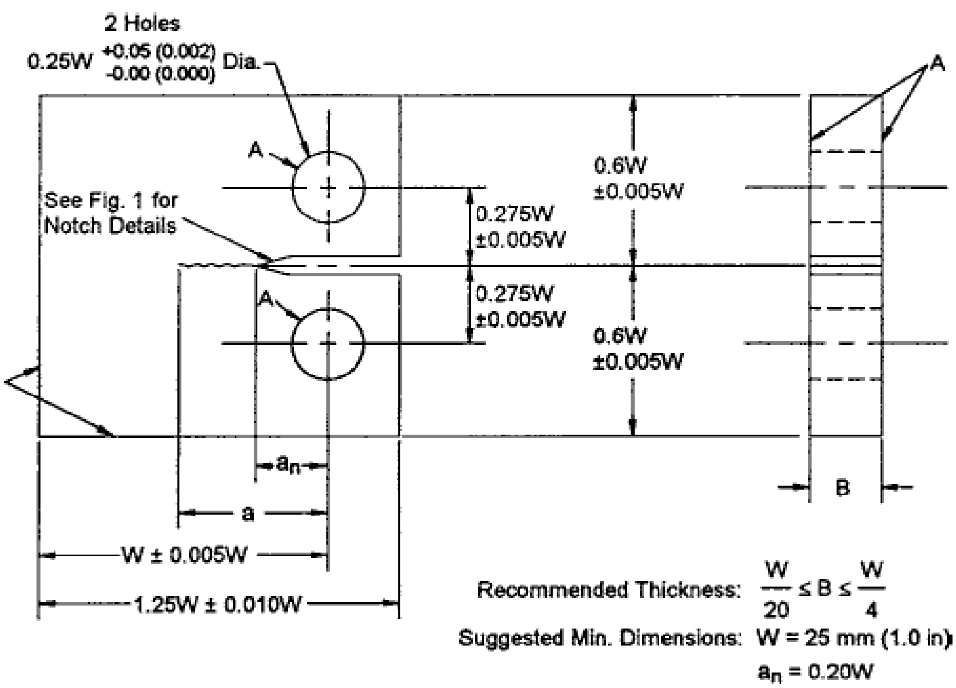

Figure 33. Standard CT Specimen for fatigue crack growth rate testing (Source: ASTM E647-08).

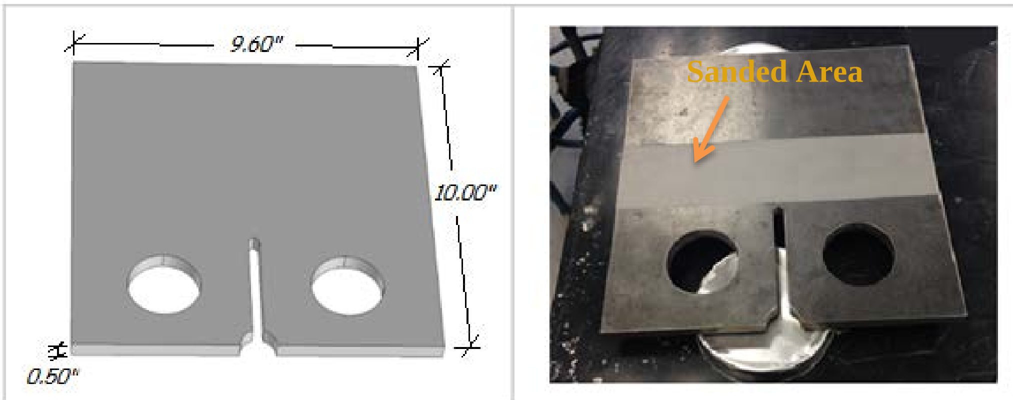

Figure 34. ASTM CT Specimen with 12.7 mm (0.5 in) thickness.

Prior to loading specimen in tension for fatigue testing, a 10.5 mm (0.41 in) crack was initiated by loading samples to about 72,000 cycles. Preceding this, all specimens were pre-cracked 1 mm (0.04 in) as dictated in ASTM E647-08. The importance of this is to provide a sharpened fatigue crack of adequate size and straightness for each specimen. The overall purpose of the laboratory testing is to demonstrate the extension of fatigue life using a composite material as a structural patch. This research aimed at the development of a patch that was composed of a sensing layer in addition to the actual structural layer. Thus allowing for *in situ* monitoring of a fatigue crack in a structure that has been rehabilitated.

Much of the manufacturing of the composite structural patch was performed at the Center for Composite Materials (CCM) at the University of Delaware. This extensive process included: sandblasting, application of acetone, coating a fabric layer with carbon canotubes (CNTs), adhesive placement, vacuum bagging, and curing of the specimen. Please refer to Appendix E for images taken during structural patch manufacturing process.

Due to its mechanical properties and overall provided stiffness, the structural composite employed for this study was M40J unidirectional ply laminate fiber with G94 resin system manufactured by Toray Composites (America), Inc. Based on the technical data sheet provided by the manufacturer this material's fiber property includes a tensile strength of 4413 MPa (640 ksi) and a tensile modulus of 377 GPa (54.7 Msi). Taking into account the 35% ±2% fiber/resin volume fraction, the tensile modulus of the composite patch is about 231 GPa (33.5 Msi) – 241 GPa (35 Msi). Ideally, in order to precisely transfer the applied load from the steel specimen or member to the composite patch, in order to decrease the strain, patch must possess tensile modulus equal to or greater than that of the steel itself. Considering steel has a modulus of 200 GPa (29 Msi), M40J was chosen for this research.

Material was also selected as a result of preliminary tests using dog-bone steel specimen and previous promising research that has demonstrated, when adhered to steel, material such as this has capability of decreasing the overall strain experienced in the steel by transferring the applied load. This reduction in strain concentration inevitably will lead to improved fatigue life for the steel and bridges when implemented.

Previous experiments have been conducted here at the University of Delaware solely utilizing the proposed sensing layer. As previously discussed, the sensing layer will allow for *in situ* measurements in order to monitor structures when incorporated with structure patch. The overall objective of these experiments was to establish a point of reference for the subsequent holistic rehabilitation tests, which integrated both the sensing and the structured patch. Not to mention the simple validation of the accuracy of the proposed sensing layer; which these experiments in return did verify.

The laboratory research focuses on three individual phases. The initial phase involved a baseline test of the steel specimen previously discussed. This specimen was unaltered and unchanged from its original fabrication. Upon completion of this preliminary test, a new specimen was drilled with a crack-stop hole, a fatigue crack rehabilitation method commonly used by bridge owners. Specimen #2 was then cyclically loaded to in order to simulate fatigue loading. The final experiment focused on the rehabilitation of a steel specimen employing the composite patch and sensing layer. This test aimed at demonstrating of the effectiveness of our innovative rehabilitation method employing composite materials with sensing capabilities.

As a result of the information revealed from the field instrumentation process and some simple amplitude loading tests, a load with amplitude fluctuating between 89 kN (20 kip) and 125 kN (28 kip) was chosen for fatigue testing. Load was applied at 2.5 Hz. Although it unlikely that these experiments will exactly replicate the recorded strains experienced in the field monitoring phase of the project, load induced in laboratory testing will allow for accurate strain values that encourage fatigue damage. Field monitoring displayed that load induced on bridge is quite variable. Not only is the applied load fluctuating but also the strain measurements will continue to change as the crack continues to propagate. Strains recorded during a selected week will differ from measurements taken when the crack is longer. Therefore, rather than attempting to recreate these unpredictable values, the aforementioned constant amplitude loading range was employed for all fatigue experiments.

Loading was performed utilizing a force transducer manufactured by MTS (Model 661.22c-01 with a maximum force capacity of 245 kN (55 kip)). With the given loading scenario, each fatigue test took at least 20 hours to fail the specimen. For each test, the loading was halted after every about 20,000-25,000 cycles in order to measure the crack length. Although the placement of back-face strain gauges also allows for calculation of crack length during testing, simple crack length measurements ensure consistency.

Ultimately, knowledge gained from these experiments will determine the effectiveness of our rehabilitation method and its possible application as viable solution to fatigue cracking issues in a real world scenario.

3.3.1 Baseline Testing (Specimen #1)

An initial E647 fatigue test was conducted in order to establish a baseline relationship between crack lengths and resistance changes. For this preliminary test, no structural patch was incorporated. A pre-cracked ASTM standard single edge-notch CT specimen was tested. Strain gauges were mounted to specimen prior to loading, as shown in **Figure 35**, in order to monitor basic strain data experienced by the specimen as it undergoes fatigue loading.

The philosophy behind the positioning and layout of strain gauges was quite simple. Referencing **Figure 35**, gauges 1, 2, 3 and 4 were to remain consistent among all lab specimens. Gauge 1 is located at the neutral axis of the specimen. Theoretically by the properties of basic mechanics, the portions one side of the neutral axis should be in a state of tension, while those on the opposite side will be in compression. Therefore, gauges were placed both above and below this location in order to determine the strain response of specimen relative to the neutral axis. In addition, gauge 1 was situated in response to the subsequent tests employing the drilled hole in order to capture the strain near the edge of the crack-stop hole that will be drilled in Specimen #2. Gauges 2 and 3 were placed above the neutral axis in order to later illustrate a strain profile. This profile should theoretically be linear. Finally, Gauge 4 is located on the back face of the specimen in order to determine the actual incremental crack length as discussed in Newman's 2011 report. The approach involves using the back face strain and calculating the ratio of crack length to specimen width using empirically-based equations (Newton 2011). Although these equations can be quite extensive, they do accurately permit determination of the crack length from simple measured strain.

In order to accurately compare and contrast data measured from different experimental phases, gauges locations need to match up. Therefore, strain gauges 1, 2, 3 and 4 shown in Figure 35 are all consistent with gauges 1, 2, 3 and 4 on all lab specimens.

The anomaly for this specimen was Gauge 5, which for baseline testing was located 0.50 inches from the crack mouth. This gauge assisted in pre-cracking strain measurements as well as measuring strains occurring at the crack mouth.

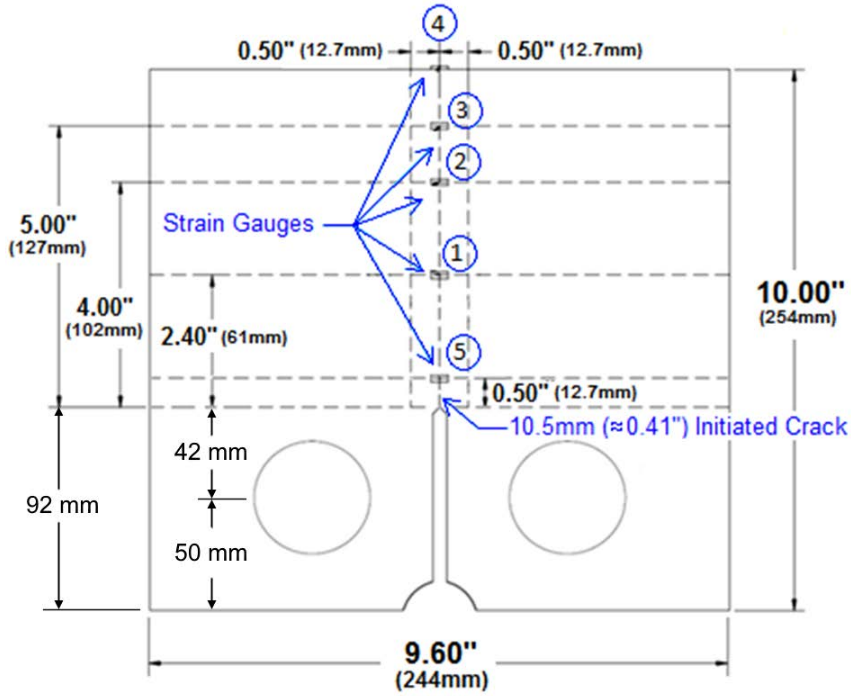

Figure 35. E647 fatigue test Specimen #1 (baseline) instrumented with strain gauges.

The specimen was fatigue loaded to failure employing the previously described loading conditions at 2.5 Hz. This experiment allowed for a general understanding of the overall fatigue limits of the steel specimen. This threshold is used to draw comparisons to subsequent test results.

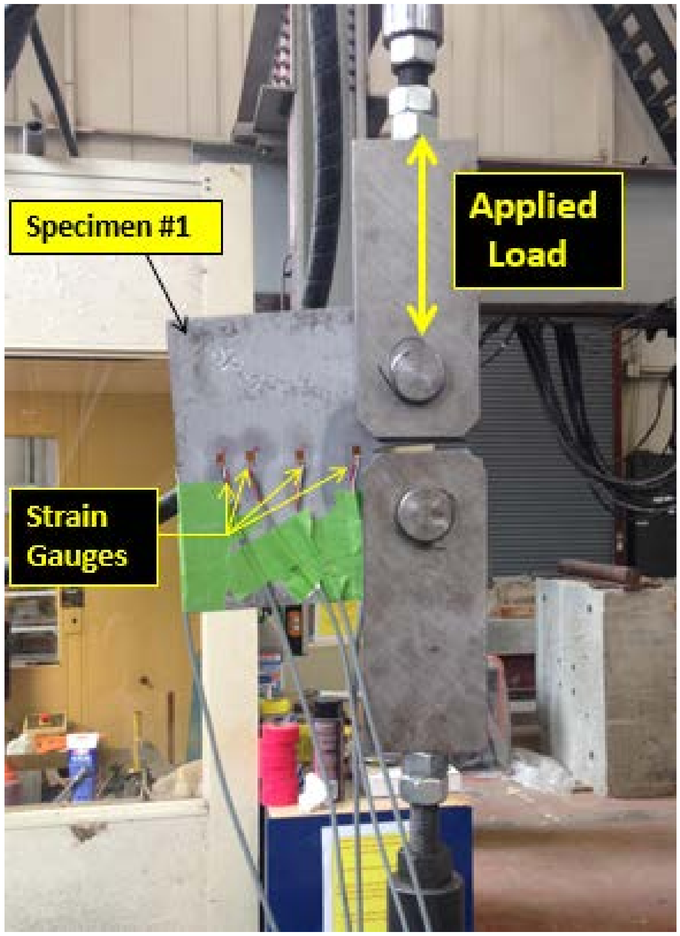

Figure 36. Baseline testing experiment #1 setup.

3.3.2 Rehabilitated Plate: Crack-Stop Hole (Specimen #2)

In order to simulate the scenario experienced in the field on DelDOT 1678-006, a crack-stop hole was drilled into a CT specimen prior to fatigue testing. This experiment had dual purposes. The initial goal of this testing was to ensure that a drilled crack-stop hole will reduce the overall stress concentration. In addition, this investigation aimed at demonstrating that the suggested minimum diameter of the hole drilled (25.4 mm (1.0 in)) is sufficient enough to stop the propagation of a fatigue crack. Preliminary calculations have been computed employing formula developed by Rolfe and Barsom in 1977. This simple formula discussed in Chapter 2 and utilized in Appendix D, theoretically, determines the diameter of the crack-stop hole required to arrest crack growth by means of the nominal stress range, crack length and yield stress. Although this formula is quite simplified, it does provide initial insight into an estimated hole diameter that should be employed in order to arrest propagation of fatigue crack.

As briefly articulated in Chapter 2, the rehabilitation method of drilling a crack-stop hole has been shown to extent the fatigue life of damaged sections. However, this fatigue improvement is based on the proper drilling of the hole. **Figure 37**, found in the *Manual for Repair and Retrofit of Fatigue*

Cracks in Steel Bridges, illustrates how the drill bit should be positioned relative to the crack tip in order to capture the plastic zone region (Dexter 2013). If crack tip is not fully captured, the crack will continue to propagate. There are two viable methods in which to drill the hole. The first technique involves the centering of the drill bit over the crack tip. The second practice requires user to drill in such a manner that the outer diameter of the drill bit intersects with the crack tip. This method of drilling ahead of the anticipated crack ideally will ensure the entire crack is fully encompassed (Dexter 2013). This methodology outlined in **Figure 37** was employed for specimen tested in this study. The hole was drilled in Specimen #2 about 1.5 mm (0.0015 in) from where crack tip was estimated to be. Rationale for this was to ensure entire crack tip was encompassed in drilled hole. A drill press with a twist bit was employed in order to drill the hole. As discussed by FHWA there are two viable bits that may be utilized: an annular cutter (or auger hole saw) and twist bits. However, twist bits should only be used for holes up to 25.4 mm (1.0 in) in diameter (Dexter 2013). Considering the size of the hole to be drilled was one inch, a twist bit was employed.

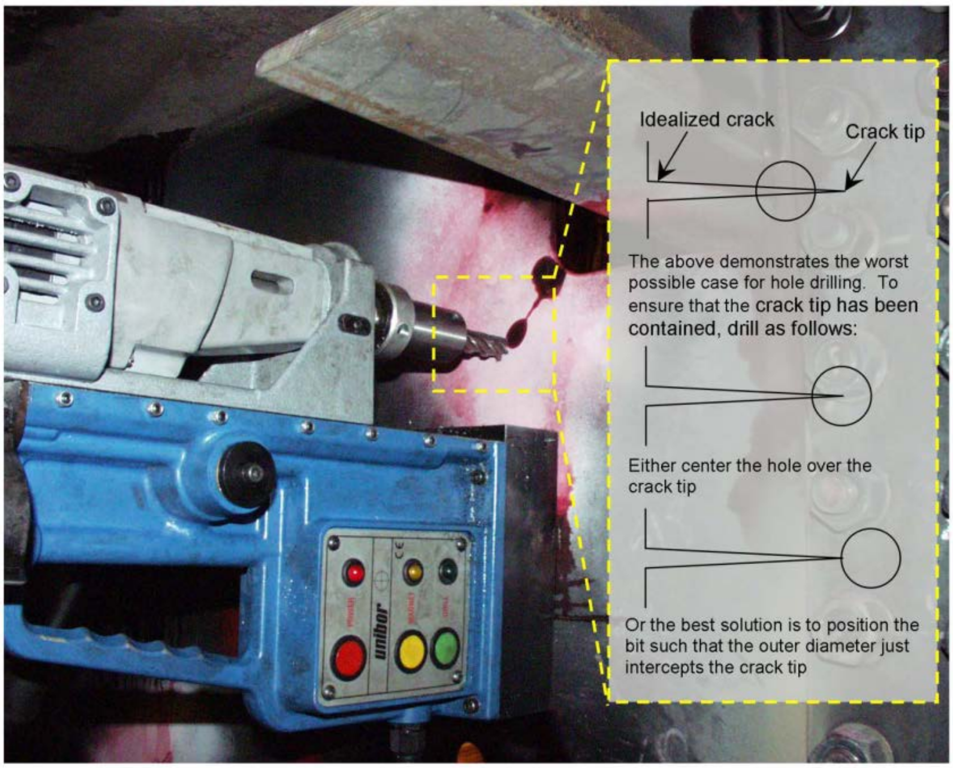

Figure 37. Crack tip identification with red dye penetrant and proper drill bit placement (Dexter, 2013).

Initially it was suggested to replicate the diameter of the crack-stop hole, along with the gauge instrumentation plan employed in the field in order to best connect the field and lab testing for this project. This, however, was found to be an issue is several aspects of the research as lab investigations involved small scale testing. A 25.4 mm (1.0 in) diameter hole was selected for the lab specimen as it is the smallest hole that the FHWA recommends (Dexter 2013). The bridge monitored in the initial phase of the project utilized a 50.8 mm (2.0 in) diameter hole. Relative to the depth of the girder two inches is a reasonable size hold diameter for the field. In addition, a simple calculation, shown in Appendix D, suggests that a 28.6 mm (1.125 in) diameter hole should theoretically be sufficient enough to cease crack propagation based on the current loading and crack length in the bridge member. However, for the sake of small scale laboratory testing, the initial crack length is only 10.5 mm (0.41 in) and the plate length is 254 mm (10 in). This is in comparison to in the field which possesses a 216 mm (8.5 in) crack length and 727 mm (28.625 in) web depth. Simple calculations utilized this same equation demonstrated in Appendix D using the parameters of lab specimen would clearly validate a 25.4 mm (1.0 in) hole is sufficient, especially when considering nominal stress range is only 55.2 MPa (8 ksi) and crack the full crack length is less than 50.8 mm (2.0 in). Therefore, it is more appropriate to employ a 25.4 mm (1.0 in) diameter hole as opposed to the scenario depicted in the field.

In addition to the drilled hole, strain gauges were also mounted to the specimen as shown in the subsequent **Figure 38**. Gauge placement, as previously discussed in Section 3.3.1, was based on maintaining consistency amongst all specimens. Therefore, strain gauges in **Figure 38** are all located consistent with gauges 1, 2, 3, 4 on all specimens.

Upon completion of hole drilling and mounting of strain gauges, Specimen #2 was cyclically loaded to failure under the same conditions as previous specimen. The experimental setup is depicted in **Figure 39**.

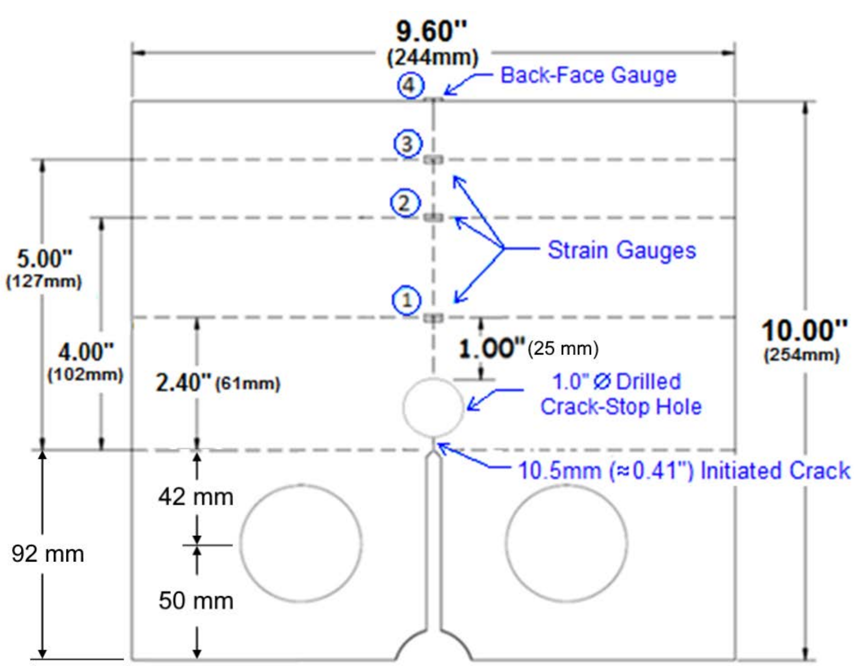

Figure 38. Fatigue test Specimen #2 with drilled crack-stop hole and strain gauges.

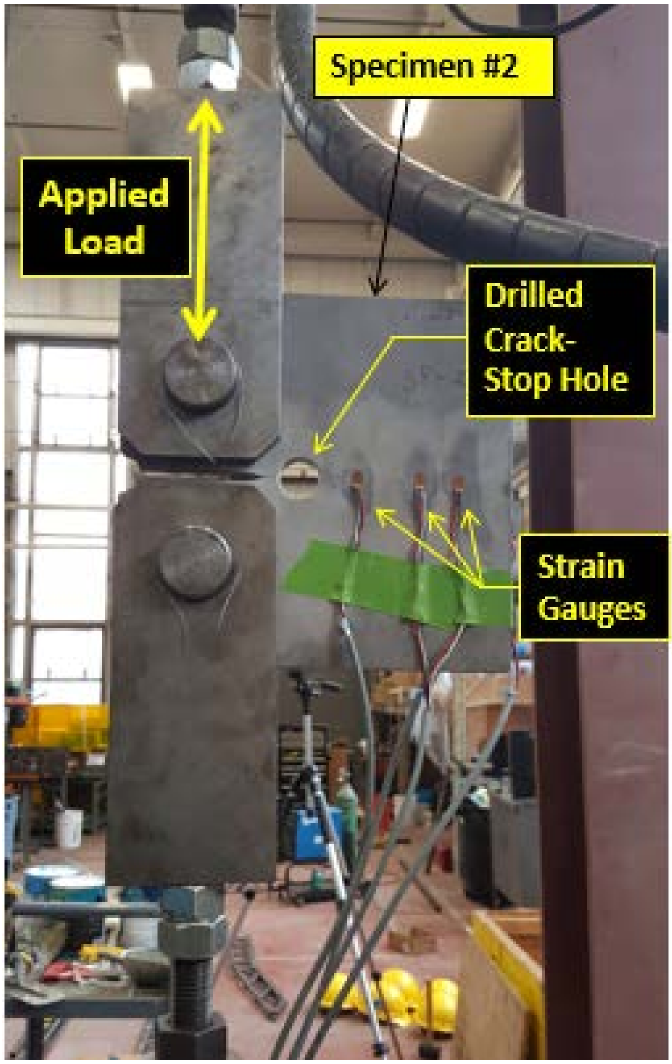

Figure 39. Drilled crack-stop hole experiment #2 Setup.

3.3.3 Rehabilitated Plate: Integrated Strengthening and Sensing (ISS) Composite (Specimen #3)

As stated earlier, the composite patch material selected for application in this research was M40J prepreg by Toray Composites (America), Inc. Due to its high Young's modulus this material was selected as a good candidate for steel as a rehabilitation. The overall objective of this third experiment was to demonstrate the effectiveness of the rehabilitation method and the ability of CNTs to detect fatigue crack growth.

The preliminary setup for testing involved the application of a CNT infused sensing layer, followed by bonding the structural composite patch to the steel specimen. The manufacturing of the sensing layer first involved the dispersion and coating of CNTs onto a 34 g/m^2 aramid non-woven fabric. This process encompasses the complete bath impregnation of the fabric into a CNT solution. Photographs taken during this process are shown in Appendix E. After CNT coating process, sheet was trimmed into two sheets measuring 203 mm x 90 mm (8.0 in x 3.54 in) for application to the steel specimen.

The composite patch was simultaneously fabricated employing the previously stated M40J material. Structural patch was comprised of a total of 22 ply. Each ply was 0.09 mm (0.0035 in) thick. Once each ply was laid-up, an autoclave was utilized in order to apply pressure and uniform temperature. The goal was to maintain a constant thickness of 1.75 mm (0.069 in). The final step involved cutting the composite laminate into two individual patches measuring 190 mm x 90 mm x 2 mm (7.48 in x 3.54 in x 0.079 in) thickness. The fabrication of two CNT sensing layers and two structural patches was accomplished in order to apply this rehabilitation patch to both sides of the cracked steel specimen in order maintain symmetry.

Hysol epoxy paste adhesive manufactured by Henkel was employed for application of the sensing layer in addition to the composite patch to steel. This two-part epoxy forms a strong bond and is said to be one of the toughened epoxy paste adhesive for bonding metal, wood, plastics and glass. The bonds that are formed are flexible and resist water, salt spray and most common fluids. The epoxy paste was applied to the sandblasted ASTM CT specimen in **Figure 34**. The sensing layer was then adhered to specimen, followed by the structural patch. In addition, strain gauges were mounted on the pre-cracked specimen prior to testing, as shown in **Figure 40**.

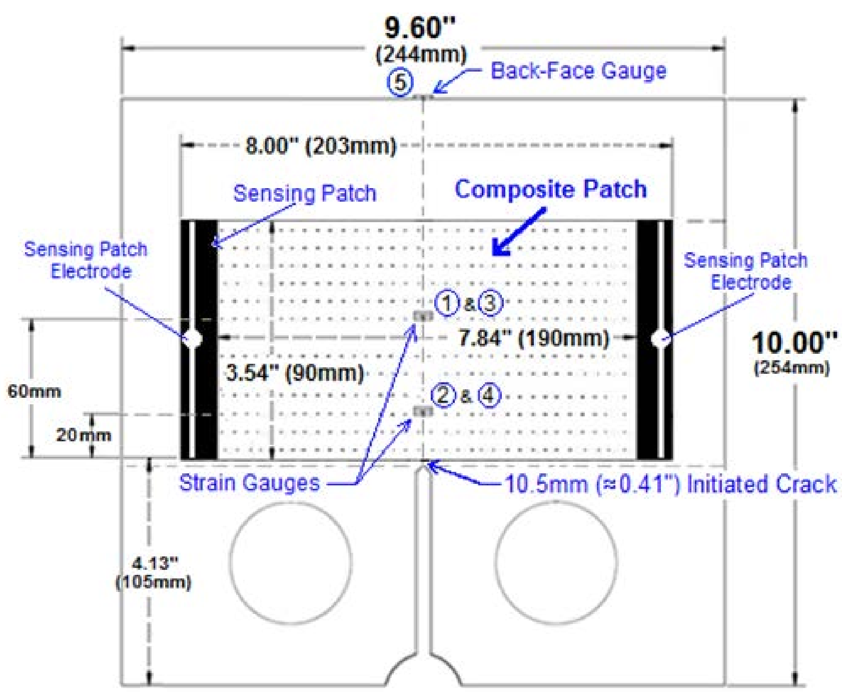

Figure 40. Fatigue test Specimen #3 with ISS composite and strain gauges.

Patch was initially placed in a manner which was hypothesized to most effectively transfer the load from steel to the composite in order to ultimately increase the overall fatigue life. Theoretically, in order to determine which, patch orientation would be most effective, numerous experiments would need to be performed. However, for the sake of time and the confinements of the research objective to simply demonstrate that this proposed rehabilitation method is viable, a single patch orientation was selected as shown in **Figure 40**. Numerous elements had to be considered in order to determine the patch location and orientation. Some of these included the location of the neutral axis prior to addition of patch, required bond area, debonding issues, plate dimensions, electrode positioning and location of crack mouth relative to patch edge. An example of this consideration is if patch was placed too close to crack mouth, where displacements are greatest, debonding of the patch will inevitably occur. In the instance were patch is positioned too far from crack, the neutral axis of specimen can be caused to shift up. As a result of these and numerous other scenarios, patch was positioned and placed as shown in **Figure 40**. Ultimately all concerns could not be addressed without running a series of tests solely on the effect of the patch location. However, considering the extent of this research, a single alignment was proposed and tested.

As in the case on experiment 1 and 2, Specimen #3 was mounted and cyclically loaded to failure at 2.5 Hz. Experimental setup is shown below in Figure 3.33.

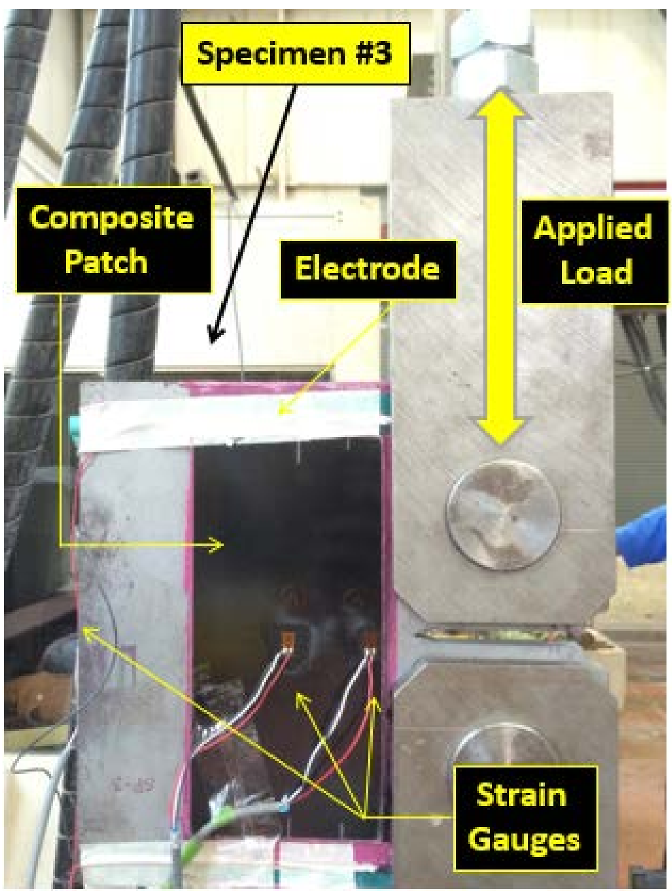

Figure 41. ISS Specimen experiment #3 Setup.

3.3.4 Rehabilitated Plate: Crack-Stop Hole and Integrated Strengthening and Sensing (ISS) Composite (Specimen #4)

This fourth and final specimen was manufactured in the same fashion as Specimen #3, which is discussed in Section 3.3.3. Prior to adhering the ISS composite patch, a crack-stop hole was drilled per Section 3.3.2. The location of the crack-stop hole is the same as shown in **Figure 38**.

The overall objective of this last experiment was to demonstrate the effectiveness of the rehabilitation method if combined with a crack-stop hole.

In addition, similar to the aforementioned experiments, the pre-cracked specimen was also mounted with strain gauges prior to the experiment as shown in **Figure 42**.

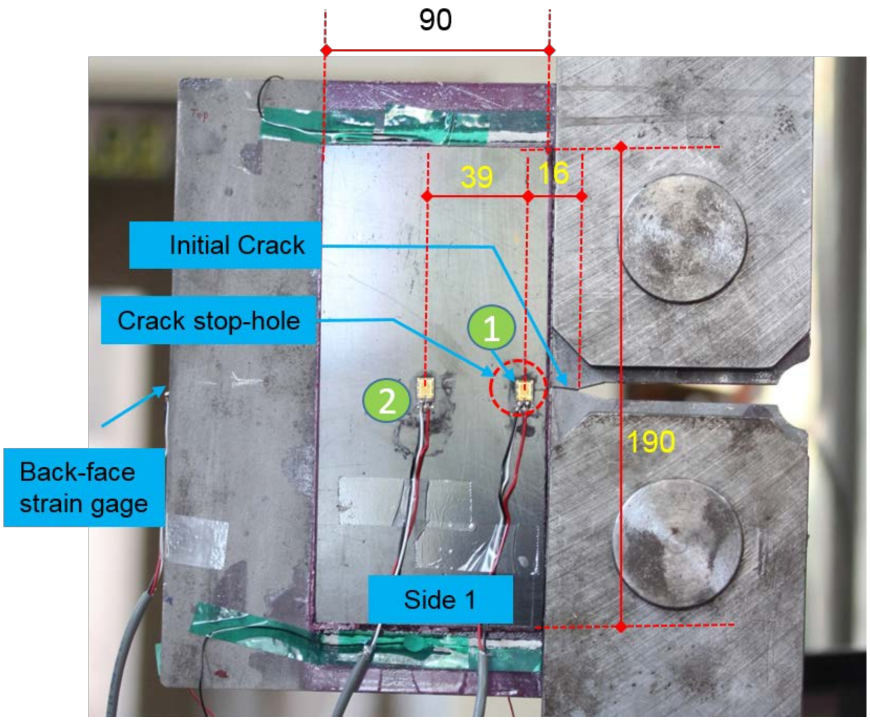

Figure 42. Crack-stop hole and ISS specimen experiment #4 setup.

4 Results and Discussion

4.1 In-Service Bridge Monitoring

The following section summarizes the results from the in-service monitoring of DelDOT Bridge 1678-006. As previously discussed in Section 3.1, this bridge was instrumented with twelve strain gauges in various locations and strain readings were taken for a period of two weeks. Upon completion of this data collection, plots were generated and a fatigue life analysis was performed in order to better understand the structure and the affect that cyclic loading has played on the remaining fatigue-prone details, and thus the bridge as currently configured.

4.1.1 Strain Readings

In order to condense the file sizes created by the recorded data, data collection was divided into individual recording sessions. Each session sampled for about 48 hours. This was done employing burst sampling settings, which recorded for ten minute intervals and then ceased recording for twenty minutes before beginning to sample data again. Session 1 was initiated May 5th, followed by session 2 on May 7th, session 3 began on May 9th and session 4 started on May 13th. A sampling rate of 32 Hz was implemented for this study. In addition, as detailed in Section 3.1.4, each individual node was responsible for recording four of the 12 strain gauges mounted on the structure. The identification numbers for the three nodes used in this study are Node 30343, Node 30344 and Node 33201. Plots were generated for each of the strain gauges for each node recorded during each of the sampling sessions. **Figure 43** to **Figure 46** illustrate a sample of the strain readings recorded from the Channel 1 of Node 30343. Referencing **Figure 19**, this is strain gauge #4 located perpendicular to the tip of the crack tip.

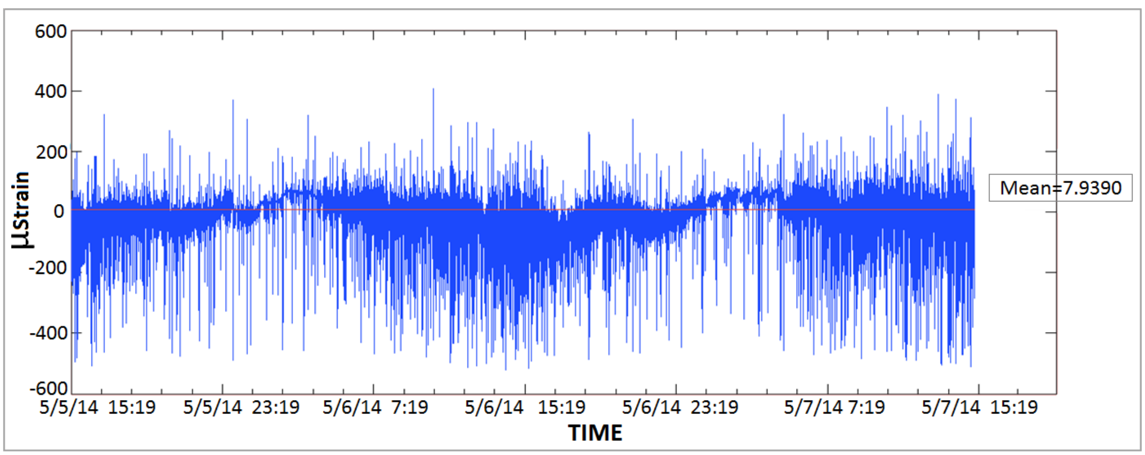

Figure 43. Node 30343 – Channel 1 - Session 1.

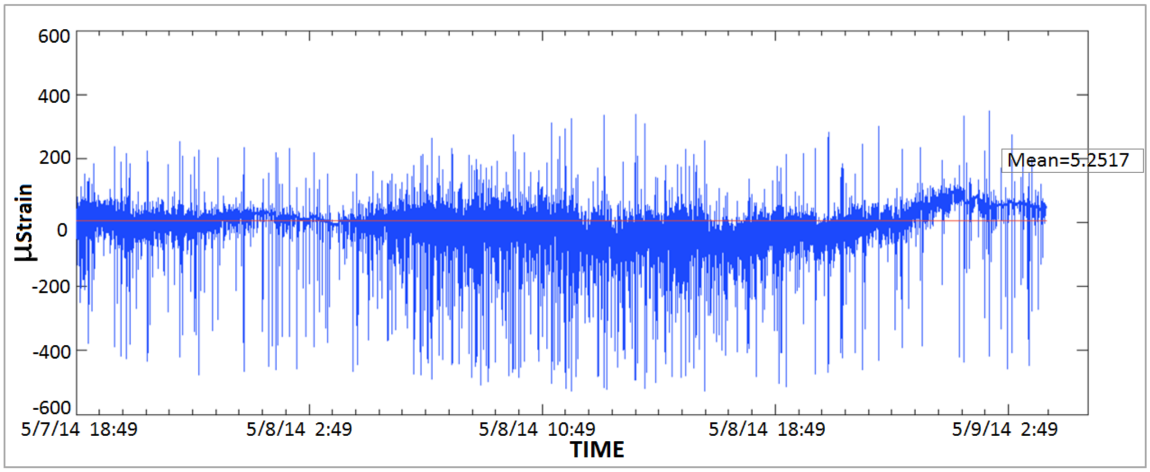

Figure 44. Node 30343 – Channel 1 - Session 2.

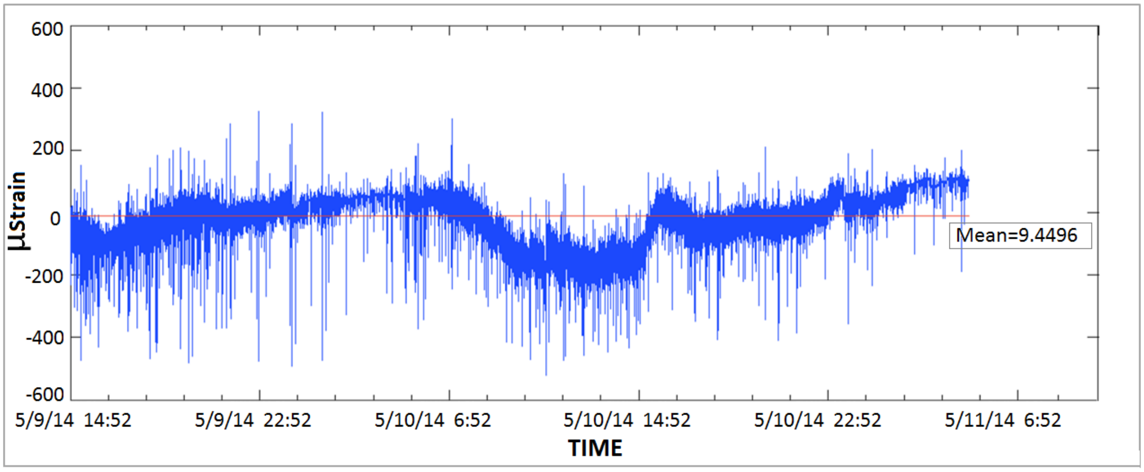

Figure 45. Node 30343 – Channel 1 - Session 3.

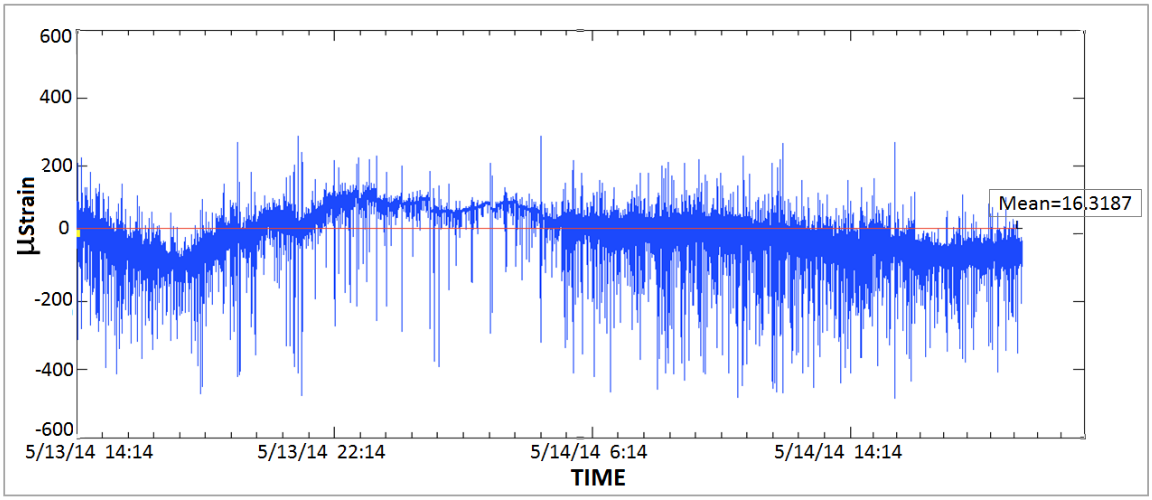

Figure 46. Node 30343 – Channel 1 - Session 4.

Plots are displayed as strain (με) vs. time (s) on the y- and x-axis, respectively. The red horizontal line symbolizes 0 microstrain (με), though this does not depict the actual origin by which negative and positive strain are determined. It is a result of the inability to stop traffic on the bridge prior to calibrating software for strain reading. Although the origin may be close to zero, it cannot be assumed to be exactly zero.

Observation of the plots generally illustrate higher amplitude strain recorded during certain times of the day, particularly daytime travel times. This is consistent with the ideology that more traffic occurs during peak hours of the early morning commute and then repeats for the evening rush hour. As shown in **Figure 43** to **Figure 46**, there is increased amplitude strain ranges beginning around morning rush hour and extending through the daylight hours to the evening commute. Night hours showed the lowest frequency of high amplitude strain ranges throughout the sampling sessions.

A notable difference in strain readings suggesting an instrumentation malfunction is shown in **Figure 47**, which is Channel 4 of Node 30343. This graph depicts a jump in sampling data between session 3 and session 4 of approximately 600 με. The data collected in session 4 of channel 4 node 343 showed extremely higher values of strain than the first three sessions. This type of irregularity in the data was the only case amongst all other plots besides channel 2 of Node 33201. As depicted in **Figure 48**, this channel also experiences a jump between Session 3 and 4, but this abnormality was not as extreme as in the case of Node 30343. Although other channels did experience variations in mean oscillation between and within sessions, this specific extreme event was not observed other than in these two anomalies.

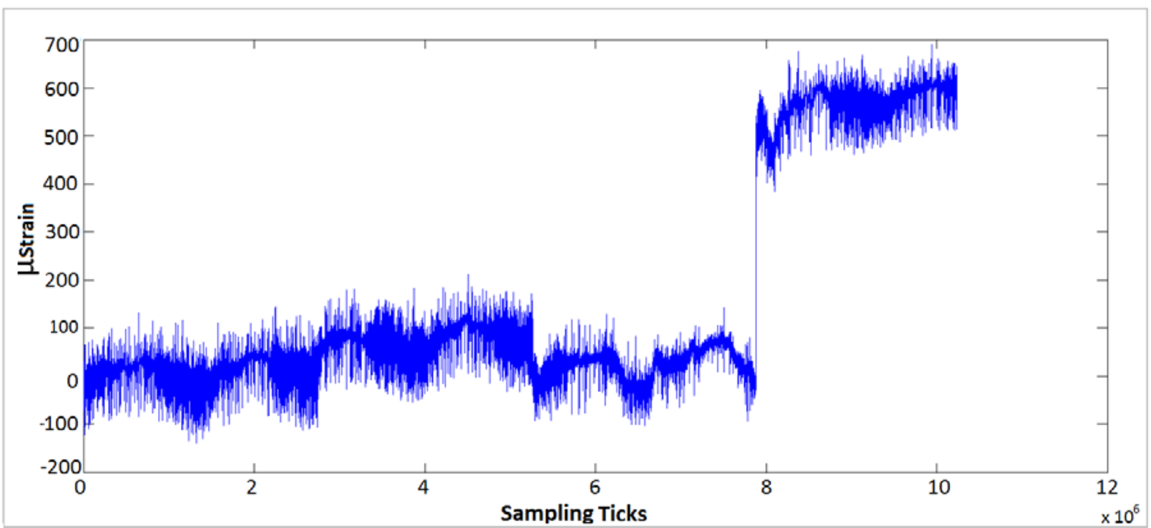

Figure 47. Data irregularity in Node 30343 – Channel 4.

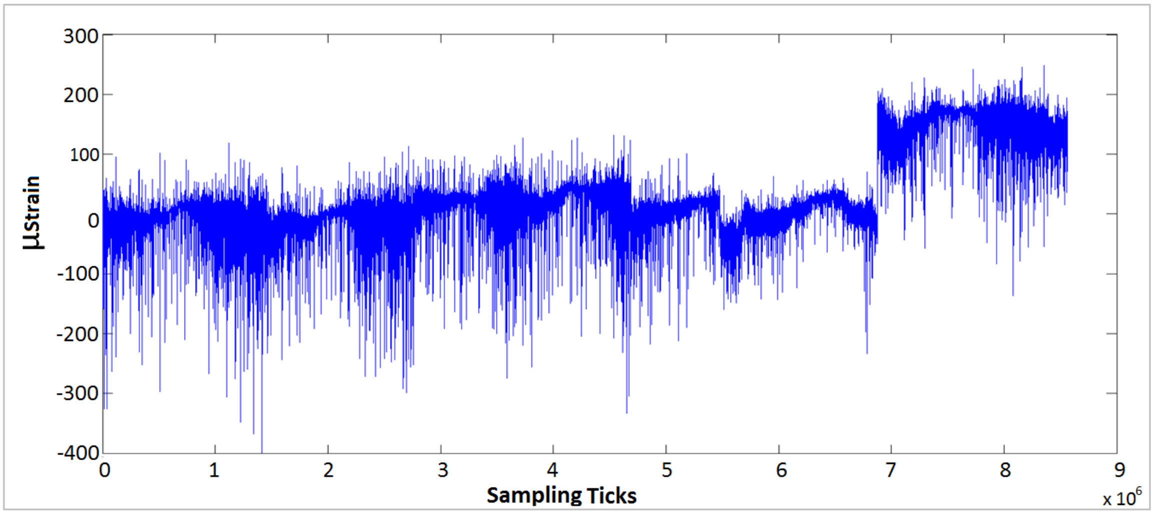

Figure 48. Data irregularity in Node 33201 – Channel 2.

It was also witnessed for many of the plots of a repetitive, irregular oscillatory motion. Examples are illustrated in **Figure 49** and **Figure 50**. These two worst case instances reference strain Gauge #5 (of the strain rosette on East Face of Beam 3) and Gauge #12 (West Face of Beam 4 on Span 5). These deviations are believed to be a result of temperature variations throughout the day. Each *strain gauge* produces a *temperature*-dependent measurement signal. Due to the sensitivity of strain gauges, thermal expansion and contraction of the bridge girder consequently led to the drift in strain readings as shown below. The data can be corrected by measuring the temperature and employing a thermal correction curve available through the manufacturer. But for the purpose of this study, these variations were ignored. Ultimately we are just interested in determining the actual stress cycles and not the absolute values. The overall differences between maximum and minimum values do not change as a result of the slow-varying temperature.

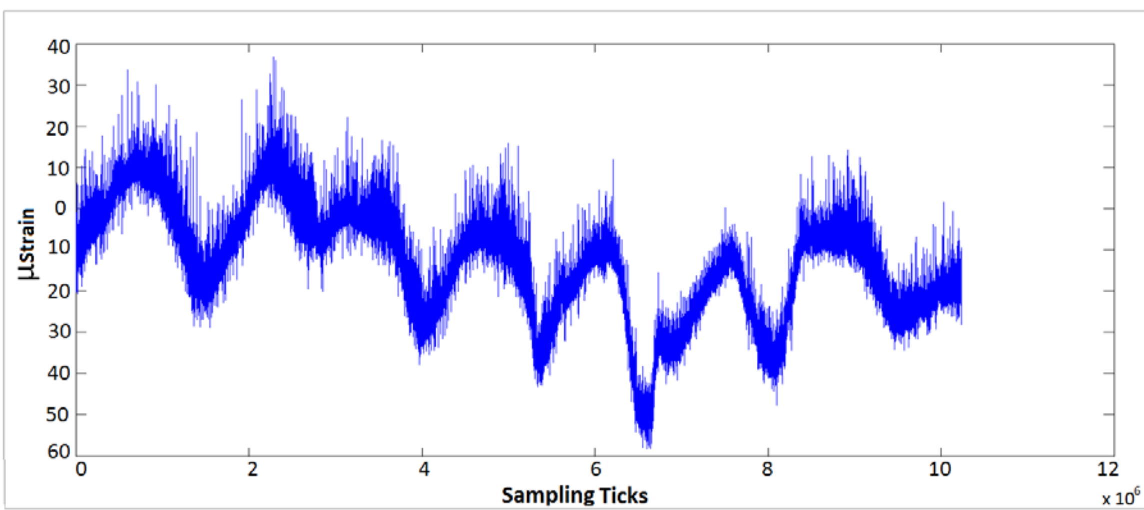

Figure 49. Example of irregular oscillatory motion [Node 30343 – Channel 3].

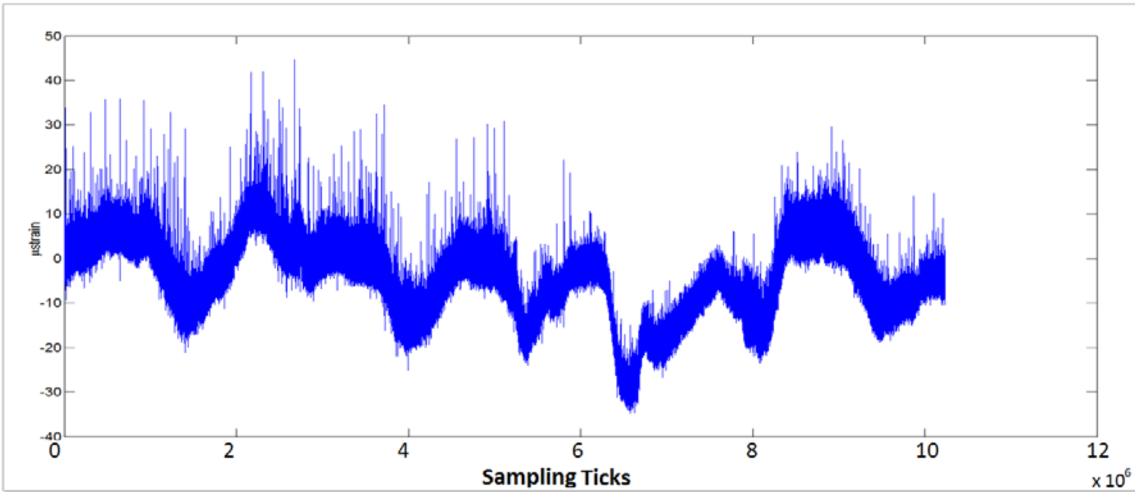

Figure 50. Example of irregular oscillatory motion [Node 30344 – Channel 4].

The full data views in **Figure 43** to **Figure 50** were helpful in the determination of the general trend of the strains. However, in order to draw conclusions of the individual strain gauges, the plot had to be further inspected. A sample examination of a strain recorded over a two second interval is shown below. Note brackets in the legend indicate the actual gauge number. Please reference **Figure 19** and in Chapter 3 for specific gauge locations.

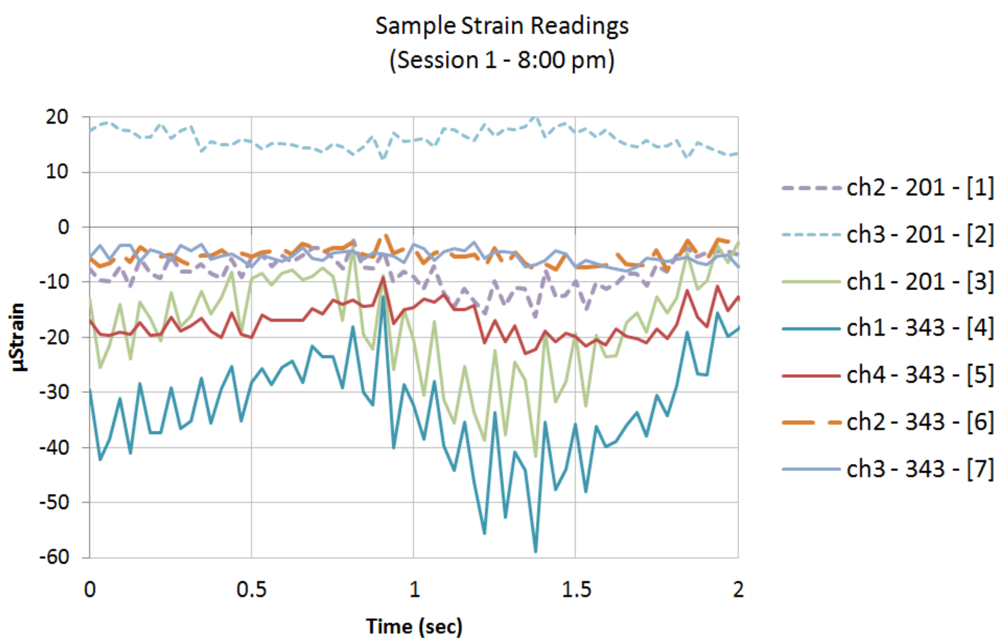

Figure 51. Sample strain readings - East Face of Beam 3 on Span 5.

This example is taken from the east face of Beam 3 and was recorded during sampling session 1 at 8:00 pm. It illustrates the readings of all strain gauges located on this particular face of Beam 3. Gauges located below the neutral axis are in tension (Gauge 1) and every gauge above it is in compression (Gauges 3-7). In addition, the initial hypothesis was that the strain experienced by any individual gauge should be greatest near the crack tip and decrease moving away from crack. This premise is confirmed in **Figure 51**. Across this two second time interval, Gauge 4 experienced the largest strain values. Referencing the previous strain gauge instrumentation plan displayed in **Figure 19**, this strain gauge is positioned 13 mm (0.5 in) from the crack-stop hole and projected crack tip. Furthermore, Gauge 7 sensed the least strain and, coincidentally recalling **Figure 19** again, this gauge is located the furthest from the crack tip. These observations, for the most part, carry throughout all plots when examined over incremental intervals. Therefore, it can be concluded from this study in addition to a previous laboratory testing conducted at the University of Delaware that compared calculating stresses of a steel beam subjected to applied loading to values taken from the data acquisition system, that this monitoring system is capturing realistic strains experienced by this structure throughout the day.

Figure 52 and **Figure 53** apply this same technique displaying the raw strains experienced over a period of a condensed time interval at different times of the day. These plots however, illustrate the differences between recorded strains for gauges positioned at the same location on opposite girders and opposite faces of the girders. Essentially one can begin to draw conclusions about the strains experienced by the damaged girder opposed to that of the "healthy girder."

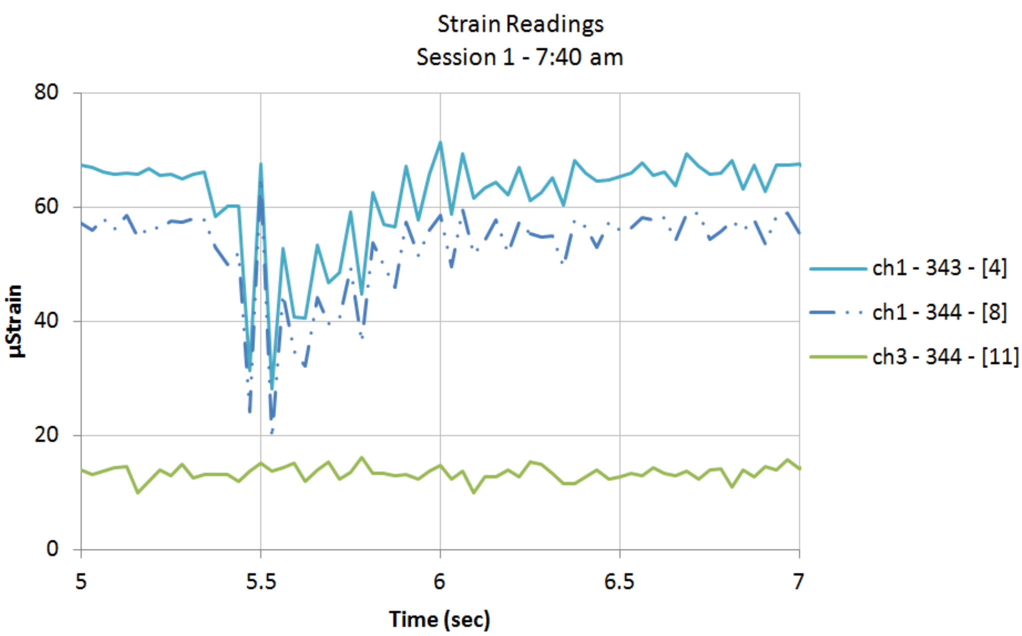

Figure 52. Sample strain readings comparisons – Session 1- 7:40 am.

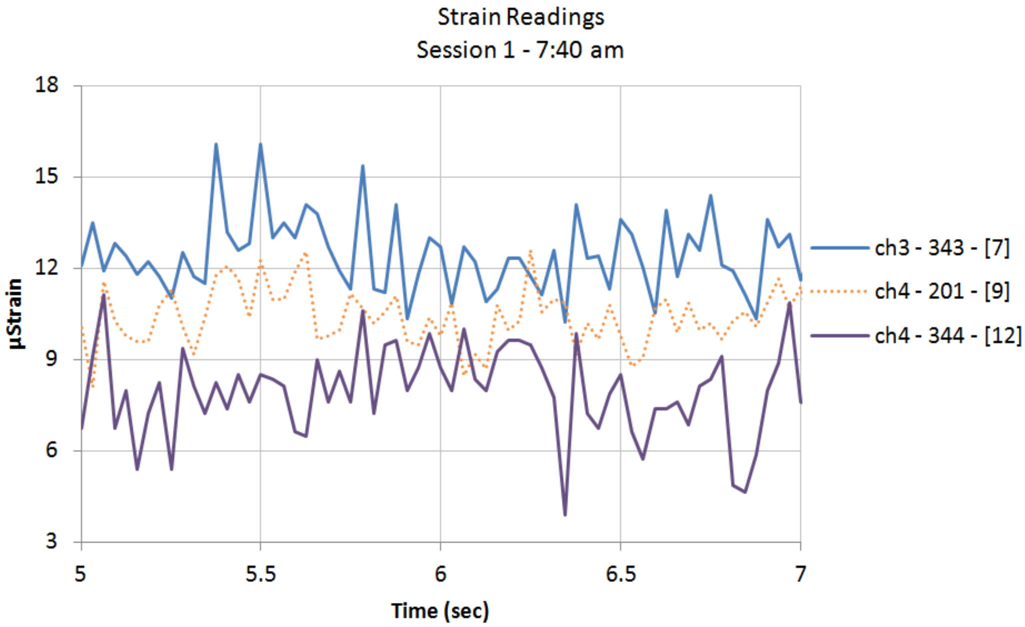

Figure 53. Sample strain readings – Session 1- 7:40 am.

Figure 52 and **Figure 53** are from Session 1 at 7:40am. The time interval essentially corresponds to that of the morning rush hour. **Figure 52** displays gauges 4, 8 and 11 centrally located 197 mm (7.75 in) from the bottom flange. Gauges 4 and 8 are welded on opposite faces to beam 3, which has been found to have multiple fatigue cracks. Gauge 11 is located on beam 4, the healthier girder, exhibiting no visible fatigue cracking issues. It is noted that Gauges 4 and 8 exhibit much higher strains than that of Gauge 11. This is to be expected as Gauge 11 is on the "healthy girder." In addition, the strain gauges positioned on Beam 3 both follow the same trend and display similar strain readings. This observation coincides with initial expectations of these gauges experiencing similar strains as they are on opposite sides of the same girder.

Figure 53 reports the data from Gauges 7, 9 and 12, which are all located 368 mm (14.5 in) from the bottom flange. As in the previous case, the "healthier girder" (Gauges 12) has been shown to sense less strain. However, when comparing the gauges on opposite faces of Beam 3, for this instantaneous point in time, Gauge 7 and 9 do not appear to experience the same strains. At first glance, this result deviates from original expectations as they are located in the same position from the of bottom flange. But one must also have considered that as these gauges are located further from the crack tip, thus the strain readings are lower. Therefore, comparing the actual difference between strains of parallel gauges, the results are actually quite similar to previously discussed. In addition, one must consider these are very small strains; only slightly above noise level readings. Therefore, these deviations are minuscule. Thus the initial theory for both cases is confirmed.

Overall, although there were some discrepancies in the recorded data, the monitoring system was generally able to accurately record the strains experienced by DelDOT 1678-006. From this data it was possible to infer information in reference to the current state of the structure. Recorded data allowed for a foundation in which to begin building our laboratory study.

4.1.2 Potentiometers

As discussed in Section 3.1.3, two potentiometers were employed in the field monitoring of DelDOT 1678-006. These gauges allowed for displacement measurements to be taken as the crack opened and closed due to the traffic. Similar to that of the strain readings, **Figure 54** depicts the readings taken by the gauges plotted as displacement (mm) vs. sampling ticks. As can be observed, the crack motions did not experience irregularities as seen in the strain data.

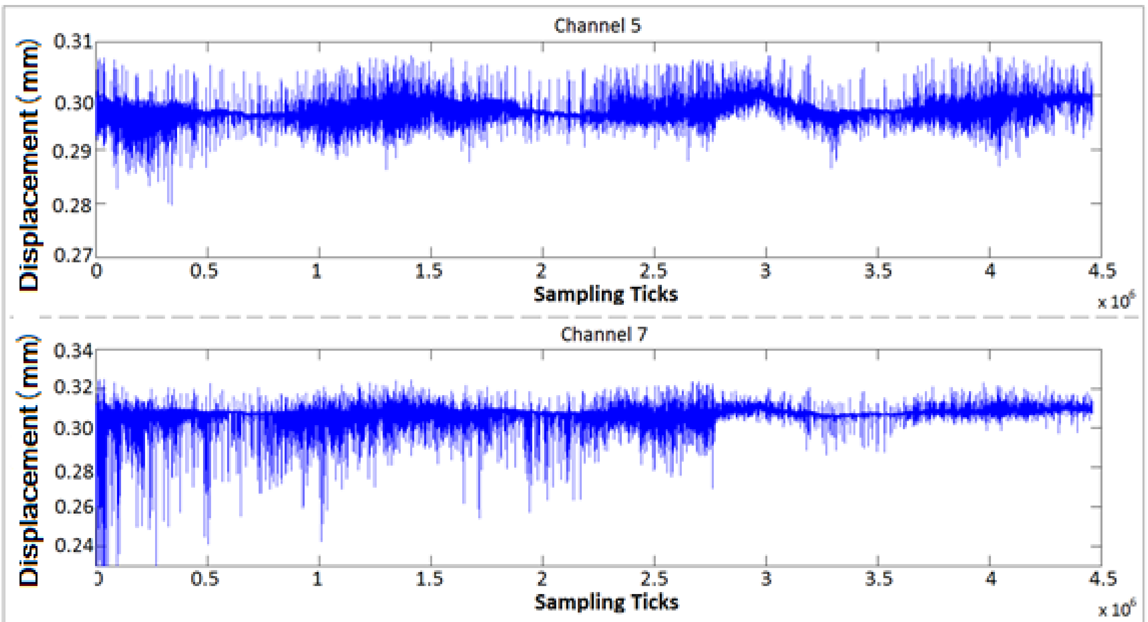

Figure 54. Potentiometer readings.

Both potentiometers were wired to Node 33201. Referencing **Figure 19** of Chapter 3, Channel 5 of this node corresponds to the gauge located near the middle of the crack. Channel 7 is located near the site of the crack initiation.

Examining Channel 5, the periods of larger displacements appear to be consistent with the hourly traffic. The greater motions occur during morning commuting times and evening rush hour. This observation agrees with what was displayed from the strain readings. Referencing Channel 7, it appears that the displacement measurements tend to decrease over time. It starts with a rather large displacement range of about 0.12 mm (0.005 in) occurring at the beginning of the data record. Ranges drastically drop off towards to end of the recording session. More research is required in order to further draw conclusions related to results of these potentiometer measurements. But ultimately these gauges were simply employed in order to gain a general understanding of the amount of crack mouth opening displacement (CMOD) for this in-service structure.

4.1.3 Fatigue Life Analysis

Fatigue crack development and propagation occurs as a result of repetitive cyclic loading. In order to determine the fatigue life associated with this structure, the number of cycles had to first be calculated for the different stress ranges experienced at the instrumented locations. Assuming the loading and response is consistent throughout the year, the number of cycles experienced per year could ultimately be estimated. As mentioned in Section 3.2, the numerical analysis employed for this research incorporated two of the cycle counting strategies presented by ASTM E1049-85 in order to form cumulative fatigue damage conclusions. Data collected from 12 different sensors monitoring the bridge were analyzed using the Rainflow counting algorithm, simple range counting (full cycle counting), and simple range counting (half cycle counting) methods. The corresponding Miner's number for each channel was also calculated to find the fatigue life of the bridge. In order to organize findings, histogram plots and data tables were generated for all strain sensors employed in this study. It should also be noted that bin sizes selected for production of histogram plots were determined employing Scott's Rule (Scott 1979).

In order to provide a visual representation of the stress ranges experienced by a particular gauge, a sample histogram depicting the stress ranges and the frequencies at which they occur for Channel 1 of Node 30343 is displayed in **Figure 55**. This plot shows the results of each counting method used; Rainflow counting, simple range counting (full cycle counting), and simple range counting (half cycle counting) methods extrapolated to 25 years. Only stress ranges greater or equal to 31 MPa (4.5 ksi) were examined, as previously stated in Section 3.2.1, for the connection in question 31 MPa (4.5 ksi) is the threshold corresponding to infinite fatigue life. Any value below this ultimately will not contribute to the development of fatigue damage.

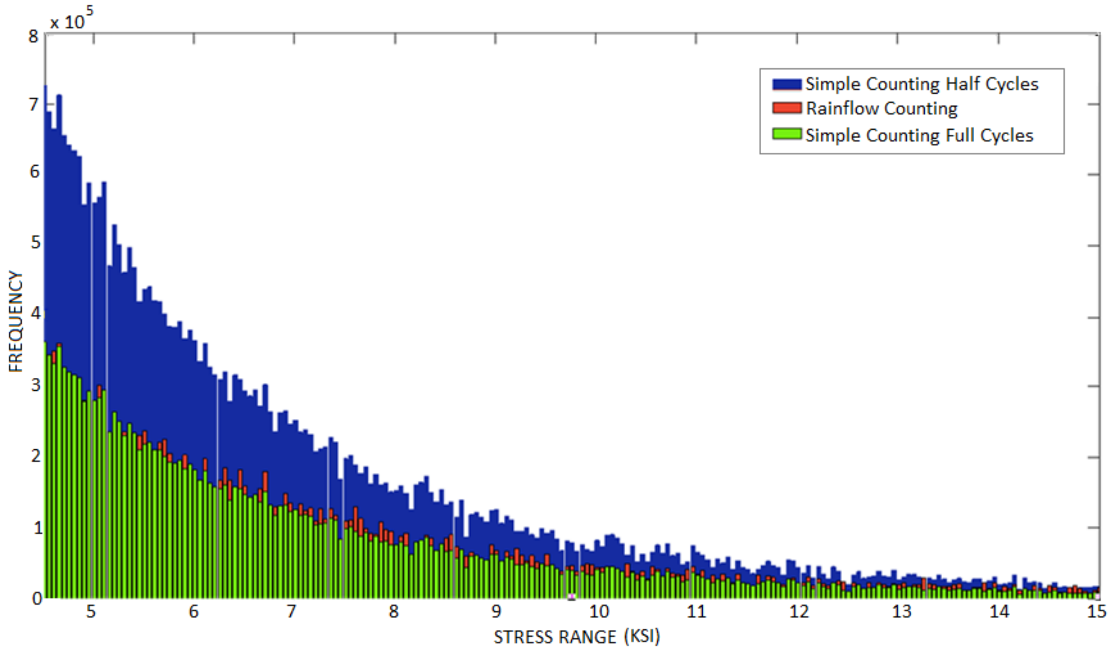

Figure 55. Counting algorithm histogram.

The Rainflow counting and full cycle strategies defined in the ASTM standards were weighed more heavily in this evaluation, with the half cycle analysis included for reference. Rainflow and full cycle stress range counting in **Figure 55** display a relatively strong correlation. As anticipated, the Rainflow counting method displays a slightly higher damage model prediction than the full cycle simple counting method. However, this is only the case when considering stress ranges greater than 31 MPa (4.5 ksi). Although not depicted on the graph, for ranges less than 31 MPa (4.5 ksi), full cycle counting method obtained generally higher frequencies than that of Rainflow counting method. Oscillatory noise and low level stress applications will result in the simple counting method recording higher relative low level stress frequencies, while underestimating larger stress range applications. The general overall exponentially decaying trend is consistent amongst all counting methods.

Examination of histogram plots more thoroughly reveal that the majority of cycles occurring at stress levels less than 31 MPa (4.5 ksi). While for the case of Channel 1 of Node 30343, **Figure 56** reveals the overall maxium to be 174 MPa (25.3 ksi). This plot is of the raw data for the all recording sessions. Although the maximum stress can be considered to be quite large, one must consider the fact that this value occurs possibly once or twice. The number of these cycles compared to that of the smaller stresses is insignificant. The more substantial risk to fatigue crack propagation is due to the smaller repetitive loads as opposed to a few heavy loads. Referencing **Figure 56** once again, although cycles are exponentially decreasing, it should be noted that there are still thousands of cycles greater than 31 MPa (4.5 ksi). This may be detrimental to the structure considering that this data was recorded for less than 200 hours. Please refer to Appendix C for remaining histogram plot for all strain gauges.

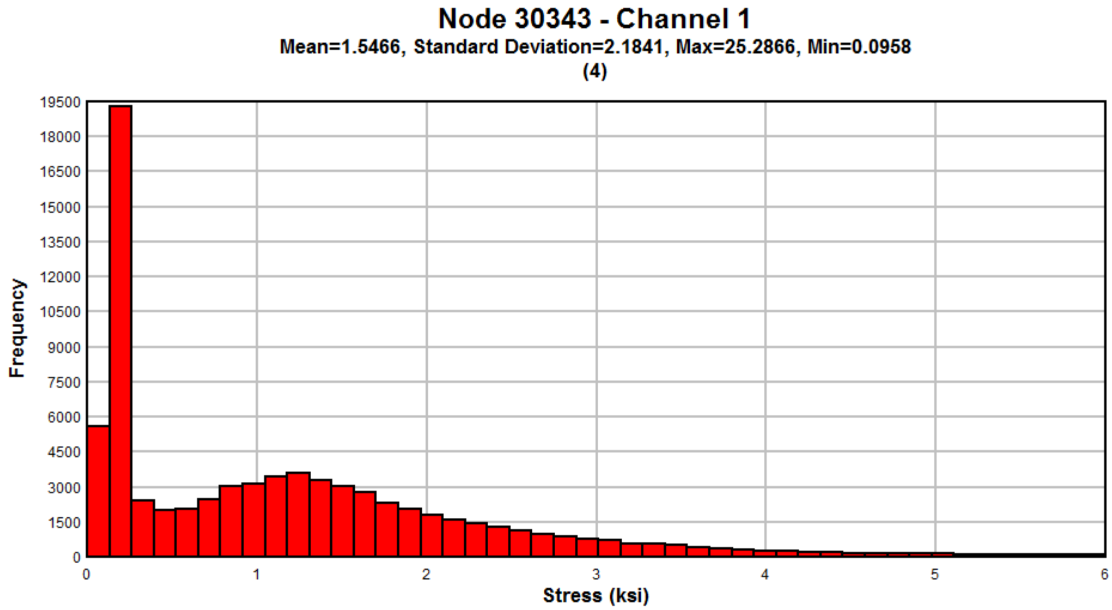

Figure 56. Raw data histogram plot.

As previously discussed in this chapter, in order to provide numerical results, each channel (strain sensor) employed on DelDOT 1678-006 was analyzed using Rainflow counting, simple range counting (full-cycles) and simple range counting (half-cycles). In addition, the maximum stress range in ksi was tabulated. Using Miner's equation as discussed in Section 3.2.2, Miner's number and the corresponding anticipated fatigue life was calculated for each channel. To execute this calculation with quantities for which the physical significance was more readily apparent, the cycles counted during the monitoring period were linearly extrapolated to compute the number of cycles that would occur over 25 years (assuming no change in traffic; simply for mathematical purposes). The fatigue life is then the ratio between 25 and Miner's number. The fatigue life is then the ratio between 25 and the resulting Miner's number. These formulated values have been organized and are shown in **Table 8**.

Table 8. Data analysis results.

Gauge Number	Node Channel	RAINFLOW COUNTING			SIMPLE RANGE COUNTING (Full Cycles)			SIMPLE RANGE COUNTING (Half Cycles)		
		Max Stress Range (ksi)	Miner's Number	Fatigue Life (Years)	Max Stress Range (ksi)	Miner's Number	Fatigue Life (Years)	Max Stress Range (ksi)	Miner's Number	Fatigue Life (Years)
Node 343										
4	Ch1	27.125	26.443	0.945	24.906	21.331	1.172	24.906	42.662	0.586
6	Ch2	4.126	0	∞	3.715	0	∞	3.715	0	∞
7	Ch3	2.758	0	∞	0.966	0	∞	0.966	0	∞
3	Ch4	10.194	0.085	293.772	6.492	0.023	1106.195	6.492	0.045	553.097
Node 344										
8	Ch1	25.102	22.670	1.103	24.751	18.389	1.360	24.751	36.778	0.680
10	Ch2	5.498	0	29002.657	4.122	0	∞	4.122	0	∞
11	Ch3	2.309	0	∞	1.696	0	∞	1.696	0	∞
12	Ch4	2.308	0	∞	1.317	0	∞	1.317	0	∞
Node 201										
5	Ch1	26.369	18.512	1.351	24.177	14.178	1.763	24.177	28.355	0.882
2	Ch2	18.805	0.681	36.732	12.747	0.461	54.195	12.747	0.923	27.100
1	Ch3	6.309	0.019	1315.789	5.864	0.008	3048.780	5.864	0.016	1524.390
9	Ch4	2.694	0	∞	1.645	0	∞	1.645	0	∞

As shown in **Table 8**, in cases where the stress ranges are less than 4.5 ksi, the fatigue life is infinite in accordance with AASHTO LRFD Bridge Design Specifications (AASHTO 2010). In addition, Miner's number is essentially equivalent to zero for these gauges as the comparison of experimental stresses to the allowable stresses is low.

The results are consistent with initial hypothesis that the stress decreases as you move away from the fatigue crack mouth. The highest of these values occurring directly at the tip of the crack (Gauge 4). In addition, the calculated fatigue life is lowest that this location. This is ultimately the worst case scenario. As presented in **Table 8**, the value associated with the lowest fatigue life for this section employing Rainflow counting method is a low 0.945 years. Even employing the other counting methods, the fatigue life is still relatively low.

Comparing values obtained from strain gauges located in the same location on different girders/faces, the fatigue life values are about the same. Referencing instrumentation plans in **Figure 19** & **Figure 20**, strain Gauges 7, 9, and 12 are all located 368 mm (14.5 in) from the bottom flange. Therefore, theoretically one would expect for these locations to have the same fatigue life. As denoted in **Table 8**, this philosophy holds true as the tabulated fatigue life is theoretically infinite. In addition, maximum stresses ranges only deviate 0.24 from their mean. Similarly, Gauges 4, 8 and 11 are all located 197 mm (7.75 in) from the bottom flange. Gauges 4 & 8, which are located near the crack tip, values parallel each other; while the expected fatigue life at the location of Gauge 11 is infinitely higher. This is attributed to Gauge 11's location on the "healthy girder" while the remaining two are positioned near the tip of the crack. This comparison illustrates the differences the stress ranges experienced and ultimately the fatigue life of a "healthy girder" vs. a "damaged girder."

Overall, cumulative fatigue analysis through Miner's number showed varying fatigue life and stress range distributions throughout the channels. However, observation shows a direct correlation between location of the sensor in terms of distance from the crack mouth and ensuing fatigue life. The highest stress range (and therefore lowest fatigue life) occurred, as predicted and previously discussed, at strain gauge 4. This gauge was the closest to the crack mouth. Additional comparing the beam 3 (girder with fatigue crack) to Beam 4 ("healthy girder" without fatigue damage) early predictions held true. For each gauge placed on Beam 4, all results illustrated an infinite fatigue life by failing to incur maximum stress ranges of more than the 31 MPa (4.5 ksi) threshold. Results demonstrate that this girder is in fact a "healthy girder," with no reasonable suspicion of development of any fatigue related damage in the near future. This is based on readings recorded at the instrumented locations.

In addition to analyzing the cumulative damage experience by each channel, each session was also analyzed individually as a result of discrepancies discussed in Section 4.1.1. Ideally, the cumulative fatigue calculations for the entire recorded dataset should parallel that of the individually analyzed sessions. Results of this investigation are presented in **Table 9**.

Upon computation of the average amongst each individual sampling session, results signify that Miner's numbers are actually quite comparable to that of the compounded data set containing all four sessions. However, when further analyzing each session's tabulated values some inconsistencies do arise. As data was generally recorded over the similar time period, it is hypothesized that values between sessions should remain relatively constant. The most notable change in fatigue life occurs during Session 3 for the majority of the channels, exhibiting a substantially higher fatigue life than other data sessions. The variation may however be attributed to the days of the week of data collection. Unlike the others, Session 3 was set to record from Friday afternoon until early Sunday morning; times when truck traffic volumes are expected to be substantially lower than during working hours. Also, of the data collected during session 3, ~58% was obtained between the hours of 7:00 p.m. and 7:00 a.m., resulting in an unrepresentative, and underestimated, sampling of stress conditions for extrapolation. The remaining night collection proportions for Session 1, 2, and 4 are ~52%, ~62%, ~41% respectively. These slight disproportionalities in sampling conditions are exacerbated when multiplied over a 25-year period.

Table 9. Data analysis results by individual sampling Session.

Sampling Session	RAINFLOW COUNTING											
	Max Stress Range (ksi)	Miner's Number	Fatigue Life (Years)	Max Stress Range (ksi)	Miner's Number	Fatigue Life (Years)	Max Stress Range (ksi)	Miner's Number	Fatigue Life (Years)	Max Stress Range (ksi)	Miner's Number	Fatigue Life (Years)
Node 343												
	Ch1			Ch2			Ch3			Ch4		
1	26.939	38.217	0.654	3.928	0	∞	1.907	0	∞	8.269	0.124	201.237
2	25.420	35.314	0.708	3.637	0	∞	1.740	0	∞	7.720	0.099	252.521
3	24.497	10.374	2.410	3.500	0	∞	2.039	0	∞	6.737	0.022	1126.026
4	22.389	20.507	1.219	3.399	0	∞	1.794	0	∞	8.455	0.047	530.803
AVG	24.811	26.103	**1.248**	3.616	0	∞	1.870	0	∞	7.795	0.073	**527.647**
Node 344												
	Ch1			Ch2			Ch3			Ch4		
1	25.102	33.521	0.746	5.498	0.003	7949.650	2.286	0	∞	1.910	0	∞
2	24.276	30.134	0.830	4.274	0	∞	1.743	0	∞	1.729	0	∞
3	22.455	8.475	2.950	3.612	0	∞	1.480	0	∞	1.650	0	∞
4	20.904	17.457	1.432	3.790	0	∞	1.381	0	∞	1.541	0	∞
AVG	23.184	22.397	**1.489**	4.294	0.001	∞	1.722	0	∞	1.708	0	∞
Node 201												
	Ch1			Ch2			Ch3			Ch4		
1	26.369	27.176	0.920	15.029	1.085	23.041	6.289	0.038	656.843	1.905	0	∞
2	24.776	22.871	1.093	13.478	0.914	27.351	5.803	0.022	1150.526	1.885	0	∞
3	21.144	6.288	3.976	9.699	0.180	138.576	5.144	0.003	9935.436	1.451	0	∞
4	23.438	14.203	1.760	11.177	0.297	84.069	5.245	0.002	13093.111	1.772	0	∞
AVG	23.932	17.635	**1.937**	12.346	0.619	**68.259**	5.620	0.016	**6208.979**	1.753	0	∞

Recalling the irregularities shown in **Figure 47** and **Figure 48**, session was additionally re-analyzed employing only sampling Sessions 1-3 in order to assess the potential influence of the irregularities on the study's conclusions. Referencing these diagrams, there was a large spike in the strain data that was experience between Session 3 and Session 4. Consequently, in order to determine the of this, the data analysis was repeated ignoring Session 4. Results of the re-evaluated data are displayed below in **Table 10**.

Table 10. Data analysis results of Sessions 1-3.

Gauge Number	Node Channel	RAINFLOW COUNTING			SIMPLE RANGE COUNTING (Full Cycles)			SIMPLE RANGE COUNTING (Half Cycles)		
		Max Stress Range (ksi)	Miner's Number	Fatigue Life (Years)	Max Stress Range (ksi)	Miner's Number	Fatigue Life (Years)	Max Stress Range (ksi)	Miner's Number	Fatigue Life (Years)
Node 343										
4	Ch1	27.125	28.529	**0.876**	24.906	23.325	1.072	24.906	46.651	0.536
6	Ch2	4.126	0	**∞**	3.715	0	∞	3.715	0	∞
7	Ch3	2.758	0	**∞**	0.966	0	∞	0.966	0	∞
3	Ch4	10.194	0.086	**290.360**	6.492	0.024	1063.830	6.492	0.047	531.915
Node 344										
8	Ch1	25.102	24.589	**1.017**	24.751	20.228	1.236	24.751	40.456	0.618
10	Ch2	5.498	0.001	**19230.769**	4.122	0	∞	4.122	0	∞
11	Ch3	2.309	0	**∞**	1.696	0	∞	1.696	0	∞
12	Ch4	2.309	0	**∞**	1.317	0	∞	1.317	0	∞
Node 201										
5	Ch1	26.369	19.314	**1.294**	24.177	14.965	1.671	24.177	29.930	0.835
2	Ch2	15.414	0.750	**33.351**	12.747	0.543	46.024	12.747	1.047	23.885
1	Ch3	6.309	0.023	**1111.111**	5.864	0.010	2500.000	5.864	0.020	1256.281
9	Ch4	2.229	0	**∞**	1.645	0	∞	1.645	0	∞

Comparing **Table 10** to the original **Table 8**, only slight variations in the projected fatigue damage are revealed. Due to the aforementioned variations in actual sampling times, Session 4 generally exhibited lower rates of fatigue damage. The exclusion of Session 4 resulted in an increase in average projected cumulative fatigue damage in comparison to **Table 8**. Discarding data from Session 4 lends to a more reliable data set, as unexplained irregularities in the data are excluded. However, discarding Session 4 may also lead to over-estimated damage predictions, as the weight of weekend collection times will become disproportionally high. Weekend traffic conditions will be represented by one out of three sessions, compared to an actual two out of seven-day distribution. Therefore, it can be concluded that **Table 8** presents the most accurate and proportionally precise results to the analysis of the in-service monitoring of DelDOT 1678-006. Nevertheless, considering such a small segment of sampling data was extrapolated to determine the fatigue life, this should be viewed as only an estimate. Greater periods of sampling are required in order to accurately estimate remaining fatigue life of this member. However, considering the results do indicate an estimated remaining fatigue life of less than a year there is a significant cause for concern.

4.2 Summary and Discussion

From the results of the field instrumentation and subsequent fatigue analysis, it can be concluded that the girder detail close to the support that is present in DelDOT Bridge 1678-006 possesses a significant fatigue prone detail that will continue to see considerable fatigue damage in the future. Stress range analysis shows substantial cumulative fatigue damage during short interval collection time frames that may cause severe damage. Although by the simple calculations presented in Appendix D, a 29.3 mm (1.15 in) in diameter should be sufficient to cease crack propagation, due to the complex loading experienced at the location in question, it is likely that the crack will eventually continue to grow. This conclusion is drawn from the large displacements in addition to the strain readings taken adjacent to the edge of the drilled hole and subsequent data analysis. In order to improve and guarantee the rehabilitation of this member, stresses ultimately need to be decreased. These concerns were communicated verbally with DelDOT in December 2014.

4.3 Laboratory Testing

Four fatigue tests were conducted according to ASTM E647, each with a different specimen configuration: #1) Baseline specimen (bare steel plate); #2) Specimen with crack stop-hole; #3) Specimen with integrated strengthening and sensing (ISS) composites; #4) Specimen with both ISS composite and crack-stop hole. The specimen dimensions and configurations are presented in Section 3.3. All specimens were fabricated from Grade 36 steel comprising material of older bridges susceptible to reaching their fatigue life-span.

The first step to prepare the specimens was to introduce initial fatigue damage. In this research, a 10.5 mm (0.413 in) crack, measured from the notch tip, was considered representative of typical fatigue damage found in a bridge member. During pre-cracking, which is required per ASTM E647, a loading level was carefully selected to ensure that crack growth rate was less than 10^{-8} m/cycle (3.94^{-7} in/cycle) until the crack length was 1.0 mm (0.04 in). Four ASTM E647 specimens were prepared with the initial damage (later referred to as initial crack). A constant sinusoidal cyclic loading with load amplitudes between 89.4 and 125 kN (20 and 28 kip) was selected. It took approximately 72,000 loading cycles to generate the 10.5 mm (0.41 in) long crack. A hand-held microscope was used to measure the crack length during loading. Additionally, crack lengths were measured utilizing dye penetration inspection (DPI) at the end of the initial loading cycles to ensure that each specimen had equal initial damage.

4.3.1 Specimen #1: Baseline

The initial specimen tested was a standard, unaltered ASTM E647 compact steel specimen as presented in Section 3.3.1. Ultimately it was discovered that utilizing the previously discussed fatigue loading, the steel specimen employed in baseline testing took a total of about 176,000 cycles before failure occurred. An image taken of the specimen after failure is shown in **Figure 57**. As this was our baseline specimen, this value serves as a point of reference for the other fatigue tests. The propagation of the crack relative to the number of cycles is presented and compared with the other specimens in **Figure 74**.

Figure 57. Specimen #1 after 176,000 load cycles (failure).

As stated in Section 3.3, for each test, loading was halted after approximately every 20,000 cycles in order to measure the crack length. **Figure 58** and **Figure 59** show photos taken during one of these periods, more specifically after the specimen had completed 130,000 cycles. From these images, particularly **Figure 59**, it can be seen that the crack does not actually grow completely straight.

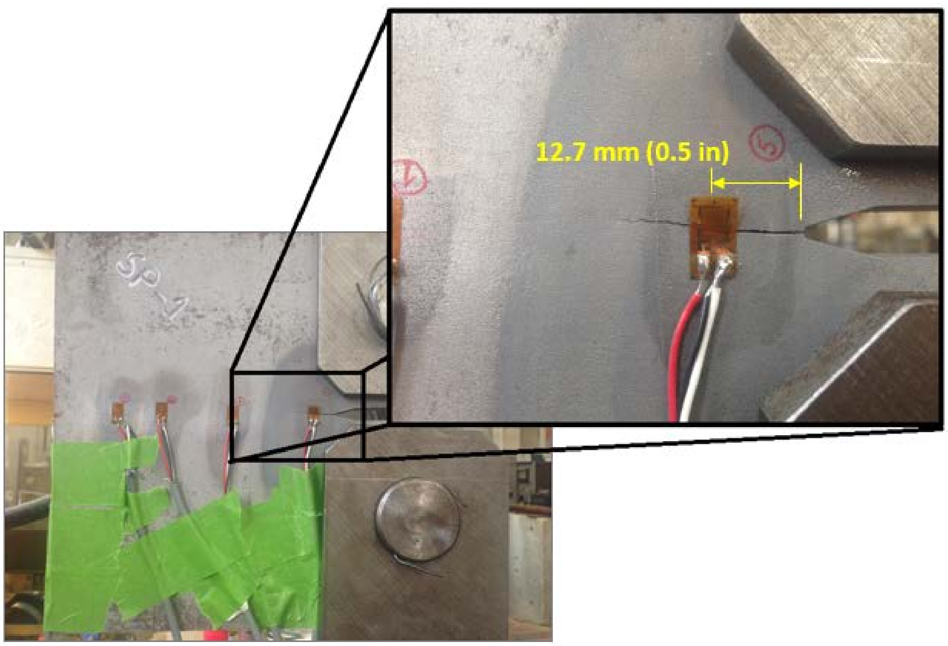

Figure 58. Specimen 1 after 130,000 Cycles (view of front side, instrumented).

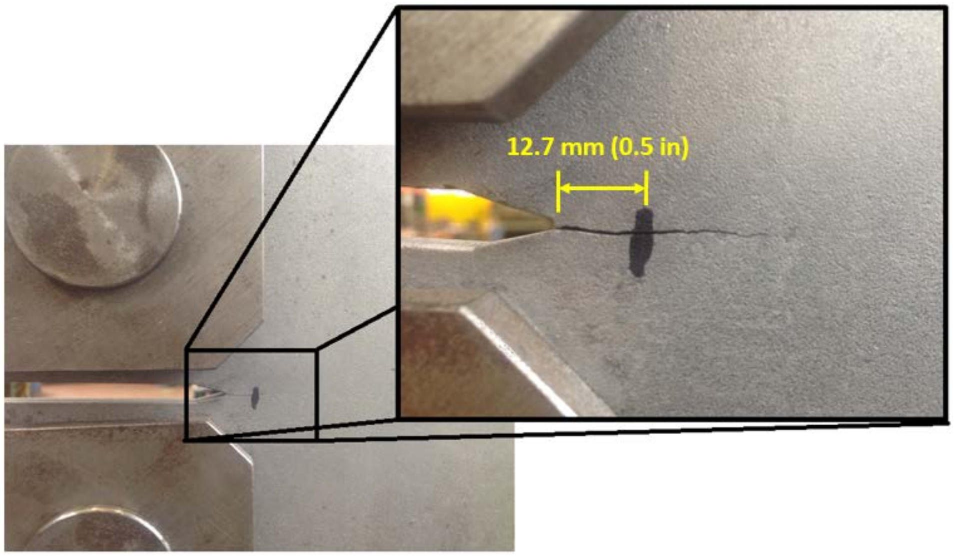

Figure 59. Specimen 1 after 130,000 Cycles (view of back side).

Figure 60 illustrates sample strain profiles taken during loading of Specimen #1. These plots show the relationship between strain along the projected crack path. Strain gauges No. 1 to 5 placed on the front face were plotted to order to generate the strain profiles; the back-face gauge (No. 4) was not included. Theoretically, by mechanical principles considering the stress concentration at the crack tip, as the distance from the crack mouth increases, the strain should exponentially decrease as it approaches the neutral axis, then linearly reduce after that point. These plots generally follow that trend.

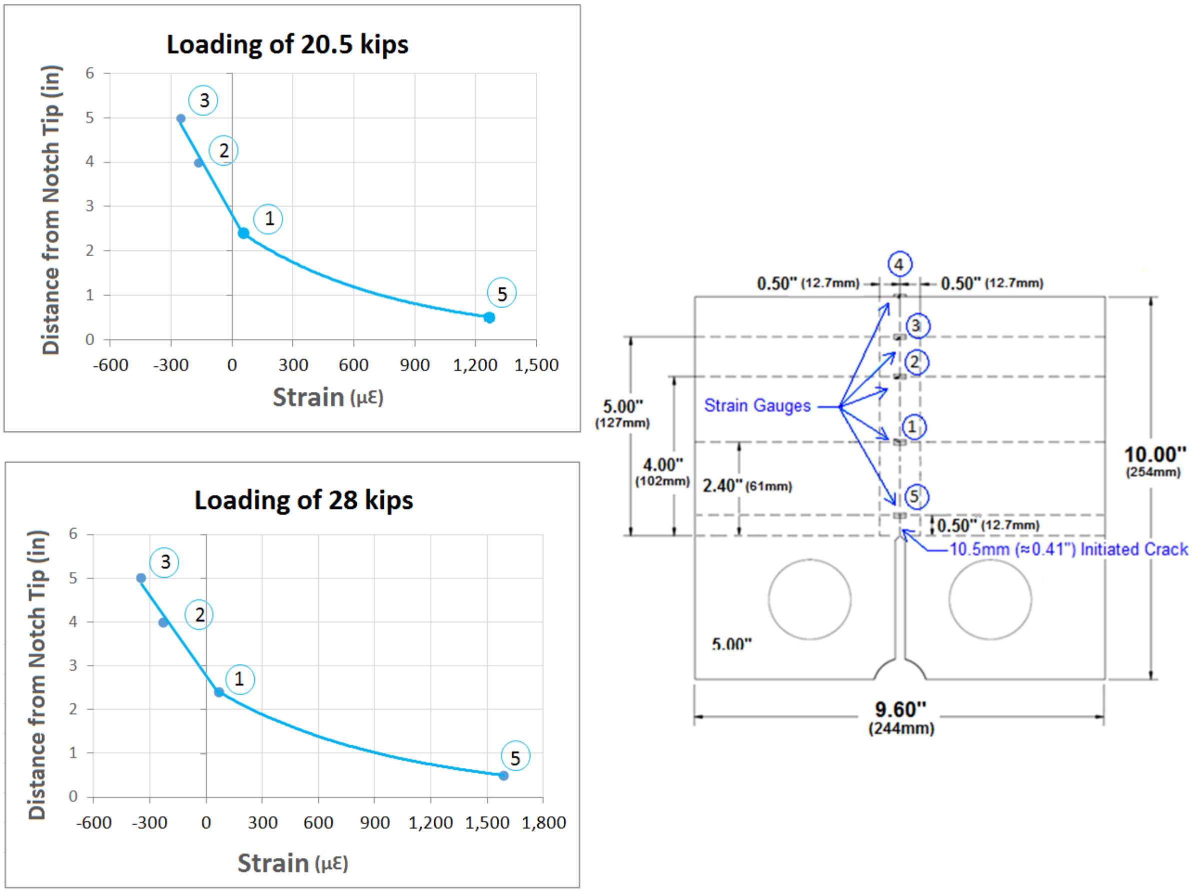

Figure 60. Sample of the instantaneous strain profile along the projected crack path at approximately 40,000 cycles.

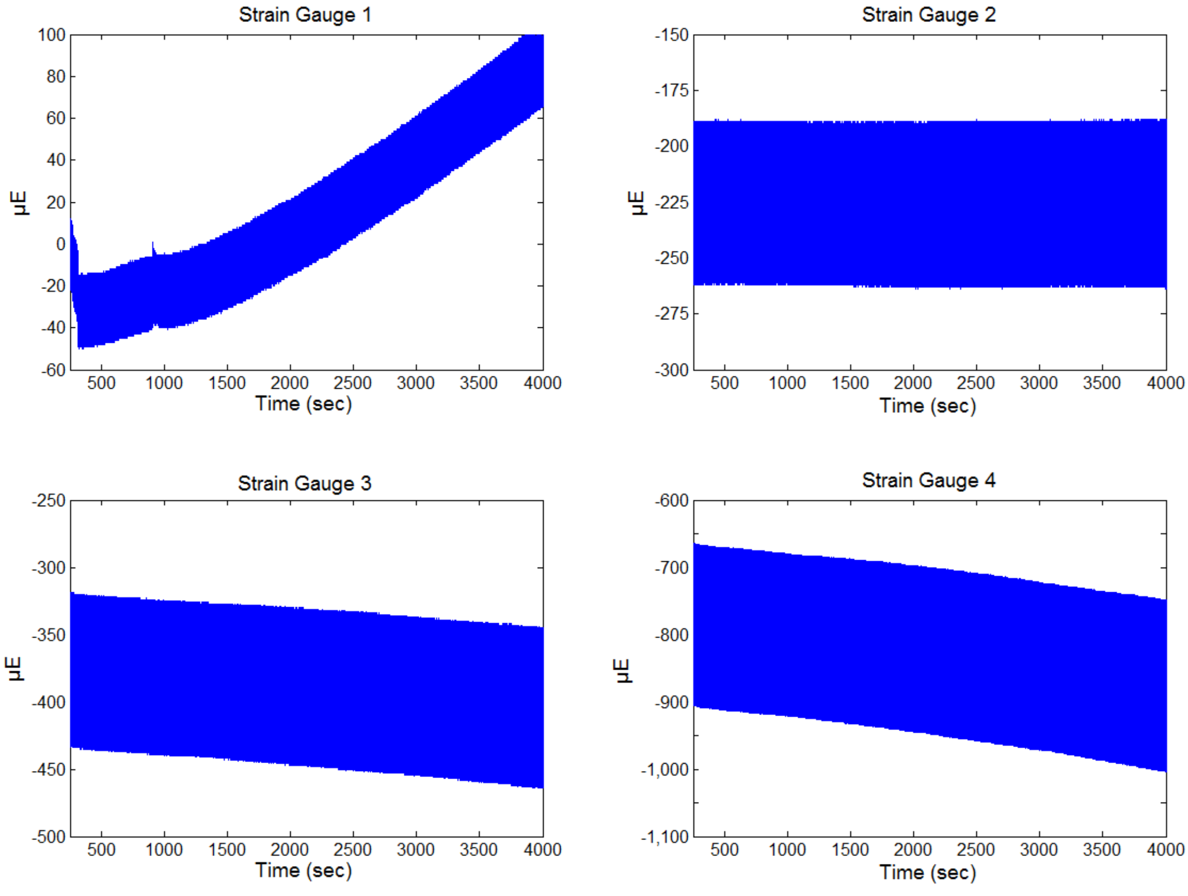

Figure 61. Sample strain readings for 10,000 cycles.

The overall trend of the strain data is shown in **Figure 61**. This plot depicts a sample of about 10,000 cycles but gives a good overall representation of the dataset. It should be noted that the readings for strain Gauge #5 are not depicted in any plots as this gauge was located 12.7 mm (0.5 in) from the notch tip. Consequently, shortly after crack initiation of 10.5 mm (0.41 in), and the commencement the fatigue loading, the crack propagated though this gauge and debonded it. Therefore, only a minimal number of strain readings were able to be captured after pre-cracking of the specimen. It can be observed that the neutral axis is close to Gauge #1 and that the compressive (Gauges # 2 to #4) and tension (Gauge #1) strains increase, which is expected. Although not shown in **Figure 61**, Gauge #5 followed a similar pattern. Strain readings exponentially increased until they reached a point in which they exceeded the gauge's range. Recalling from Section 3, it should be noted that Gauge #4 is the back-face strain gauge and therefore doesn't significantly correlate with any of the other gauges and is not a part of the strain profile.

Figure 62 presents the same data as the **Figure 61** on a different time scale. This plot displays a few seconds of data, thus the actual strain readings that are experienced for an individual cycle can be seen. As displayed, all gauge readings consistently follow a sinusoidal pattern which is consistent with the pre-set fatigue loading configuration. For this incremental portion in time, Gauge #1 is experiencing strains ranging between about -15 and 20 με; Gauge #2 between about -260 and -190 με; Gauge #3 between about -445 and -330 με; Gauge #4 between about -950 and -700 με. Gauge #5 is once again not depicted as values near the crack tip exceeded the limits the strain gauge could physically handle.

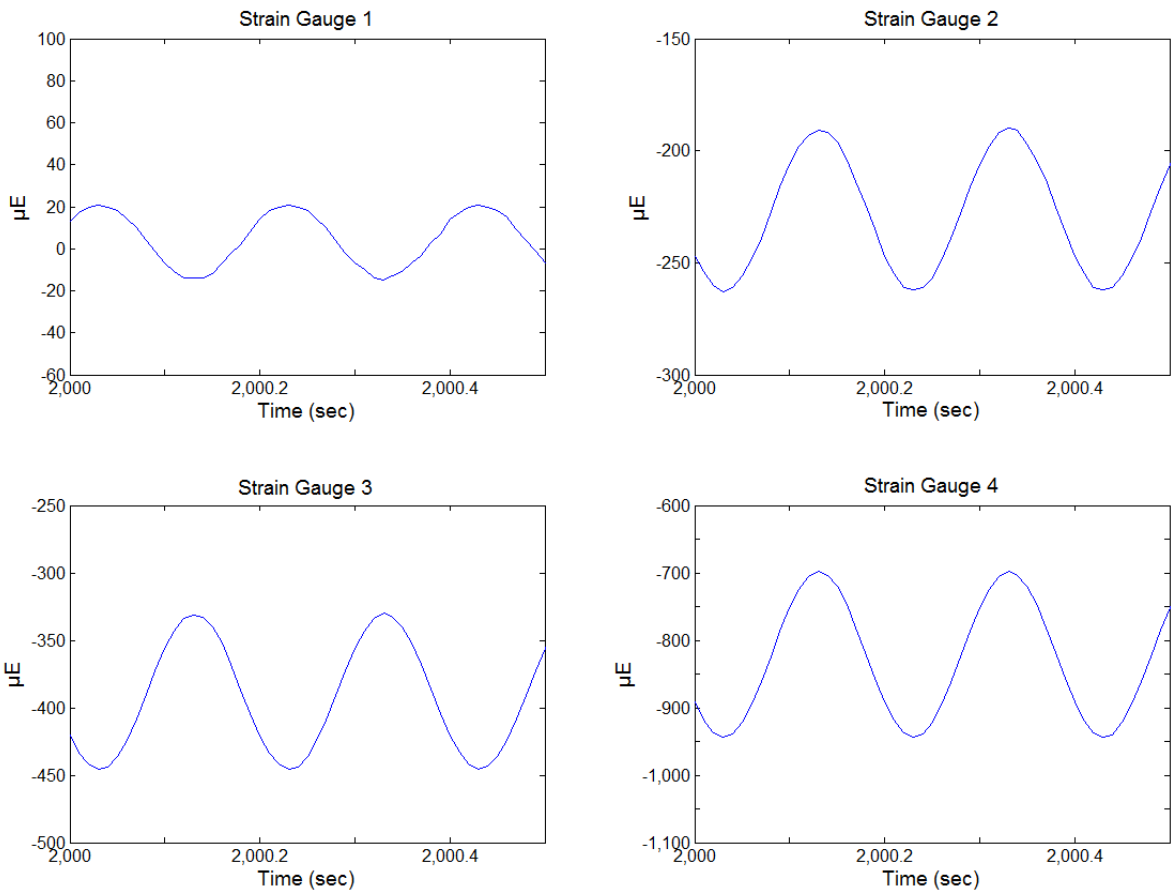

Figure 62. Sample strain reading for sample individual cycles.

4.3.2 Specimen #2: Crack-Stop Hole

Specimen #2 was a steel plate that utilized the crack-stop hole drilling rehabilitation method once the fatigue crack had been initialized as described in Section 3.3.2. This specimen failed by fracture after experiencing a total of approximately 195,000 fatigue cycles. The failed specimen is shown in **Figure 63**. It is apparent that this value exceeds that of Specimen #1, which ultimately failed after a total of 176,000 cycles. Subtracting out the cycles to initiate crack and pre-crack length, this specimen was subject to about 101,000 fatigue cycles before failure occurred. Correspondingly, Specimen #2 experienced 121,000 fatigue cycles prior it failing, which represents a 20% increase in the observed fatigue life. The propagation of the crack relative to the number of cycles is presented and compared with the other specimens in **Figure 74**.

Figure 63. Specimen #2 after 195,000 cycles (failure).

Figure 64 illustrates strain profiles at 125,000k cycles taken at the load amplitudes of 20 and 28 kip (88.9 and 125 kN). From examination of these figures it can be established that the neutral axis has shifted away from the crack initiation point when compared to Specimen #1, as a result of drilling a crack-stop hole, which was to be expected. The added hole is essentially equivalent to shifting the neutral axis by approximately 25.4 mm (1 in). In addition, it appears that each strain profile follows a seemingly exponentially decreasing manner as distance from the crack tip is increased.

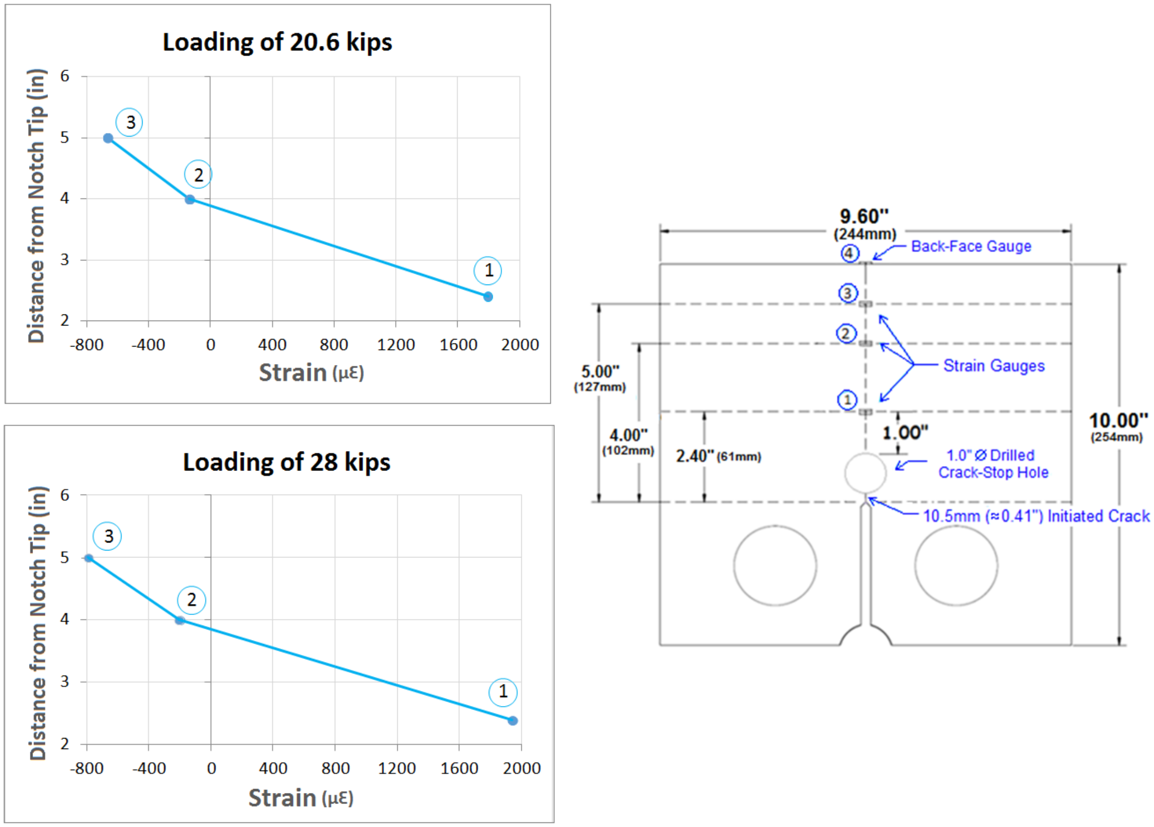

Figure 64. Sample instantaneous strain profile along projected crack path after 125,000 cycles.

Similar to Specimen #1, it can be observed from **Figure 65**, which was taken after about 160,000 fatigue cycles, that the crack has reinitiated despite the crack-stop hole. It can also be noticed that the crack has reinitiated slightly above the center of the hole.

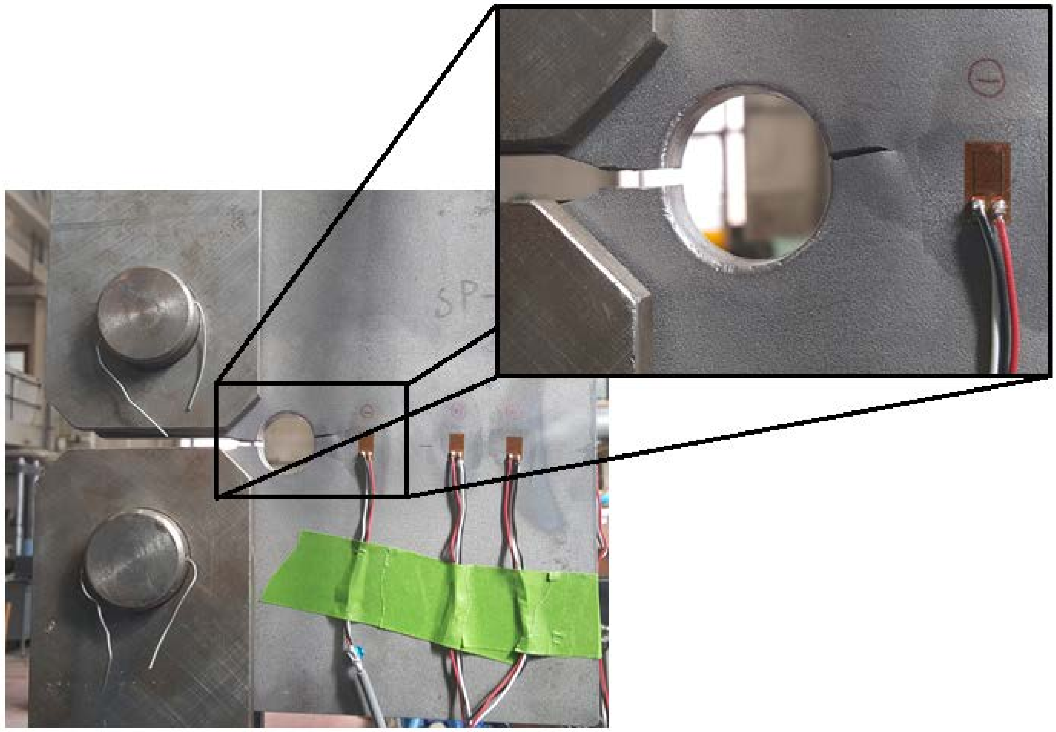

Figure 65. Specimen #2 after about 160,000 cycles (front side, instrumented).

4.3.3 Specimen #3: Integrated Strengthening and Sensing (ISS) Composite

Specimen #3 was rehabilitated using the proposed ISS composite as presented in Section 3.3.3. Our research aims at addressing the current issue of effectively rehabilitating fatigue cracks found on steel structures through means of this proposed holistic approach. As in the case with all previous experiments, Specimen #3 was cyclically loaded at 2.5 Hz with an applied load fluctuating between 88.9 and 125 kN (20 and 28 kips). Specimen #3 finally failed after a total of approximately 315,000 cycles. The failed specimen is shown in **Figure 66**.

Figure 66 illustrates that the composite patch itself did not fail, but rather debonding occurred between the steel and composite. After debonding, the load cannot effectively be transferred from the steel to the patch anymore. The full load is then placed back onto the further damaged specimen causing crack propagation to rapidly reinitiate towards failure. This emphasizes the importance of the bond for effective rehabilitation of fatigue cracks. The propagation of the crack relative to the number of cycles is presented and compared with the other specimens in **Figure 74**.

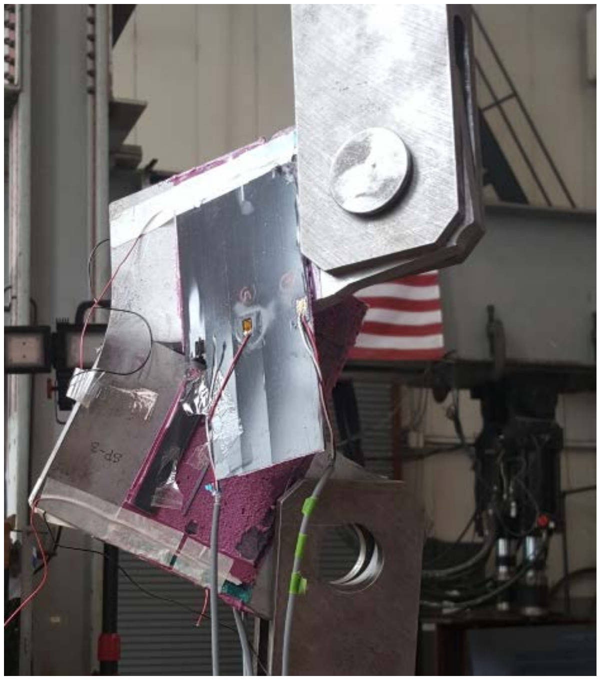

Figure 66. Specimen #3 after 315,000 cycles (failure).

Figure 67 as well as **Figure 68** depict data recorded as a result of the incorporated carbon nanotube (CNT) infused sensing layer. These graphs demonstrate the real-time monitoring capability the CNT sensing layer possesses. The utilization of this layer allowed for the continual monitoring and ability to track the propagating crack although the crack was actually now covered by the ISS composite. These results of crack length determined from the CNT sensing layer remain consistent with simple crack length measurements taken throughout the experiment. This ability of the layer addresses many concerns individuals may have in regards to the ability to continue to monitor a fatigue crack once it is covered by a layer.

Figure 67 shows the measured resistance in the CNT sensor correlated with the number of applied fatigue cycles. The measured actual crack length is shown for comparison. It can be seen that the resistance and crack growth correlate reasonably well. After about 260,000 cycles, the resistance increases at a higher rate, which was found to be associated with the onset of debonding. The deviation of the resistance measurements from crack length before 200,000 cycles needs to be addressed in further research.

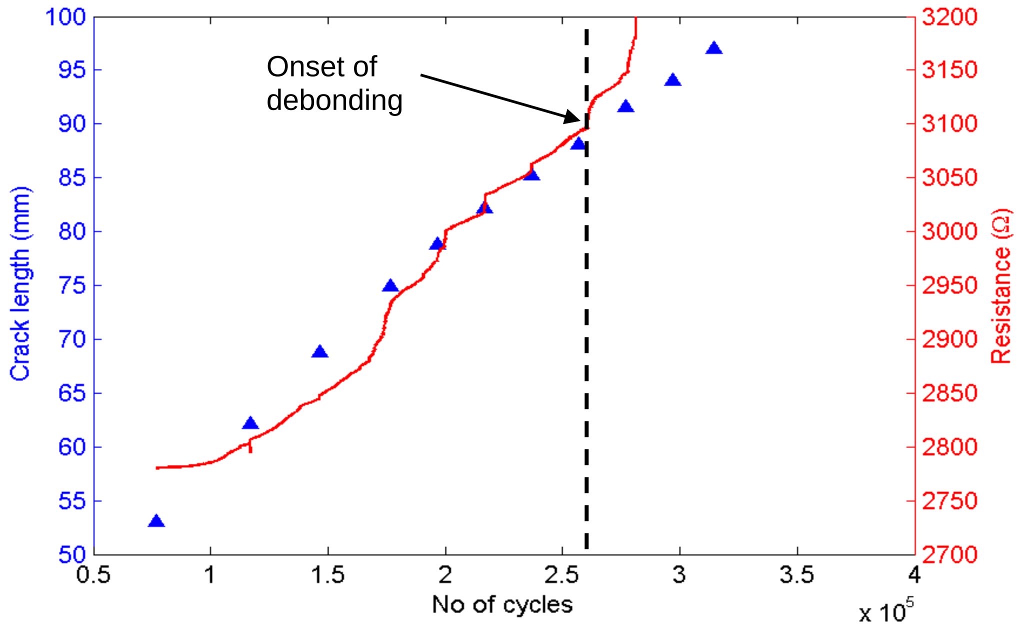

Figure 67. Crack lengths vs. resistance comparison.

Figure 68 demonstrates the monitoring capabilities of the ISS composite; if desired the CNT sensing layer can also be used for real-time monitoring of individual load cycles. In this case, the sampling rate was fairly low, which can easily be changed to produce better temporal resolution.

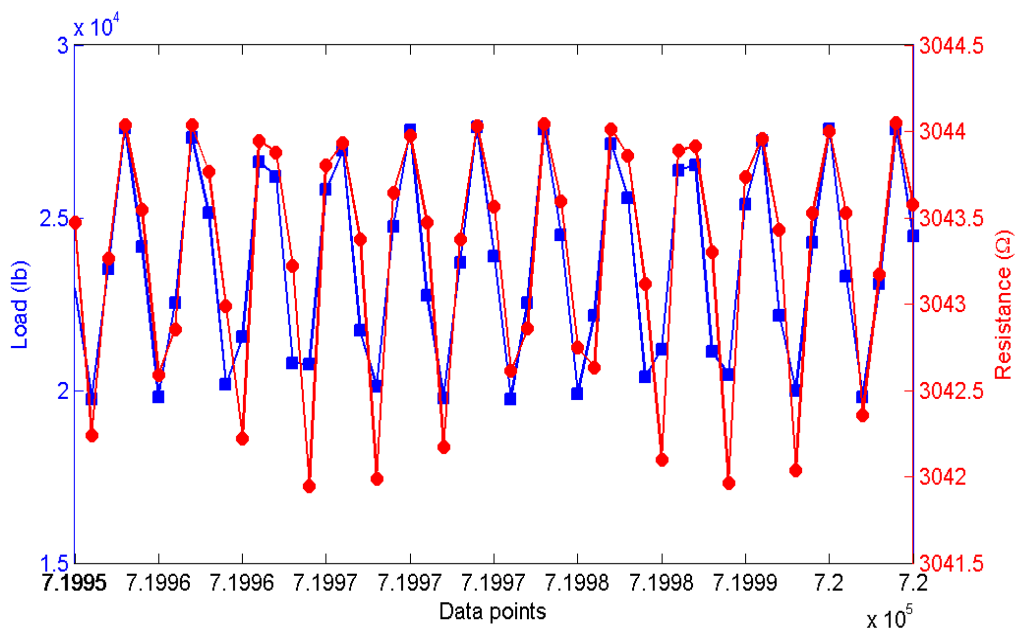

Figure 68. Real-time monitoring utilizing CNT sensing layer.

4.3.4 Specimen #4: Crack-Stop Hole and ISS Composite

Figure 69 shows an image of the final rehabilitation scheme combining crack-stop hole drilling and our proposed ISS composite. Using the same applied load fluctuating between 88.9 and 125 kN (20 and 28 kips), Specimen #4 failed after a total of approximately 728,000 cycles. The propagation of the crack relative to the number of cycles is presented and compared with the other specimens in **Figure 74**.

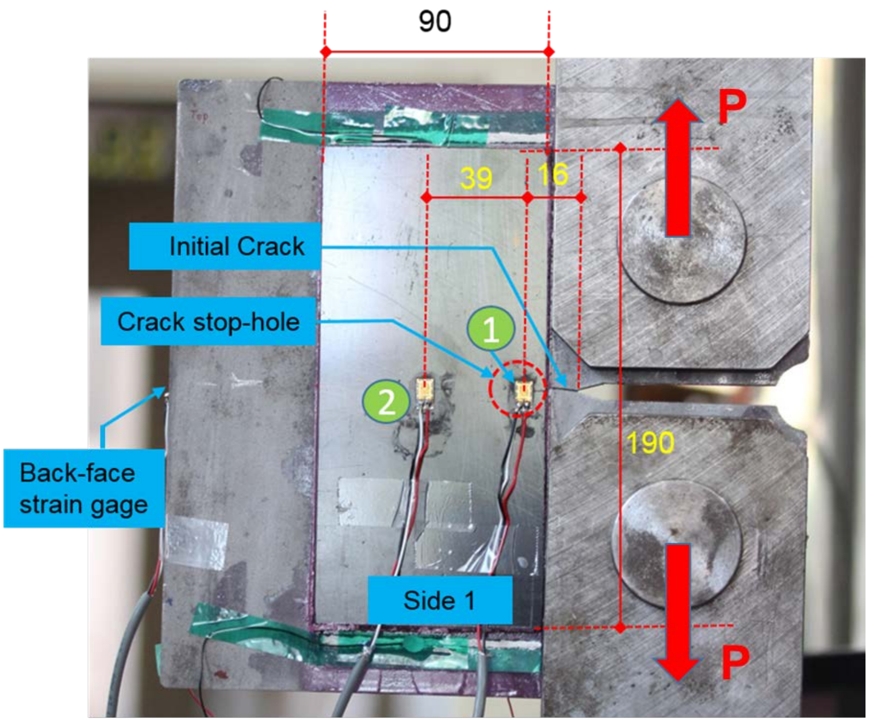

Figure 69. Loading configuration and gauge locations for Specimen #4.

Figure 70 shows beach marks on the fracture surface of Specimen #4. The beach marks show a curved morphology. These beach marks were tracked in order to relate fracture crack length with the number fatigue cycles. **Figure 70** shows that the ISS repair allowed for longer fatigue crack and the relationship between crack length and corresponding cycles was found to be fairly linear (**Figure 71**); such linear relationship confirms the ability of ISS composites to confine and control crack growth until fracture occurs. From the responses of the strain gages as shown in **Figure 71**, a premature debonding initiated at one side of specimen. Thus the crack initiated from the debonded side (from the corner of crack-stop hole) and propagated faster on that side of the specimen because of non-symmetric load sharing.

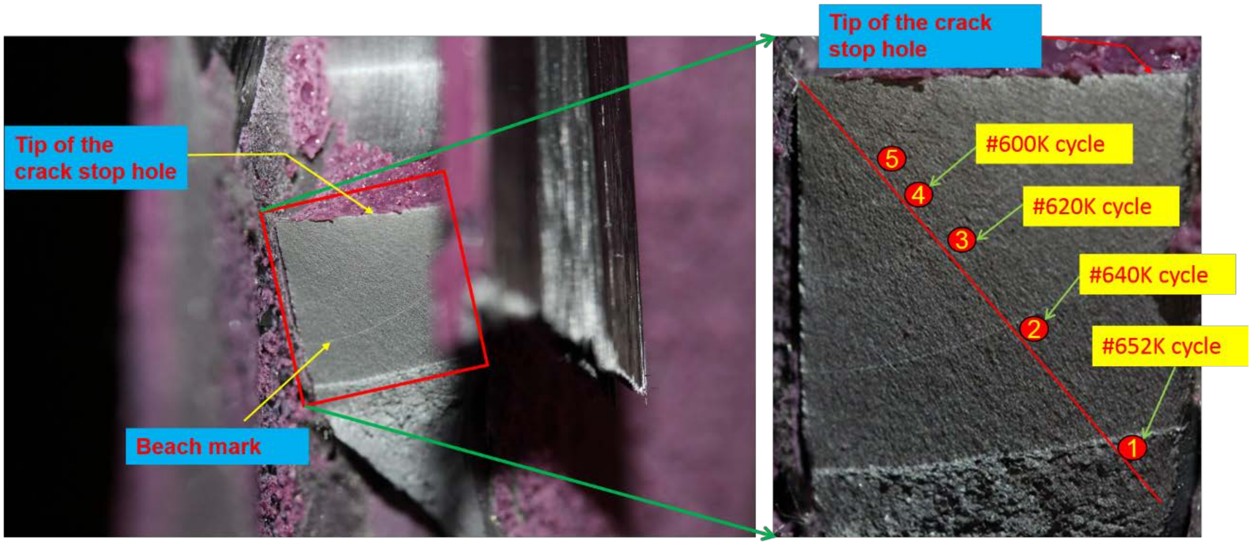

Figure 70. Curved beach marks resulting from of structural composite debonding on one side.

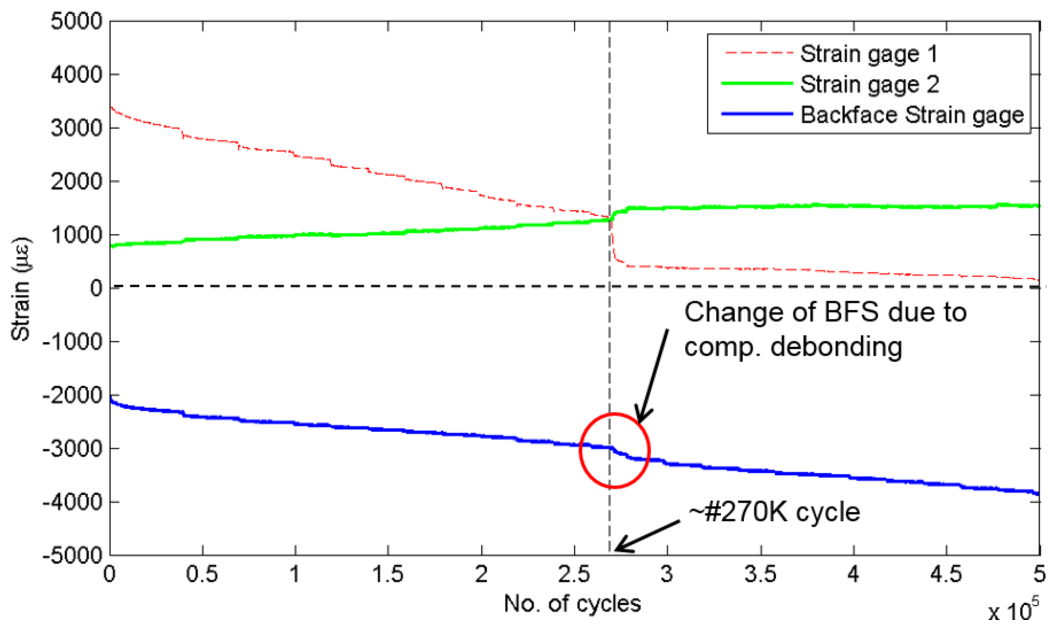

Figure 71. Strain-fatigue cycle response showing the detection of composite debonding.

Figure 72 shows the resistance response of the CNT-based sensor and the back-face strain (BFS) vs. applied load cycles. Reasonable correlation exists between the strain and resistance data, demonstrating the ability of the sensing layer to monitor fatigue crack propagation. The deviation observed in the BFS data at 270,000 cycles is due to the onset of local debonding as also shown in **Figure 71**.

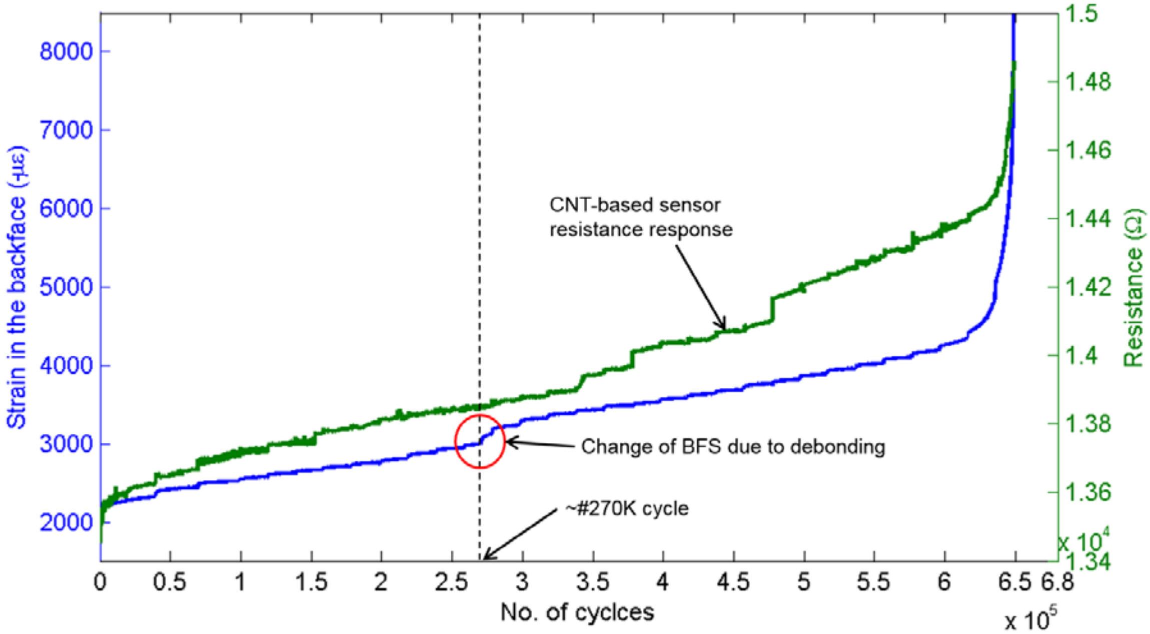

Figure 72. Resistance and back-face strain with increasing fatigue cycles for specimen with both crack stop-hole and ISS composites.

4.3.5 Comparison of Test Results

The pauses of cyclic loading generated marks, namely beach marks, on the fracture surface due to oxidation of the free surface. **Figure 73** shows the fracture surfaces of baseline specimen, specimen with crack stop-hole and specimen with ISS composites.

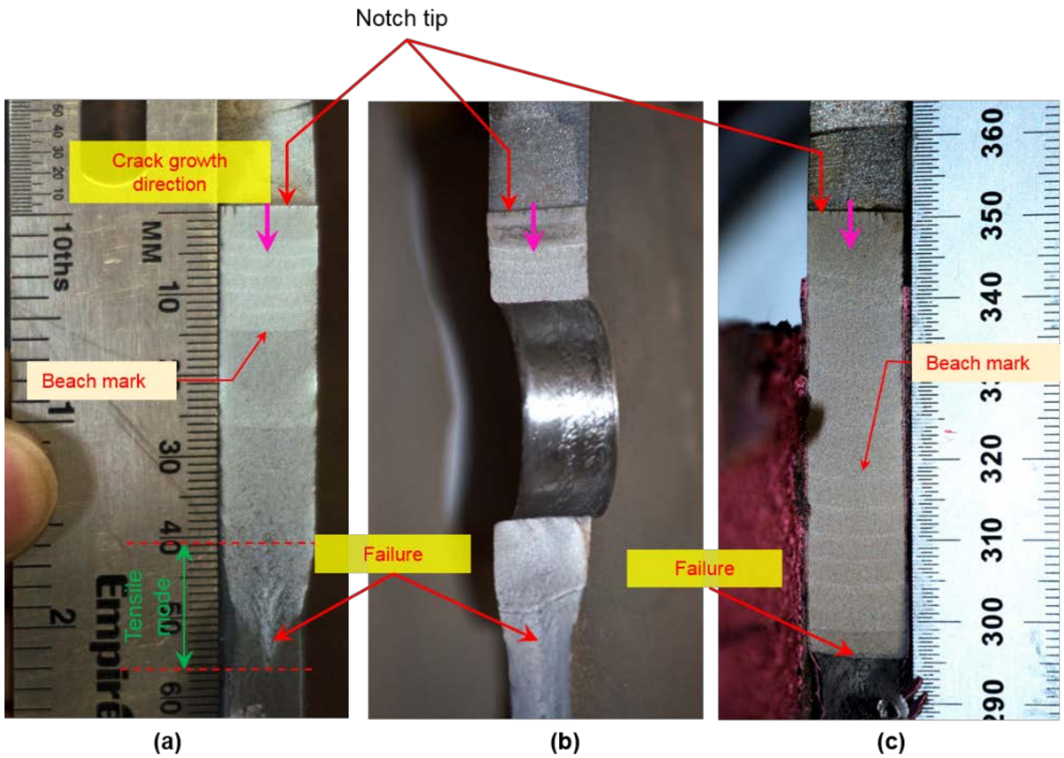

Figure 73. Fracture surface of (a) baseline, (b) crack-stop hole repair, and (c) ISS repair specimens fatigue failures.

Experimental results with respect to crack growth vs. fatigue cycle for all specimens tested are presented in **Figure 74**. It can be observed that while drilling a crack-stop hole, as was done for Specimen #2, brings some extension of fatigue life. However, the crack was not prevented from reinitiating after the hole had been drilled, leading to modest fatigue life increase of 20% (from 101k to 121k cycles). The critical crack length at fracture was found to be *a* = 87.5 mm (3.45 in) for both specimens. It can be concluded that adding a crack-stop hole does not increase the critical crack length. Application of our proposed ISS rehabilitation scheme to Specimen #3 resulted in a fatigue life extension of 135% compared to Specimen #1. It is further apparent from the graph that crack growth has been impeded as a result of the added composite layer. The crack length at fracture was *a* = 97 mm (3.82 in), which was significantly longer than critical crack length. Finally, failure for Specimen #4, which was rehabilitated using our proposed ISS layer combined with drilling a crack-stop hole, occurred at a remarkable number of 652k fatigue cycles, which represents an increase of 550% compared to Specimen #1. The average length of the crack at failure was *a* = 90 mm (3.54 in). **Figure 75** shows a comparison of final results using a bar chart.

It can be concluded that application of our proposed rehabilitation scheme based on the ISS composite combined with a crack-stop hole (Specimen #4) provided a significant increase of the fatigue life for a laboratory steel specimen tested according to ASTM E647.

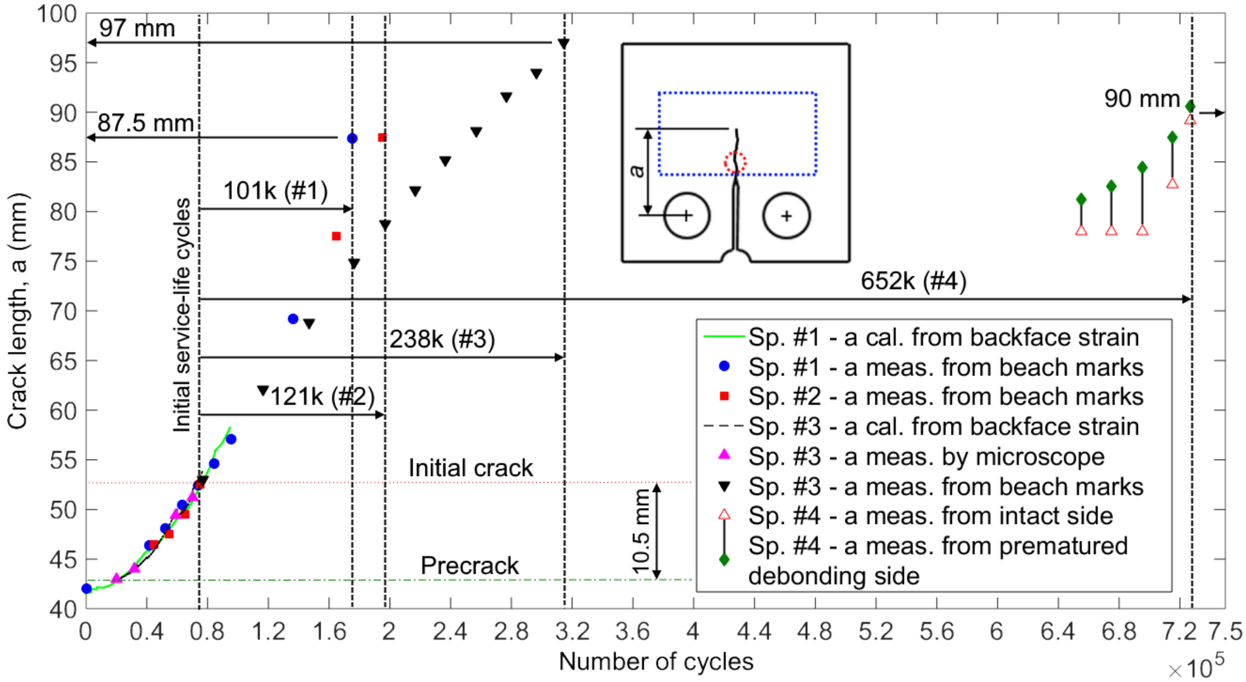

Figure 74. Number of cycles vs. crack length for baseline (blue dots), crack-stop hole (red squares), and proposed solution (black triangles). Note that '*a*' is measured from the load application point (per ASTM E647) and not actual crack length.

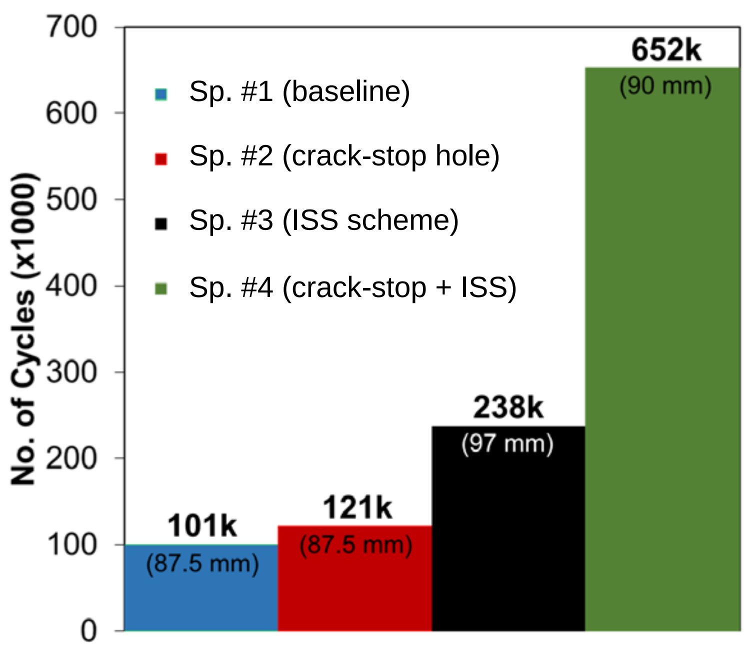

Figure 75. Comparison of the remaining fatigue life of different specimens after initial cracking. (Numerical values in parentheses represent crack length, *a* at the time of fracture.)

5 Summary and Conclusions

This research project investigated an issue currently found in a number of DelDOT steel bridges: fatigue cracks. Quite often when a fatigue crack is discovered, the immediate response is to drill a crack-stop hole. As discussed in results in Section 4.3.2, a drilled hole does in fact contribute to the prolonging of fatigue life, but may not prevent fatigue cracks from reinitiating after some period of time. However, as part of this research we proposed to study a new integrated strengthening and sensing (ISS) approach based on carbon nanotube (CNT) composites that are able to (1) extend the remaining fatigue life and (2) provide a sensing solution to monitor crack propagation. The experimental tests followed ASEM E647 specifications using cyclic loading fluctuating between 88.9 and 125 kN (20 and 28 kips). Based on the laboratory study, we can conclude the following:

- In our laboratory experiments, a 20% increase in the total number of fatigue cycles applied to an ASTM E647 specimen (Specimen #2) before fracture occurred was demonstrated employing a crack-stop hole. It should be noted that the crack did reinitiate and there was no improvement of the critical crack length (a = 87.5 mm (3.45 in)) compared to the baseline specimen (Specimen #1).
- By employing our ISS methodology (Specimen #3), the remaining fatigue life was increased by 135% compared to Specimen #1. Strain measurements showed a drastic decrease in the stresses experienced in the steel specimen, which is attributed to the added composite layer. The chosen composite material, M40J, possesses a modulus of elasticity of 230 GPa, according to the manufacturer, making it a high strength and relatively high modulus material. The particular sample employed for research was found to have a modulus of closer to 203 GPa by means of ASTM D-3039, which is close to that of A36 steel (200 GPa). This allowed for adequate load transfer from the steel to the ISS composite, thus restraining crack motion.
- Specimen #4 had both a crack-stop hole as well as the ISS composite. For this combined rehabilitation scheme, the fatigue life was extended by 550%, marking a significant improvement.
- For both Specimen #3 and #4, the sensing capabilities of the integrated CNT sensing layer allows for monitoring the crack growth both long-term and in real-time. The data further indicates that debonding may be indicated by a sudden increase in the resistance measurement in the CNT sensing layer.

Further research should address the following:

- Different geometric configurations of the ISS layer. For example, the agency may be more comfortable to place the sensor across the crack without covering the crack tip.
- Evaluation of the ISS methodology under more complex stress conditions as they may be experienced in differing realistic conditions.
- In-depth characterization of the sensing capabilities to capture onset and propagation of debonding.
- Other composite materials with higher stiffness that will allow more effective load sharing.
- Application and performance of the ISS composite on real bridges the field.

6 References

1. AASHTO, (2010) AASHTO LRFD Bridge Design Specifications, 5th Edition, American Association Highway Transportation Officials, Washington D.C.
2. Aggelopoulos, E. S., Righiniotis, T. D., & Chryssanthopoulos, M. K. (2011). Debonding of adhesively bonded composite patch repairs of cracked steel members. Composites Part B: Engineering, 42(5), 1262-1270.
3. ASTM Standard (1990). Standard Practices for Cycle Counting in Fatigue Analysis. E1049-85, American society for testing and materials. West Conshohocken, PA
4. ASTM Standard (2011). Standard Test Method for Measurement of Fatigue Crack Growth Rates. E647-08, American society for testing and materials. West Conshohocken, PA
5. Ariduru, Seçil. (2004) Fatigue life calculation by rainflow cycle counting method. Middle East Technical University, Tese de Mestrado .
6. Badawy, A. A. (2012). Impact behavior of glass fibers reinforced composite laminates at different temperatures. Ain Shams Engineering Journal, 3(2), 105-111.
7. Branco, C. M., Infante, V., & Baptista, R. (2004). Fatigue Behavior of Welded Joints with Cracks, Repaired by Hammer Peening. Fatigue & Fracture of Engineering Materials & Structures, 27(9), 785-798.
8. Buyukozturk, O., Gunes, O., & Karaca, E. (2004). Progress on understanding debonding problems in reinforced concrete and steel members strengthened using FRP composites. Construction and Building Materials, 18(1), 9-19.
9. Colombi, P., Bassetti, A., & Nussbaumer, A. (2003). Crack growth induced delamination on steel members reinforced by prestressed composite patch. Fatigue & Fracture of Engineering Materials & Structures, 26(5), 429-438.
10. Crain, Josh S (2010). Fatigue Enhancement of Undersized, Drilled Crack-Stop Holes, M.S. thesis, University of Kansas, Lawrence, KS.
11. Dexter, R. and Ocel, J. (2013). Manual for repair and retrofit of fatigue cracks in steel bridges, FHWA-IF-13-020, March, Federal Highway Administration, Mclean, VA.
12. Downing, S.D., Socie, D.F. (1982). Simple rainflow counting algorithms. International Journal of Fatigue, Volume 4, Issue 1, January, 31-40.
13. Fisher, John W., Jin, Jain, Wagner, David C., and Yen, Ben T. (1990). Distortion-Induced Fatigue Cracking in Steel Bridges. National Cooperative Highway Research Program (NCHRP) Report 336, National Transportation Research Board, Washington, D. C.
14. Gao, L., Thostenson, E. T., Zhang, Z., & Chou, T. W. (2009). Sensing of Damage Mechanisms in Fiber-Reinforced Composites under Cyclic Loading using Carbon Nanotubes. Advanced Functional Materials, 19(1), 123-130.
15. Gao, L., Chou, T. W., Thostenson, E. T., Godara, A., Zhang, Z., & Mezzo, L. (2010). Highly conductive polymer composites based on controlled agglomeration of carbon nanotubes. Carbon, 48(9), 2649-2651.

16. Gunther, H. P., Kuhlmann, U., & Durr, A. (2005). Rehabilitation of Welded Joints by Ultrasonic Impact Treatment (UIT). In IABSE Symposium Report (Vol. 90, No. 4, pp. 71-77). International Association for Bridge and Structural Engineering.
17. Han, Z., & Fina, A. (2011). Thermal conductivity of carbon nanotubes and their polymer nanocomposites: a review. Progress in polymer science, 36(7), 914-944.
18. Ju, X., & Tateishi, K. (2012). Study on fatigue crack propagation of a through-thickness crack subjected to out-of-plane bending. International Journal of Steel Structures, 12(1), 85-92.
19. Karbhari, V. M., & Shulley, S. B. (1995). Use of composites for rehabilitation of steel structures-determination of bond durability. Journal of Materials in Civil Engineering, 7(4), 239-245.
20. Kumar, B. G., Singh, R. P., & Nakamura, T. (2002). Degradation of carbon fiber-reinforced epoxy composites by ultraviolet radiation and condensation. Journal of Composite Materials, 36(24), 2713-2733.
21. Lwin, M. (2012). Clarification of Requirements for Fracture Critical Members. Retrieved from http://www.fhwa.dot.gov/bridge/120620.pdf
22. Martins-Júnior, P. A., Alcântara, C. E., Resende, R. R., & Ferreira, A. J. (2013). Carbon Nanotubes Directions and Perspectives in Oral Regenerative Medicine. Journal of dental research
23. Matsuishi, M. & Endo, T. (1968) Fatigue of metals subjected to varying stress, Japan Soc. Mech. Engineering.
24. Mertz, D. R., and Gillespie, J. W., Jr. (1996). NCHRP-IDEA final report: Rehabilitation of steel bridge girders through the application of advanced composite materials (Contract No. NCHRP-93-ID011), Transportation Research Board, Washington, D.C.
25. Mertz, D. (2012). Steel Design Handbook: Design for Fatigue. No. FHWA-IF-12-052-Vol. 12
26. Miller, T. C., Chajes, M. J., Mertz, D. R., & Hastings, J. N. (2001). Strengthening of a Steel Bridge Girder Using CFRP Plates. Journal of Bridge Engineering, 6(6), 514-522.
27. Miner, M. A. (1945). Cumulative damage in fatigue. Journal of applied mechanics, 12(3), 159-164.
28. Newman, J. C., Yamada, Y., & James, M. A. (2011). Back-face strain compliance relation for compact specimens for wide range in crack lengths. Engineering Fracture Mechanics, *78*(15), 2707Fb-2711.
29. Palmgren, A. (1924). Die lebensdauer von kugellagern (Life Length of Roller Bearings. In German). Zeitschrift des Vereins Deutscher Ingenieure (VDI Zeitschrift), 68(14), 339-341.
30. Rainieri, C., Fabbrociono, G., Song, Y., & Shanov, V. (2011). CNT composites for SHM: a literature review. In International workshop: smart materials, structures & NDT in aerospace, 2-4.
31. Reid, L. (2014). Repairing and Preserving Bridge and Steel Structure Using an Innovative Crack Arrest Repair System. Advanced Materials Research, 891, 1217-1222.
32. Rolfe, S. T. and Barsom, John M. (1977). Fracture and Fatigue Control in Structures: Applications of Fracture Mechanics. First Edition. Prentice Hall.

33. Rutherford, S. E., and H. Polezhayeva. (2006). Effect of Burr Grinding on the Fatigue Strength of Angled Welded Connections. Lloyd's Register, London, England.
34. Salvetat, J. P., Briggs, G. A. D., Bonard, J. M., Bacsa, R. R., Kulik, A. J., Stöckli, T., *et al*. (1999). Elastic and shear moduli of single-walled carbon nanotube ropes. Physical Review Letters, 82(5), 944-7.
35. Sarangi, H., Murthy, K.S.R.K., & Chakraborty, D. (2010). Optimum Strain gage location for evaluating stress intensity factors in single and double ended cracked configurations. Engineering Fracture Mechanics, 77(16), 3190-3203.
36. Schumacher, T. and Thostenson, E. T. (2014). Development of structural carbon nanotube-based sensing composites for concrete structures. Journal of Intelligent Material Systems and Structures. Vol. 25(11), pp. 1331-1339.
37. Scott, D. W. (1979). On optimal and data-based histograms. Biometrika, 66(3), 605-610.
38. Shenton III, H. W., Chajes, M. J., & Holloway, E. S. (2000). A system for monitoring live load strain in bridges. In Structural Materials Technology IV Conference Proceedings, pp. 89-94.
39. Shield, C. K., Hajjar, J. F., & Nozaka, K. (2003). Repair of Fatigued Steel Bridge Girders with Carbon Fiber Strip. Minnesota Department of Transportation, St. Paul, MN.
40. Tang, B. (1997). Fiber Reinforced Polymer Composite Applications in USA: DOT-Federal Highway Administration. Proceedings of the First Korea/U.S.A. Road Workshop, January 28-29.
41. Thostenson, E. T., Ren, Z., & Chou, T. W. (2001). Advances in the science and technology of carbon nanotubes and their composites: a review. Composites science and technology, 61(13), 1899-1912.
42. Thostenson, E. T., & Chou, T. W. (2006). Carbon nanotube networks: sensing of distributed strain and damage for life prediction and self-healing. Advanced Materials, 18(21), 2837-2841.
43. Torayca M40J Data Sheet, Technical Data Sheet No. CFA-014, http://www.toraycfa.com/pdfs/M40JDataSheet.pdf
44. Torayca M60J Data Sheet, Technical Data Sheet No. CFA-018, http://www.toraycfa.com/pdfs/M60JDataSheet.pdf
45. Walters, D. A., Ericson, L. M., Casavant, M. J., Liu, J., Colbert, D. T., Smith, K. A., *et al*. (1999). Elastic strain of freely suspended single-wall carbon nanotube ropes. Applied Physics Letters, 74(25), 3803-3805.
46. Zhang, W., Picu, R. C., & Koratkar, N. (2007). Suppression of fatigue crack growth in carbon nanotube composites. Applied Physics Letters, 91(19), 193109.
47. Zweben, C. (1989). Introduction to Mechanical Behavior and Properties of Composites Materials. DCDE, Volume 1.

APPENDIX A

DelDOT BRIDGE INSTRUMENTATION

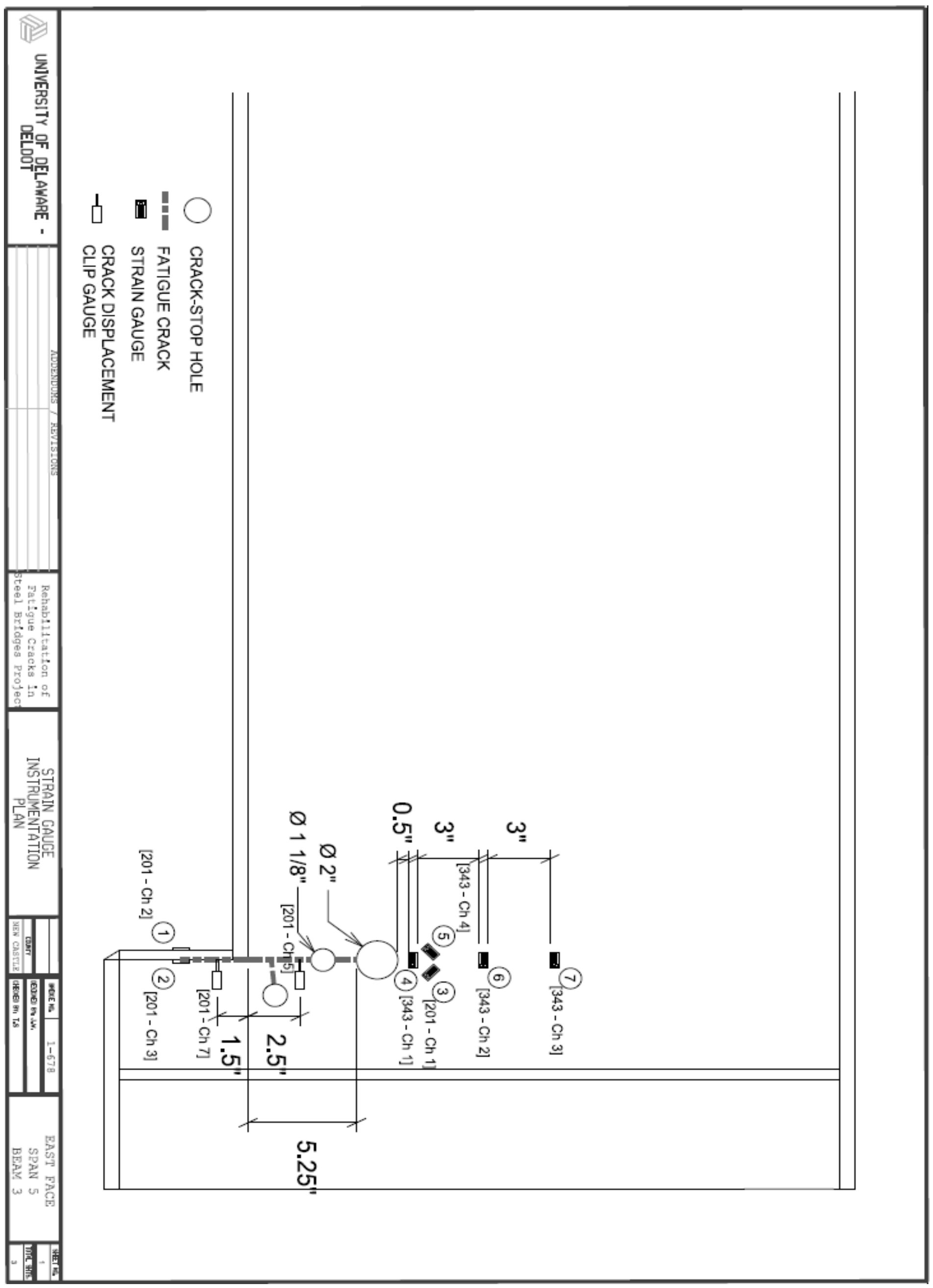

Figure A.1. Strain gauge instrumentation plan – East face of Beam 3 on Span 5.

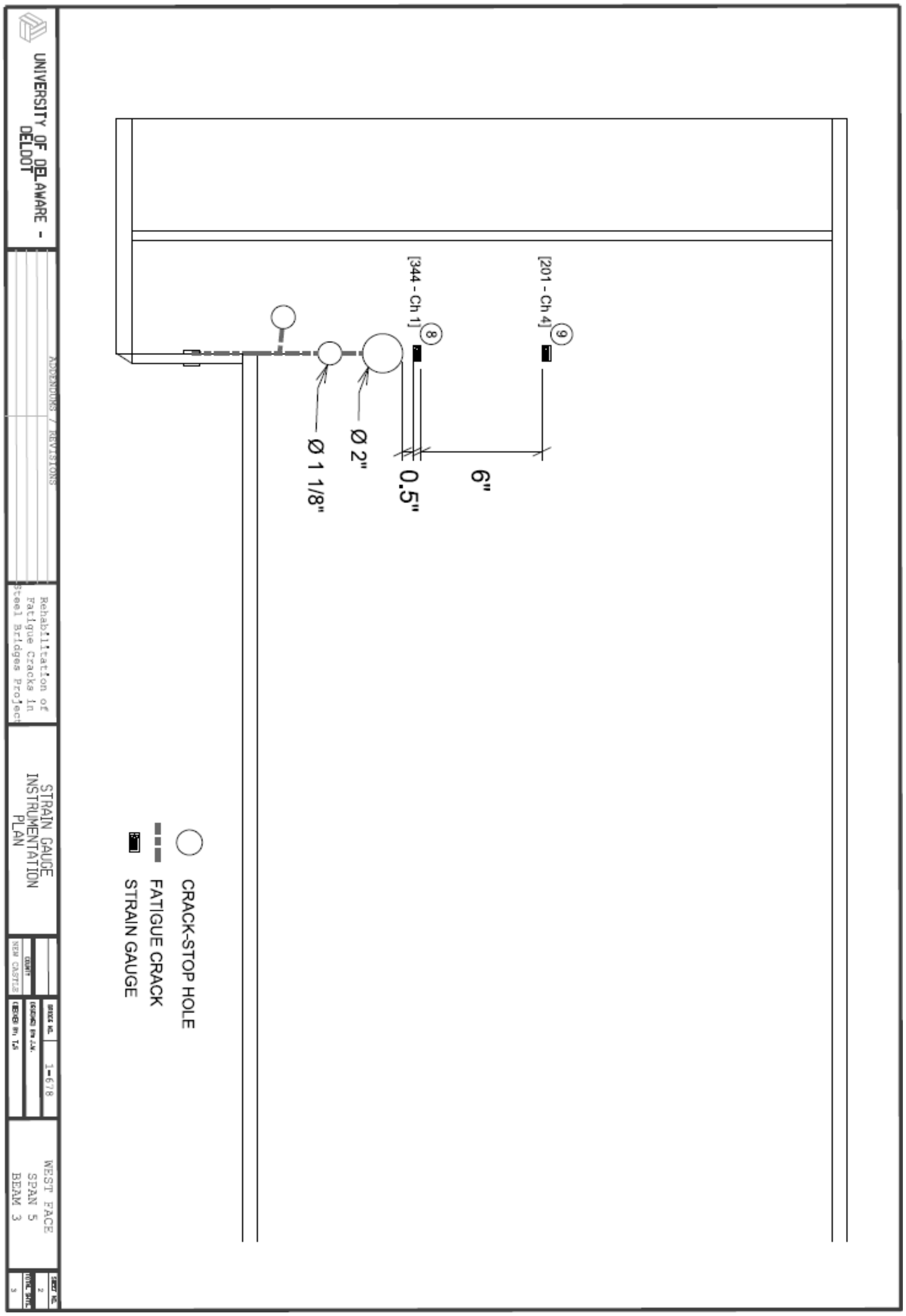

Figure A.2. Strain gauge instrumentation plan – West face of Beam 3 on Span 5.

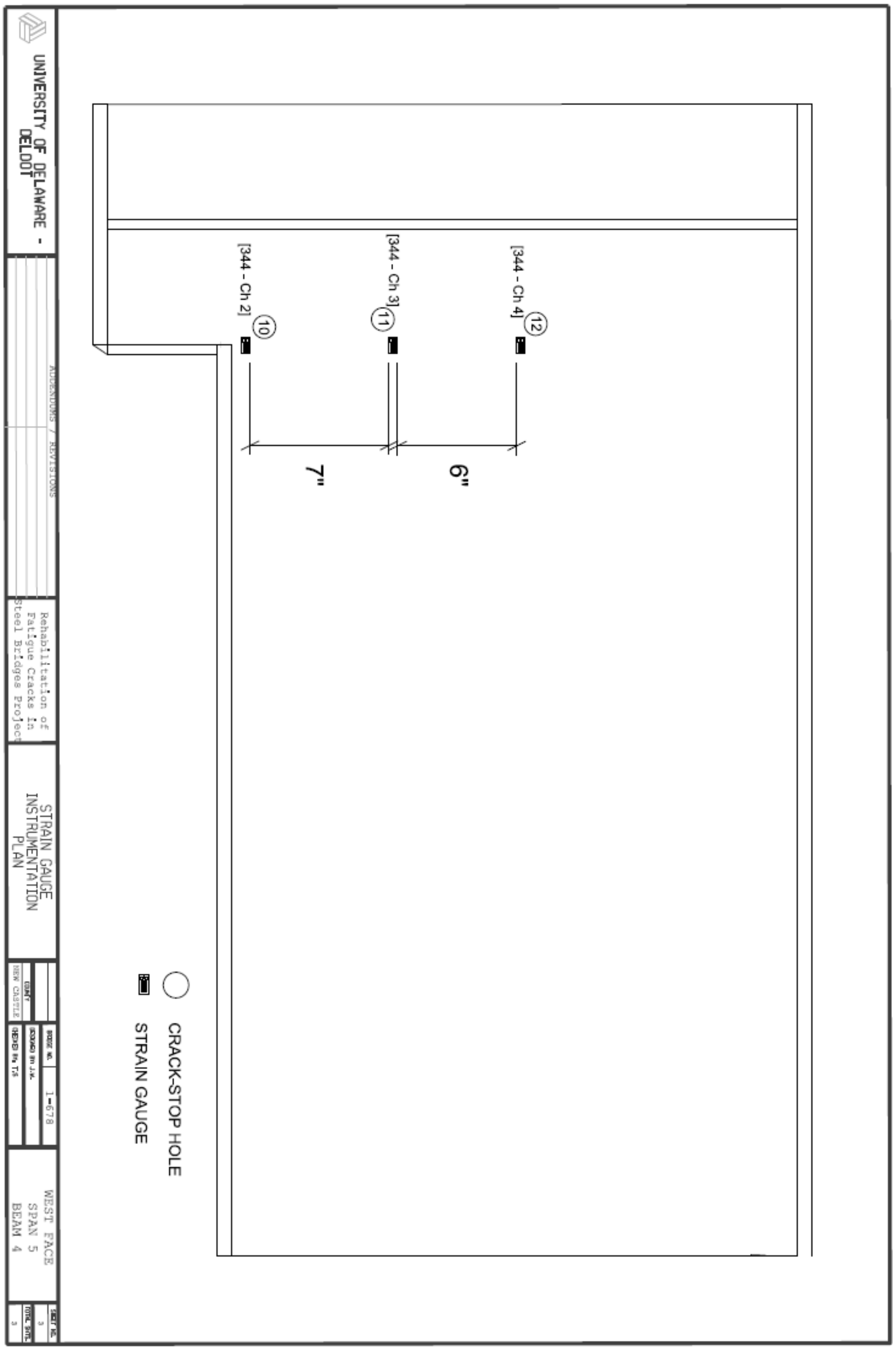

Figure A.3. Strain gauge instrumentation plan –West face of Beam 4 on Span 5.

Figure A.4. DelDOT Bridge 1678-006 fatigue cracks and drilled holes (before instrumentation).

Figure A.5. DelDOT Bridge 1678-006 fatigue cracks and drilled holes.

Figure A.6. Close-up of fatigue-prone detail (before instrumentation).

Figure A.7. East face – Span 5 – Beam 3 (before instrumentation).

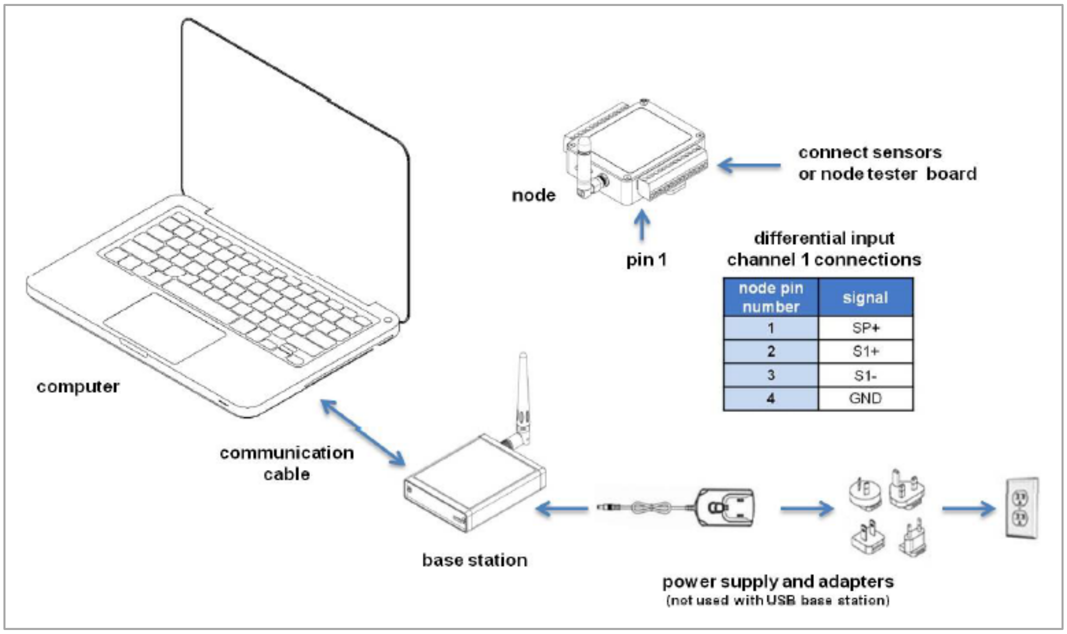

node pin number	signal
1	SP+
2	S1+
3	S1-
4	GND

Figure A.8. LORD MicroStrain® wireless sensing system (Source: www.microstrain.com)

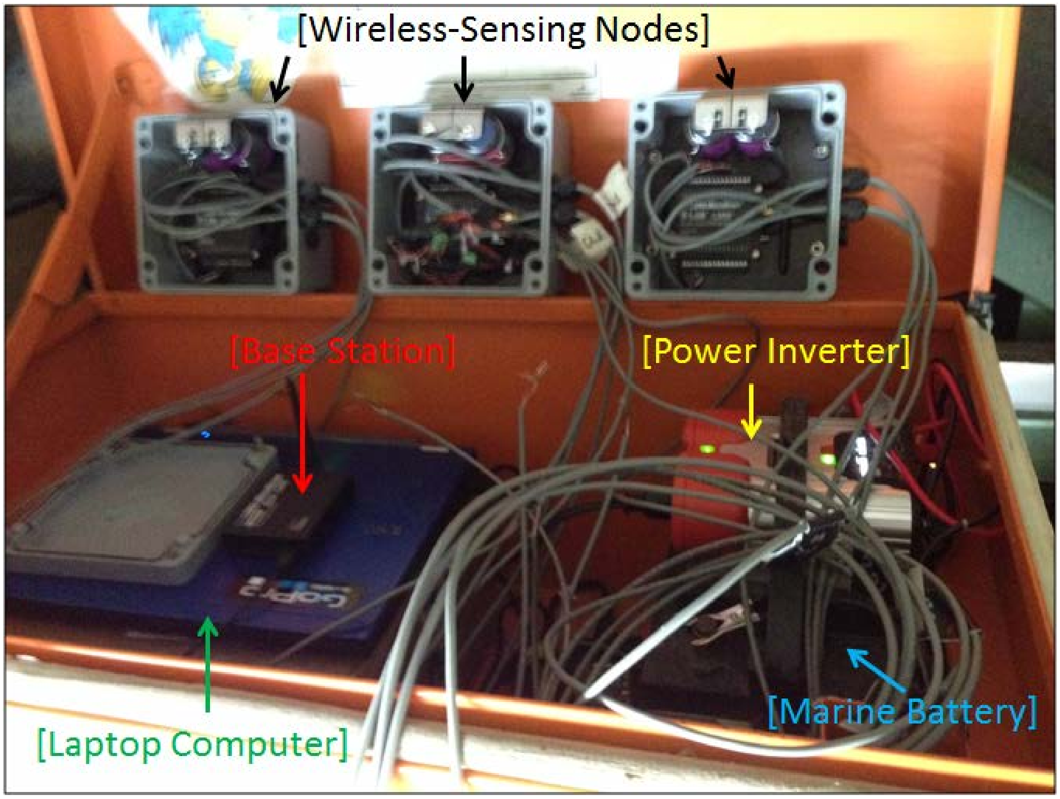

Figure A.9. Field instrumentation wireless sensing system.

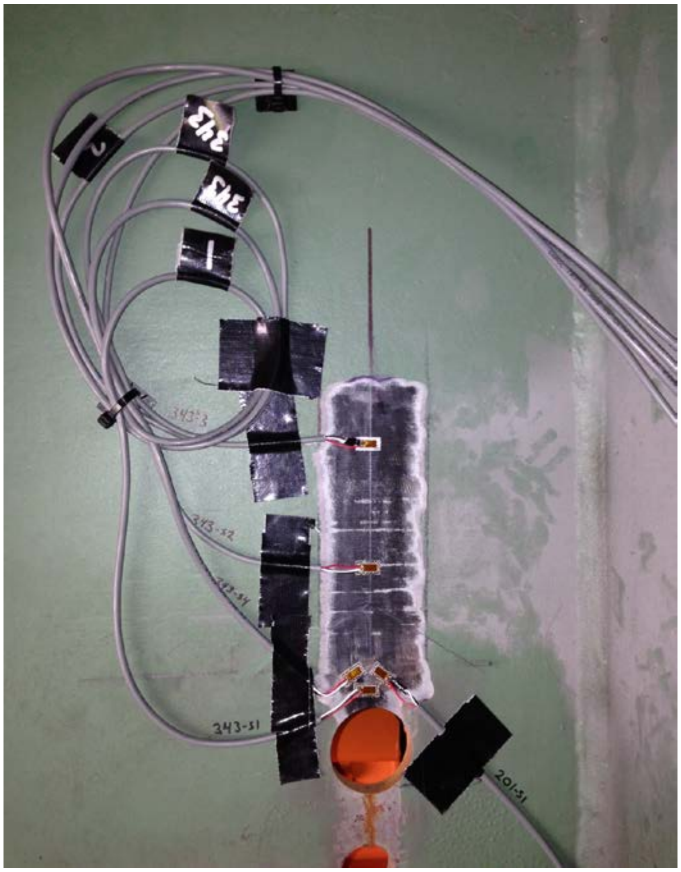

Figure A.10. Strain gauges welded to East face of Beam 3.


Figure A.11. Potentiometers on East face of Beam 3.


Figure A.12. Condition of roadway directly above fatigue-prone detail.

Figure A.13. Approach roadway.

APPENDIX B

FIELD INSTRAMENTATION STRAIN DIAGRAMS

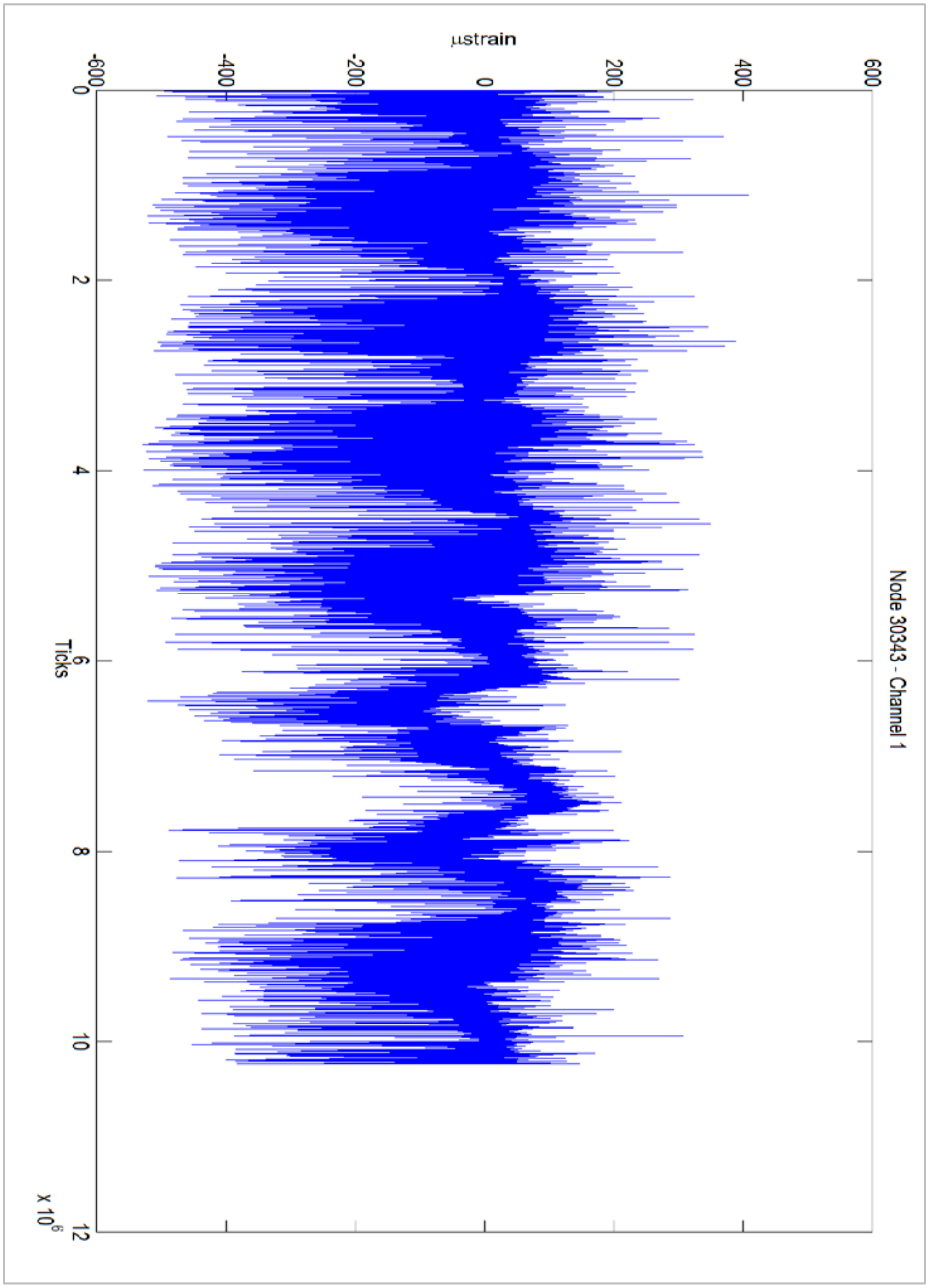

Figure B.1. Raw strain recordings – Node 30343 – Channel 1 – (Gauge 4).

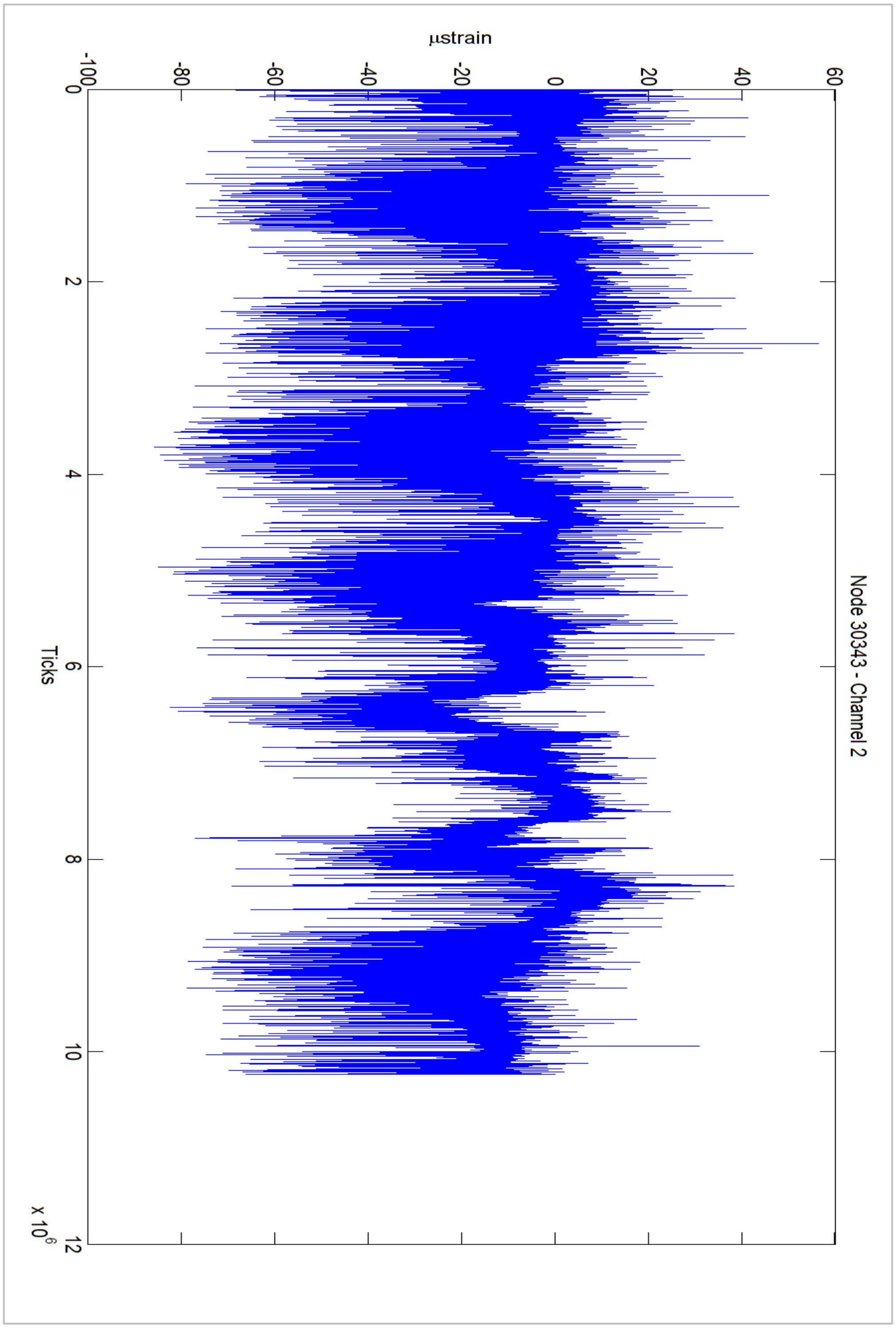

Figure B.2. Raw strain recordings – Node 30343 – Channel 2 – (Gauge 6).

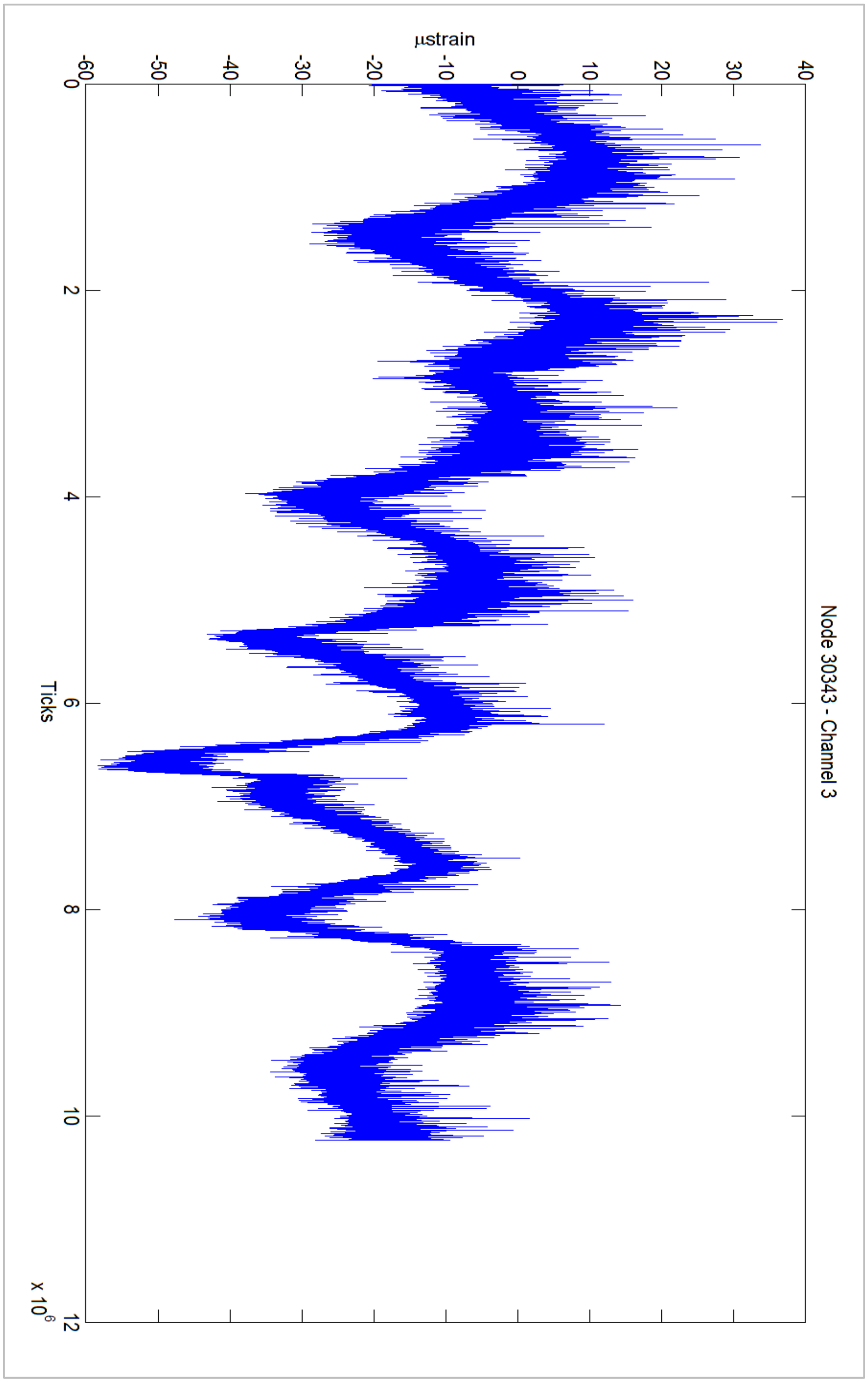

Figure B.3. Raw strain recordings – Node 30343 – Channel 3 – (Gauge 7).

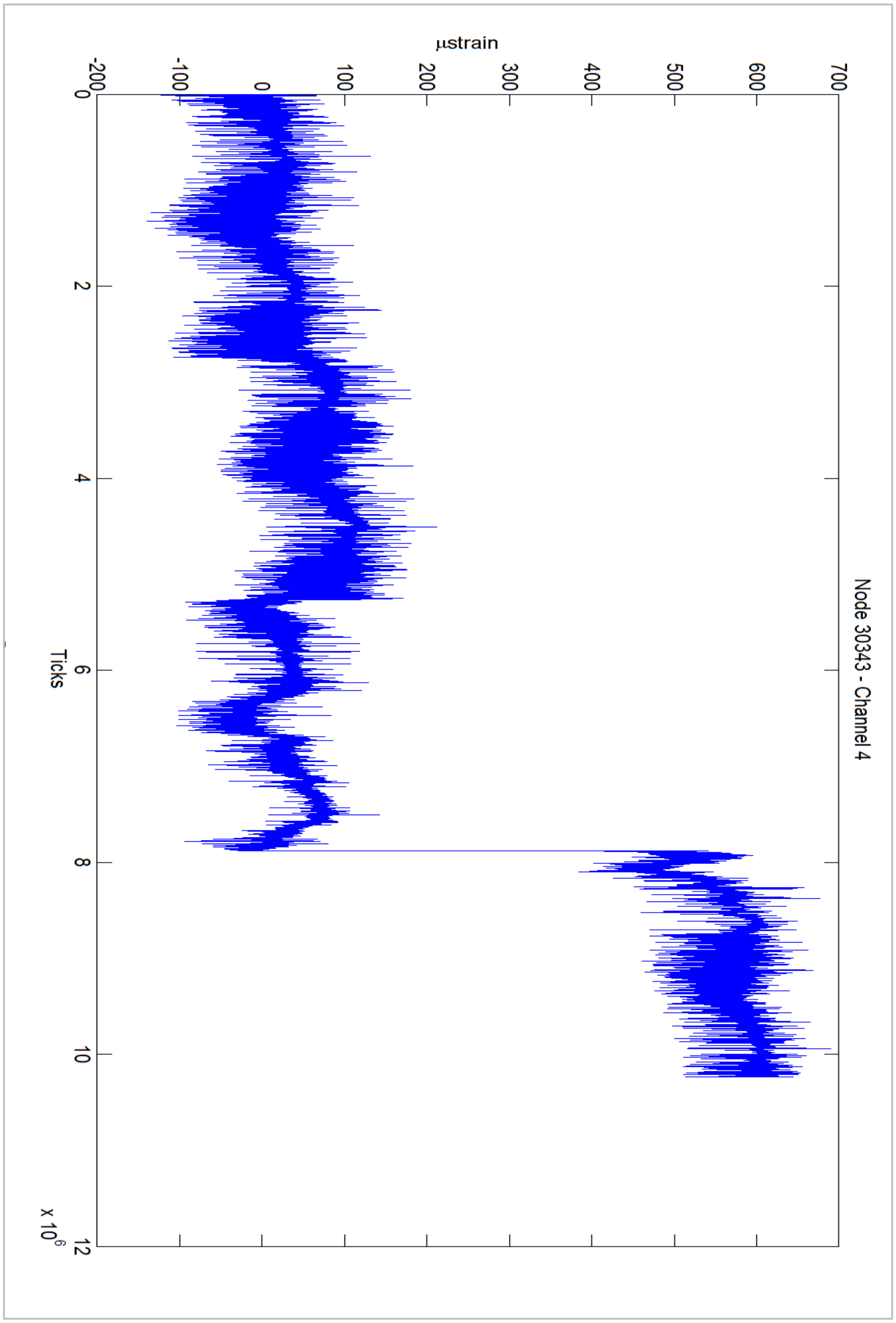

Figure B.4. Raw strain recordings – Node 30343 – Channel 4 – (Gauge 5).

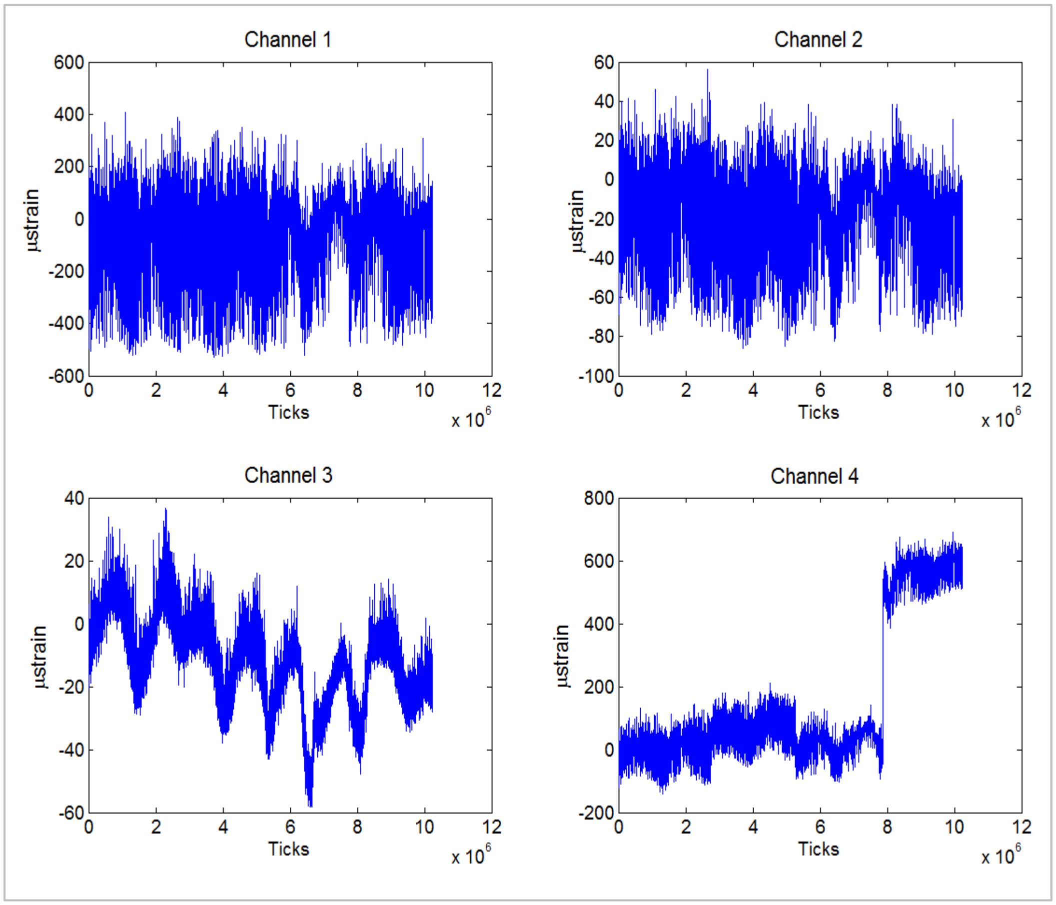

Figure B.5. Raw strain recordings – Node 30343 – All channels.

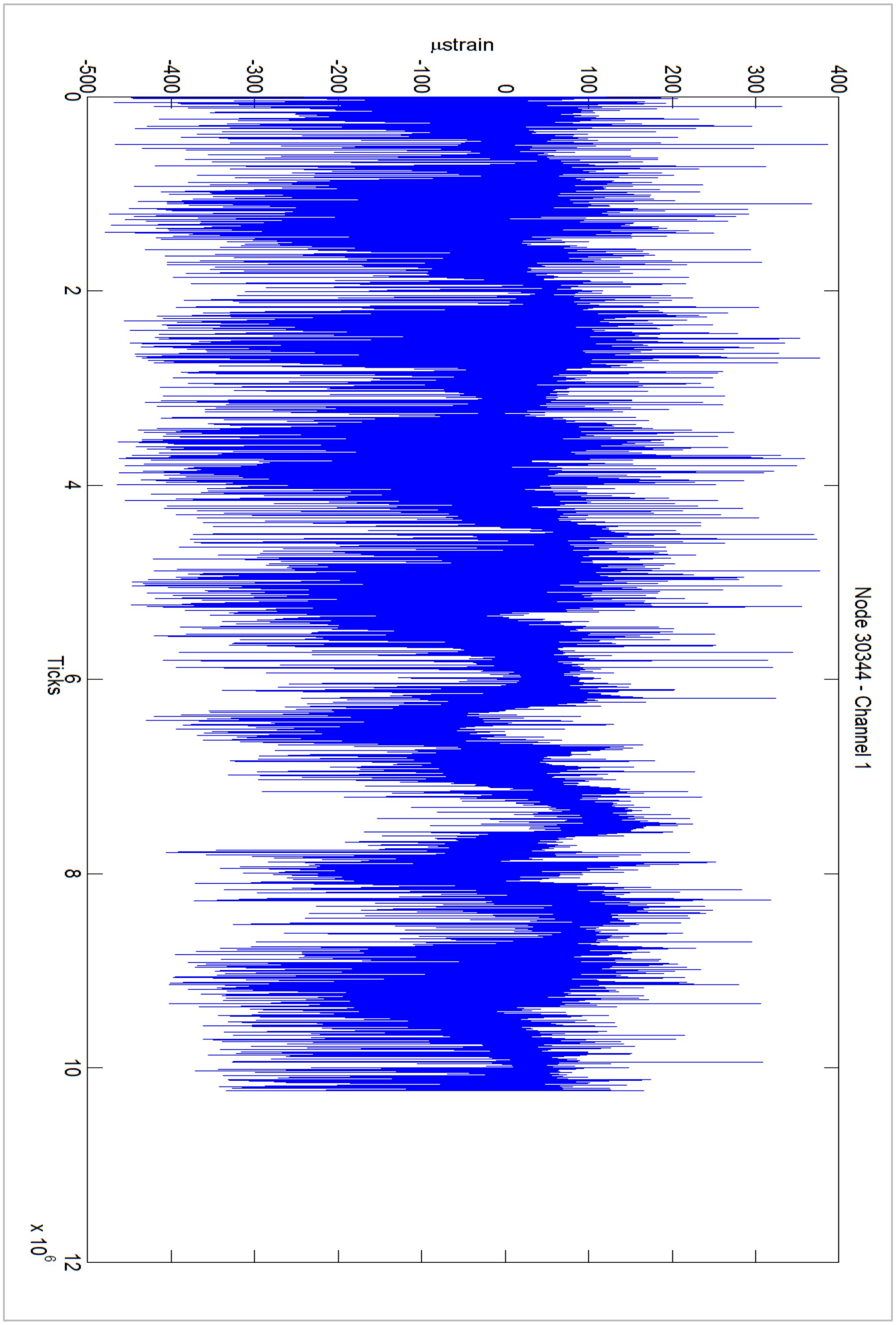

Figure B.6. Raw strain recordings – Node 30344 – Channel 1 – (Gauge 8).

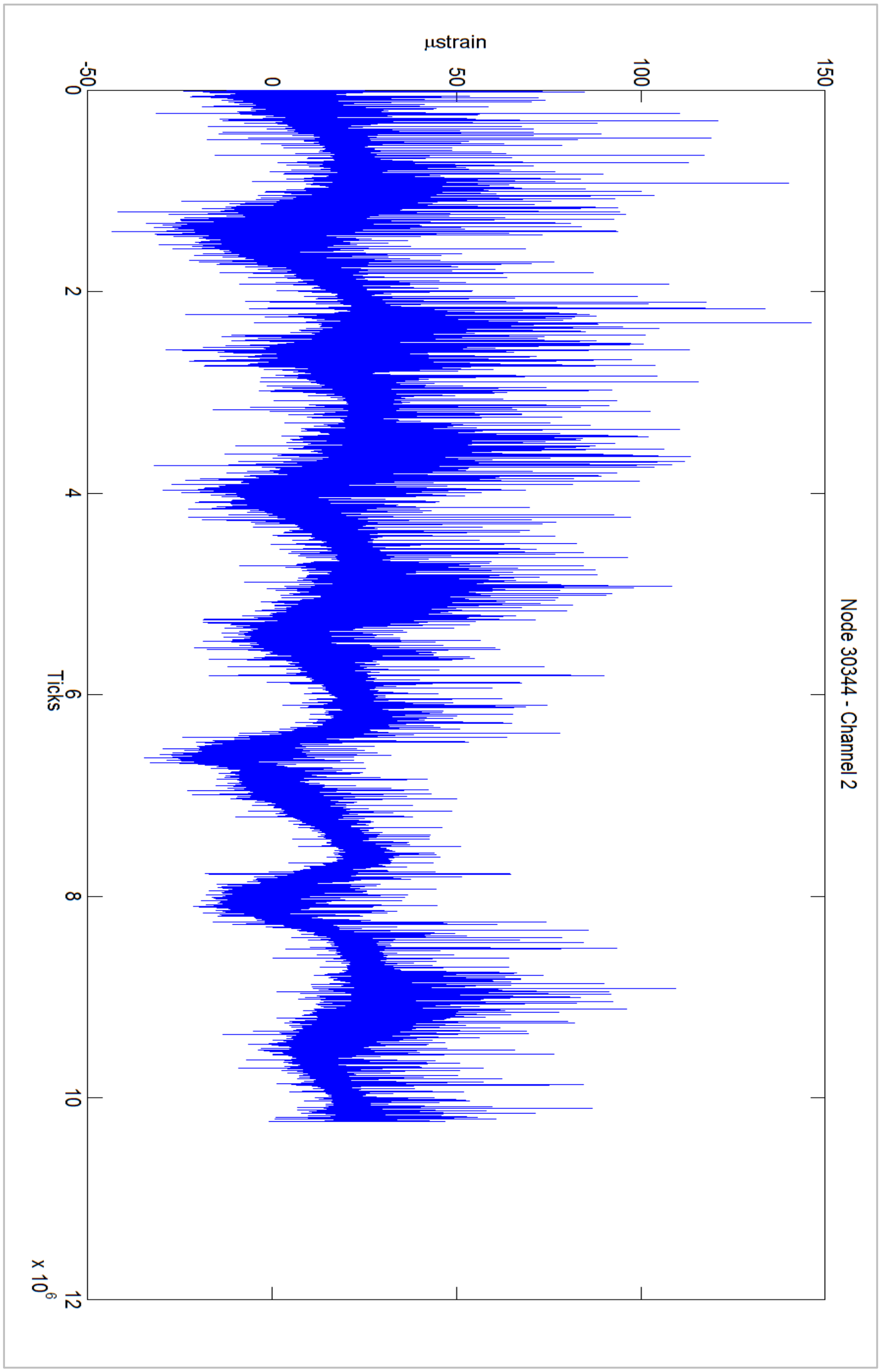

Figure B.7. Raw strain recordings – Node 30344 – Channel 2 – (Gauge 10).

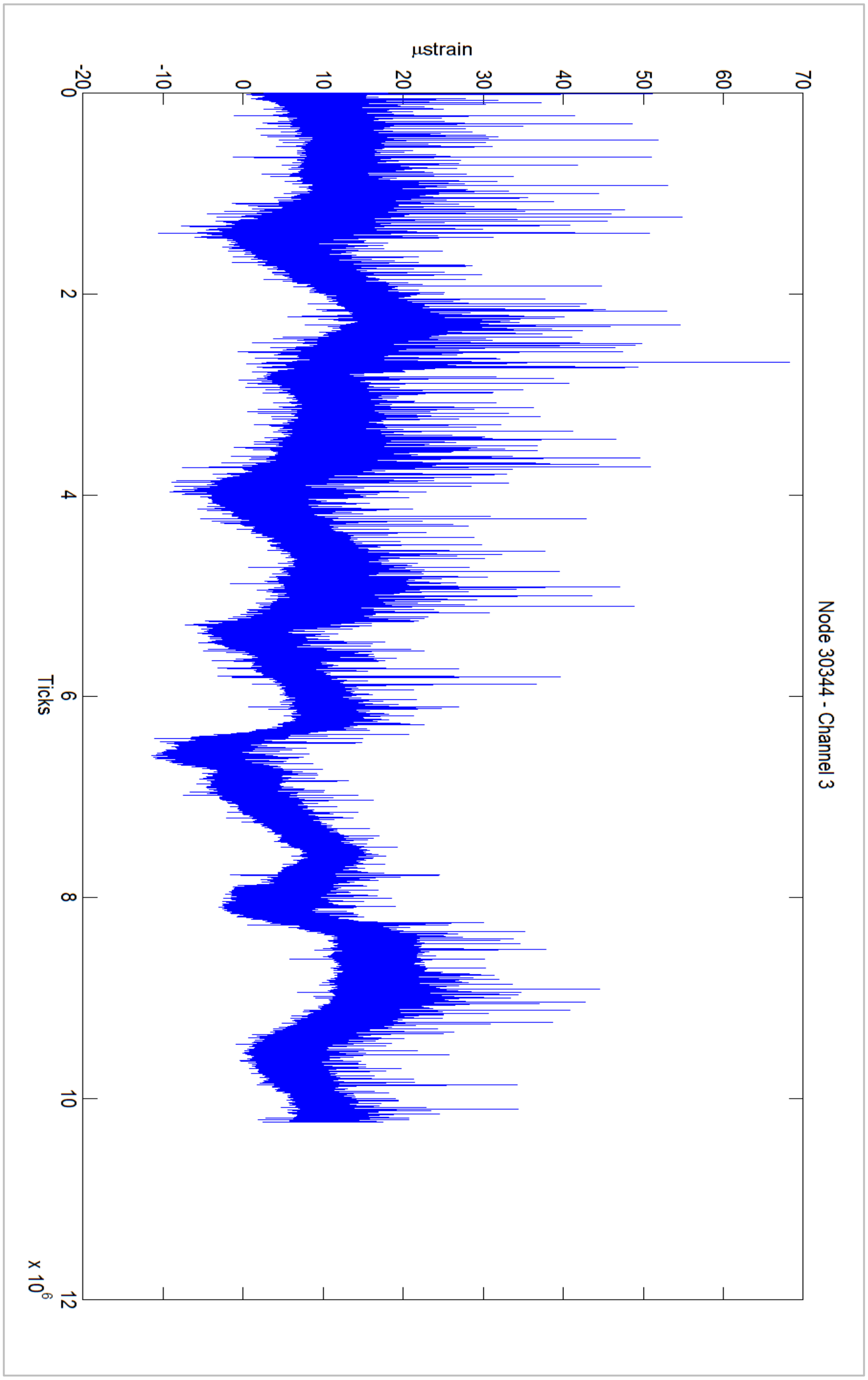

Figure B.8. Raw strain recordings – Node 30344 – Channel 3 – (Gauge 11).

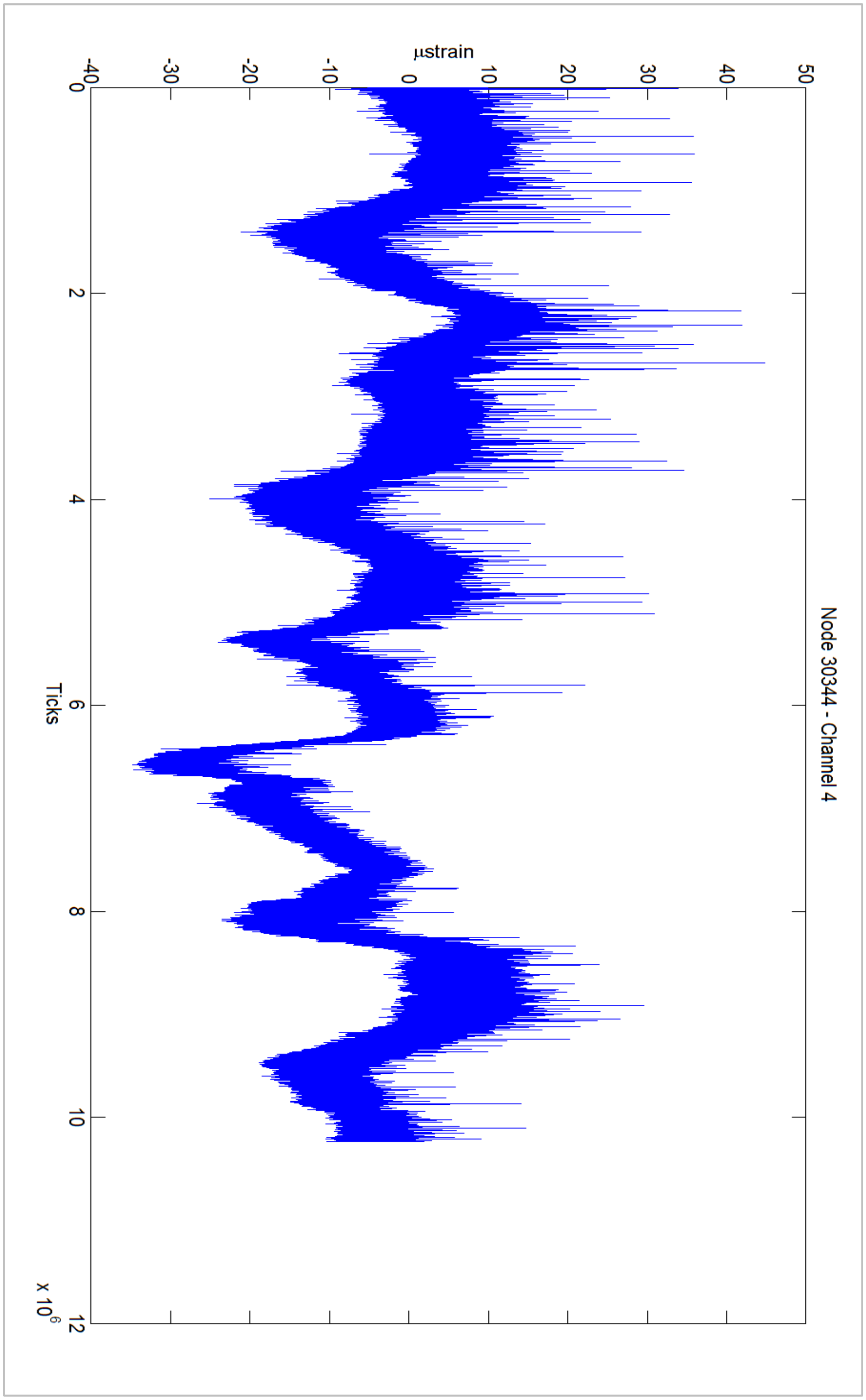

Figure B.9. Raw strain recordings – Node 30344 – Channel 4 – (Gauge 12).

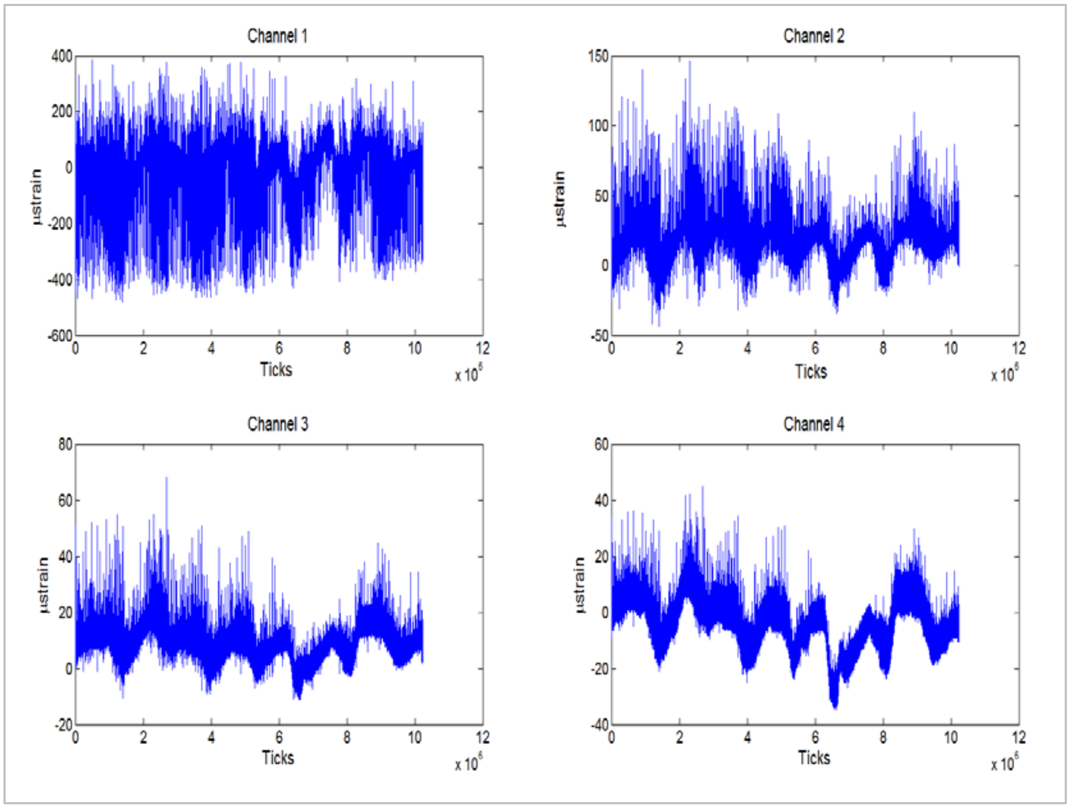

Figure B.10. Raw strain recordings – Node 30344 – All channels.

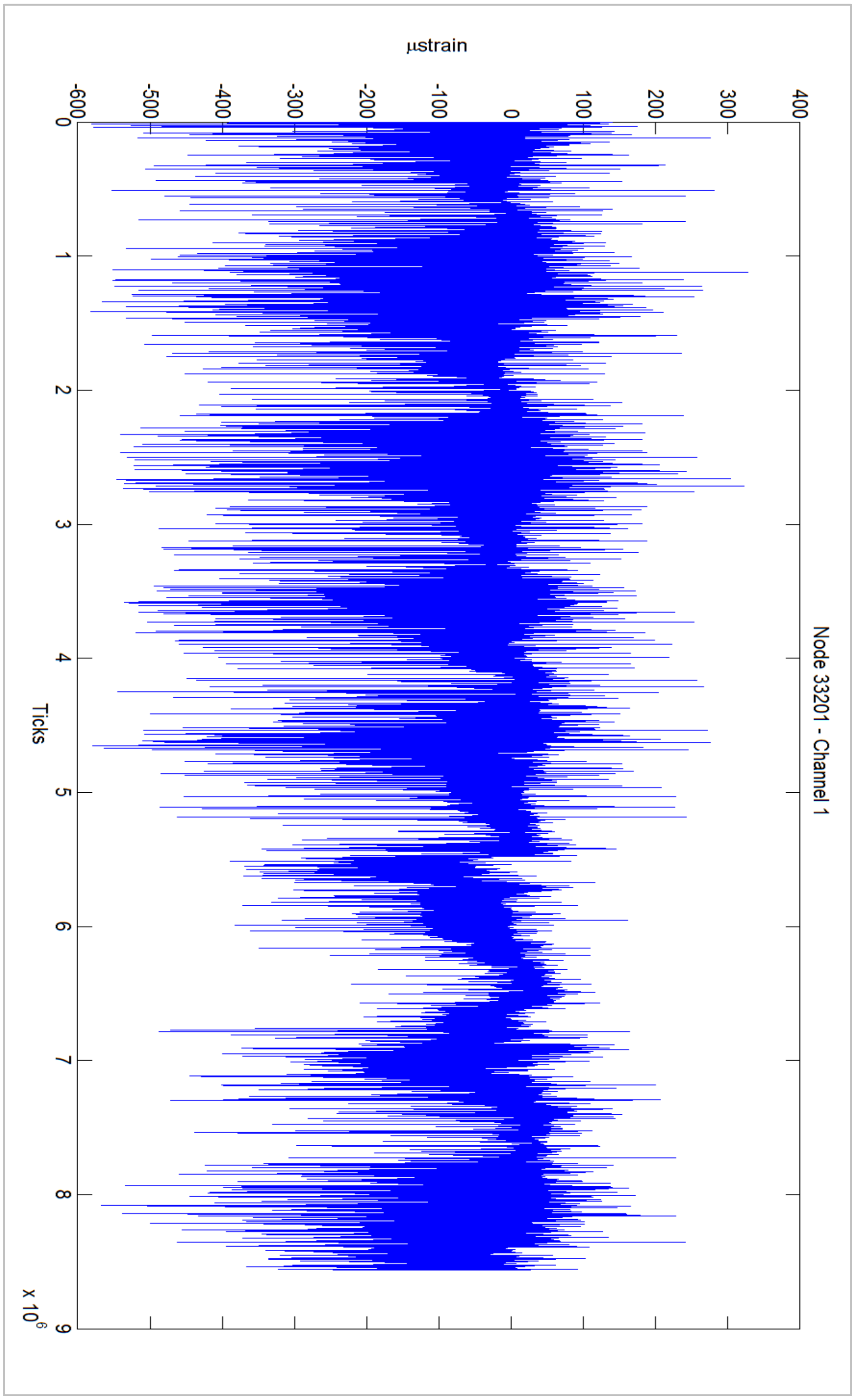

Figure B.11. Raw strain recordings – Node 33201 – Channel 1 – (Gauge 3).

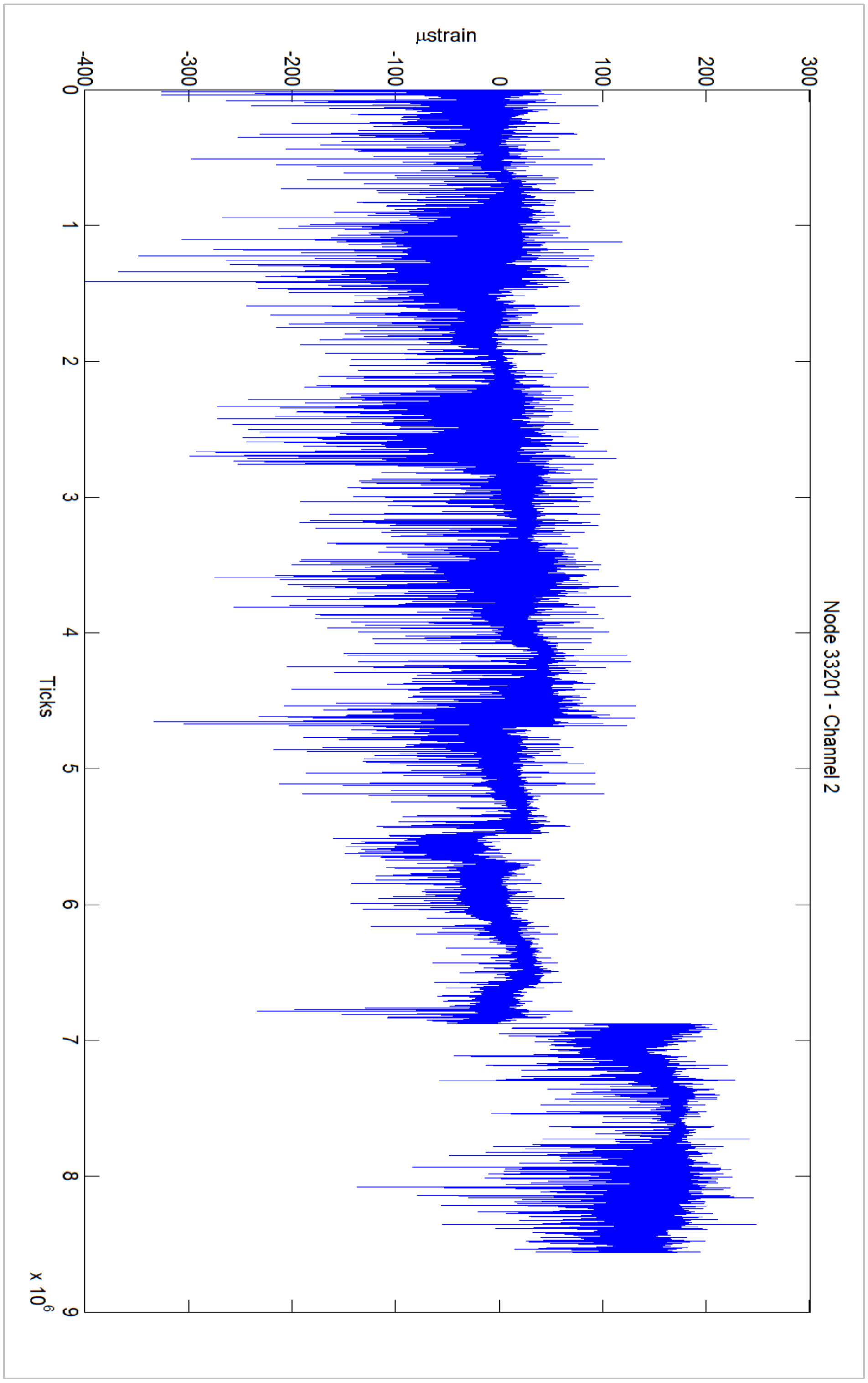

Figure B.12. Raw strain recordings – Node 33201 – Channel 2 – (Gauge 2).

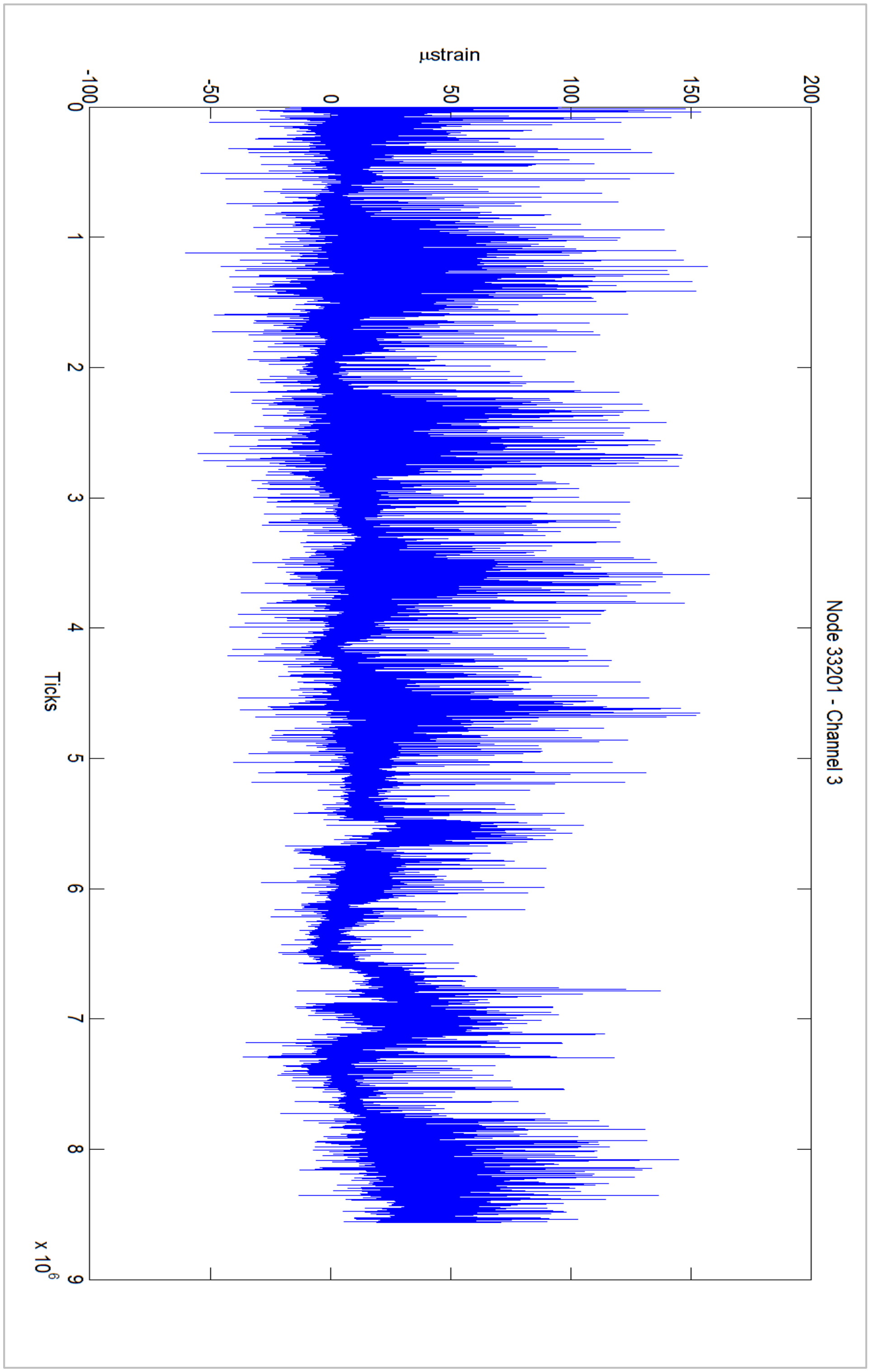

Figure B.13. Raw strain recordings – Node 33201 – Channel 3 – (Gauge 1).

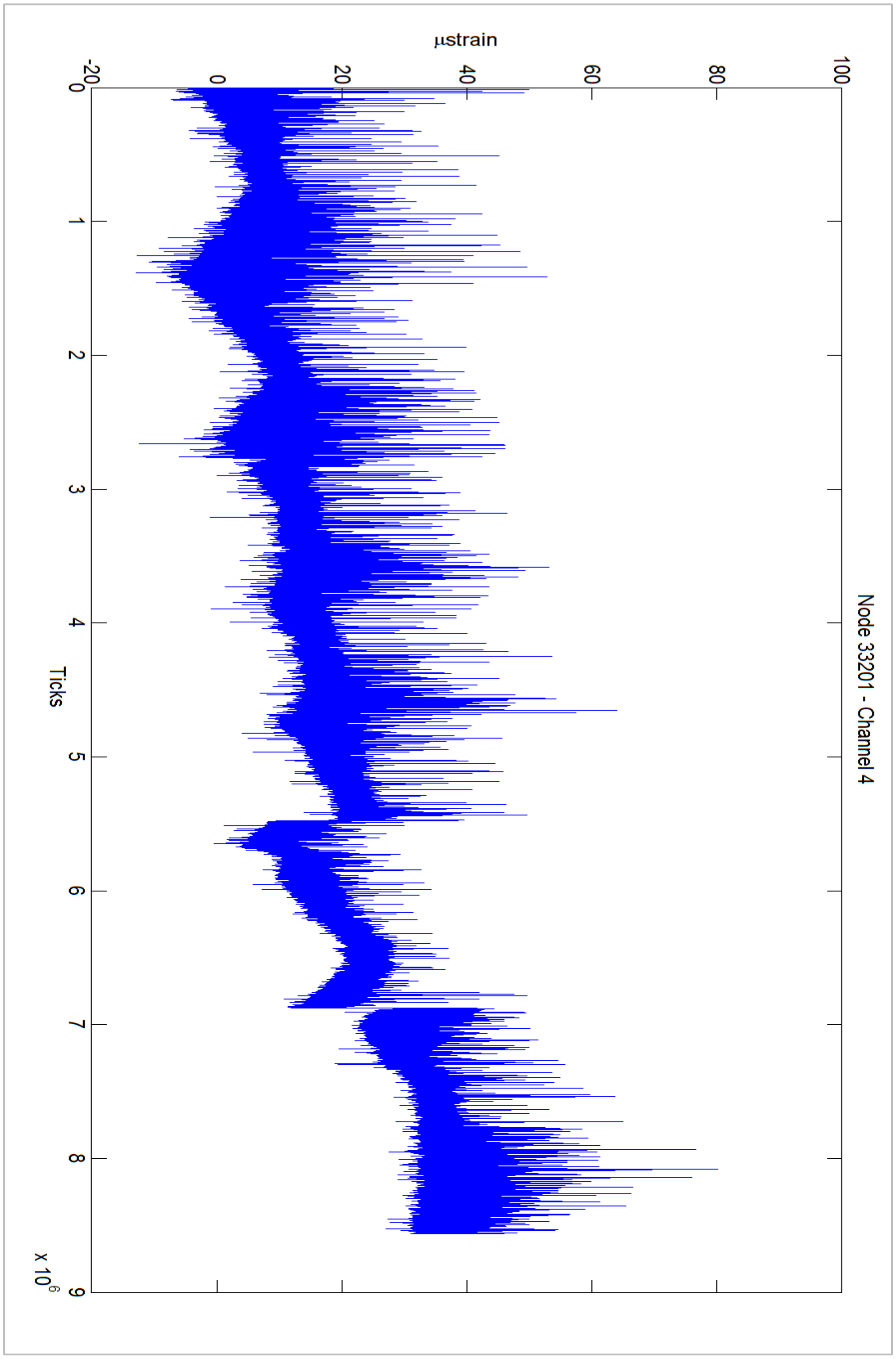

Figure B.14. Raw strain recordings – Node 33201 – Channel 4 – (Gauge 9).

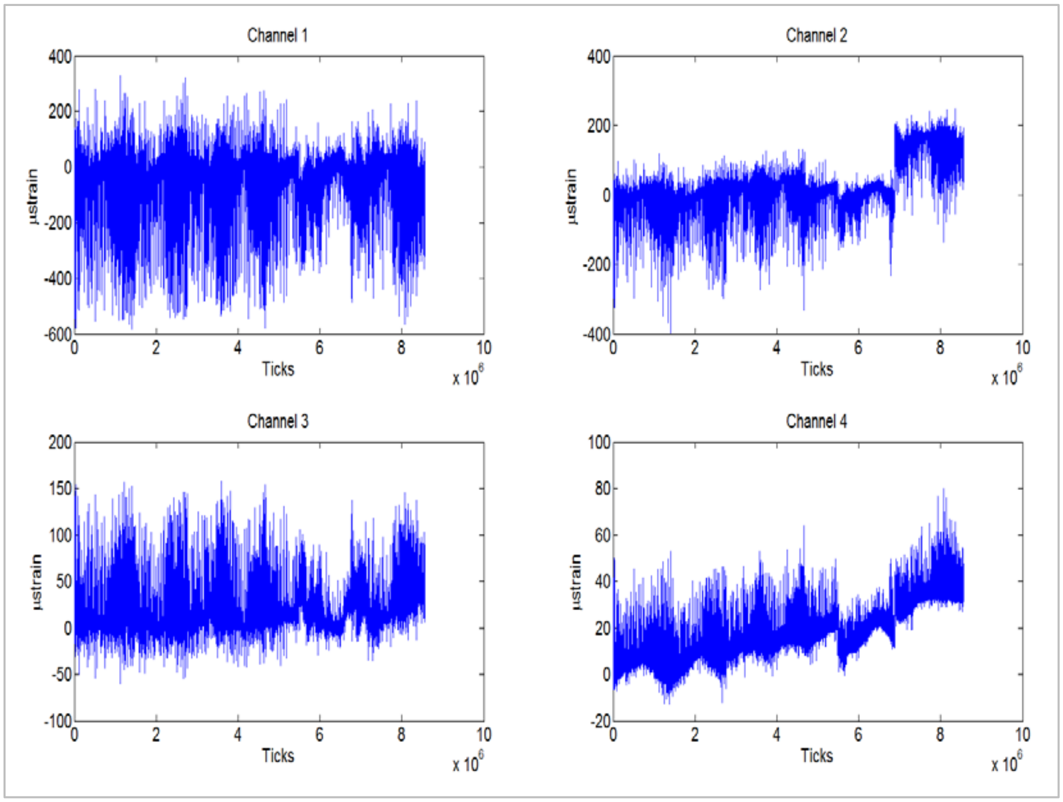

Figure B.15. Raw strain recordings – Node 33201 – All channels.

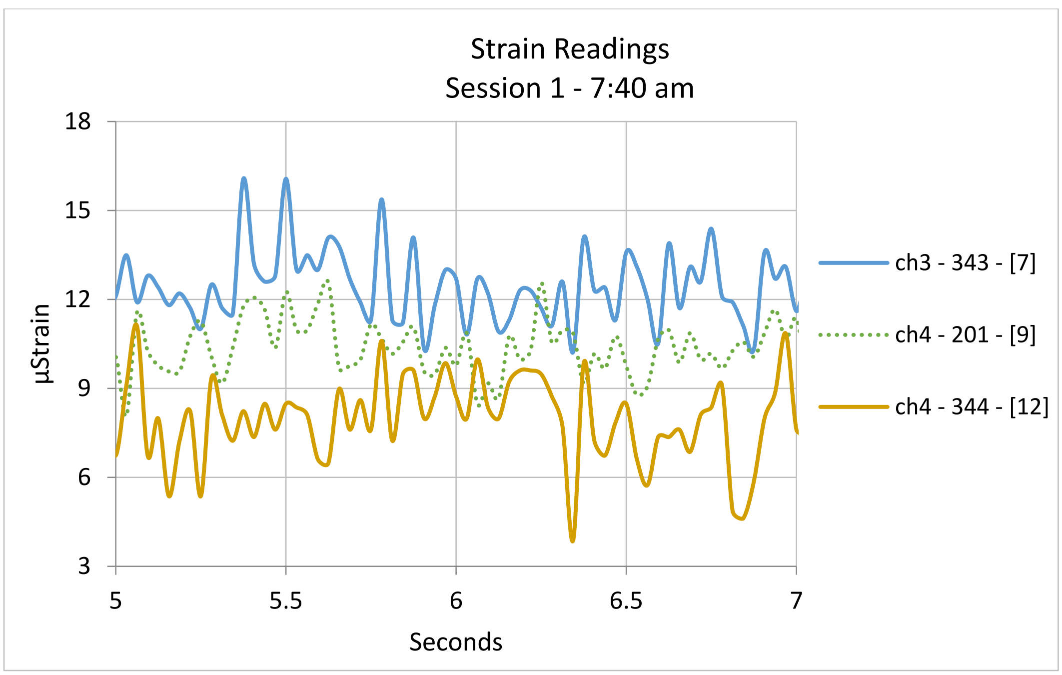

Figure B.16. Sample strain reading comparison – Session 1- 7:40 am.

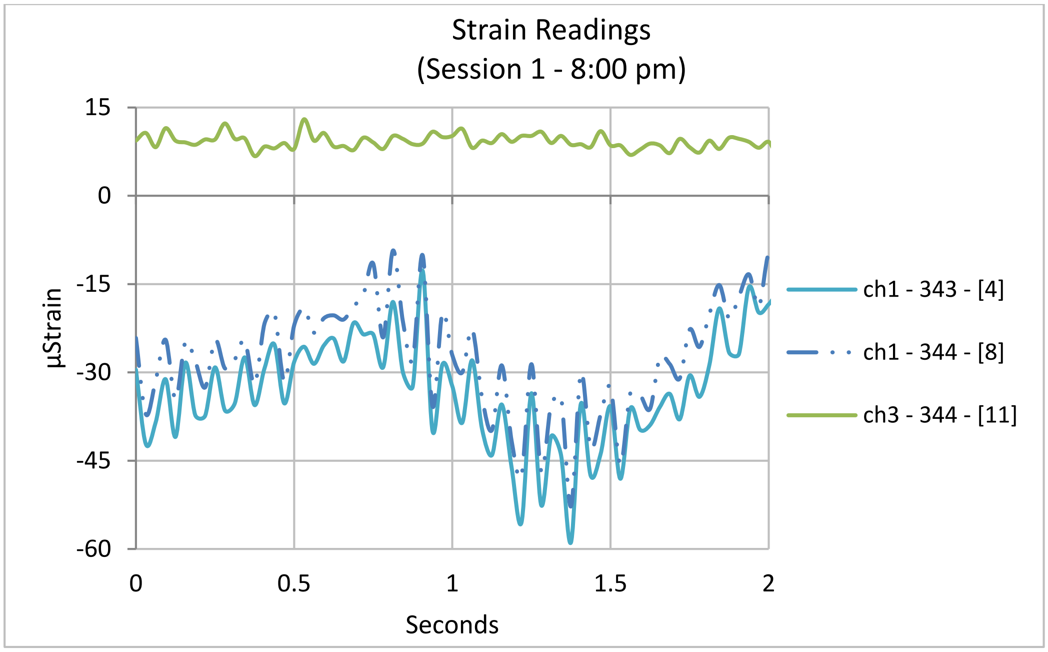

Figure B.17. Sample strain reading comparison – Session 1- 8:00 pm.

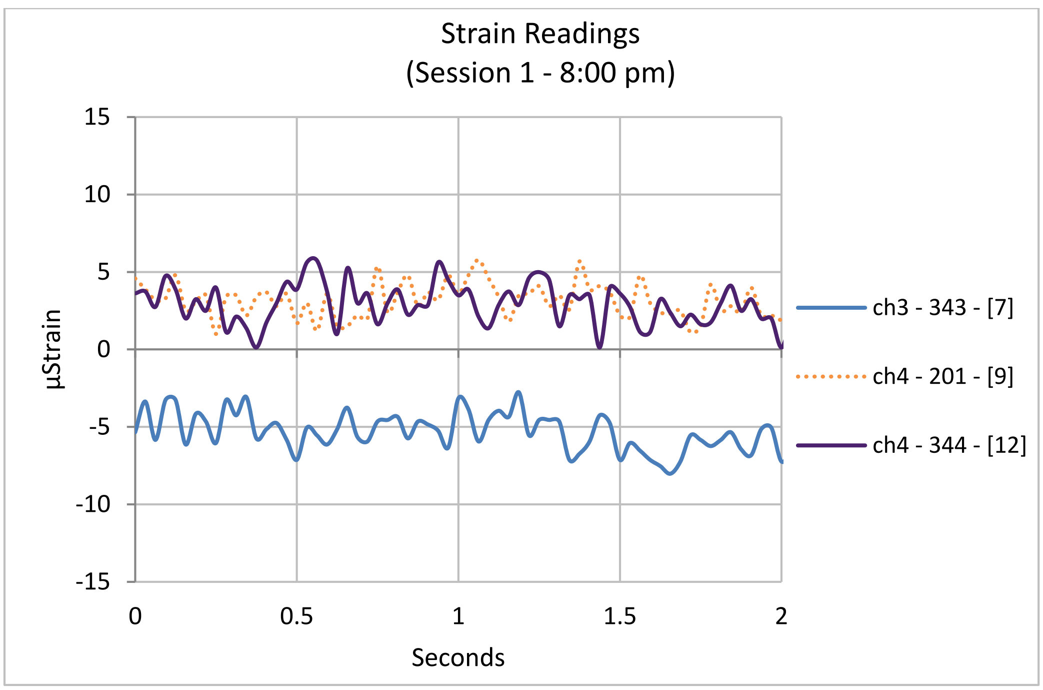

Figure B.18. Sample strain reading comparison – Session 1- 8:00 pm.

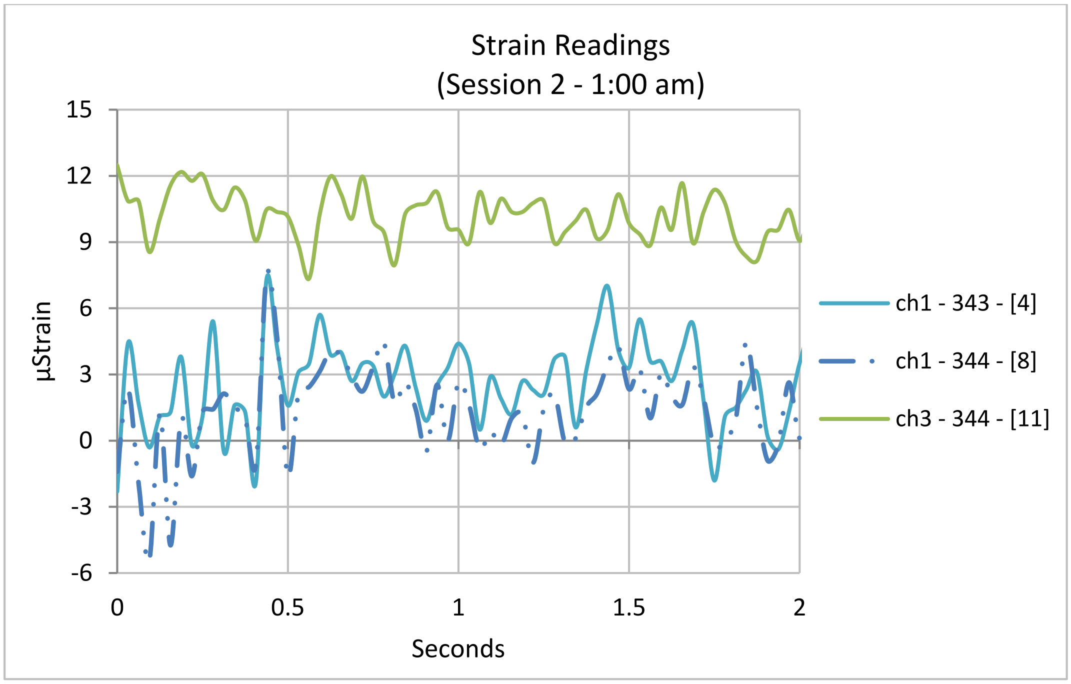

Figure B.19. Sample strain reading comparison – Session 2- 1:00 am.

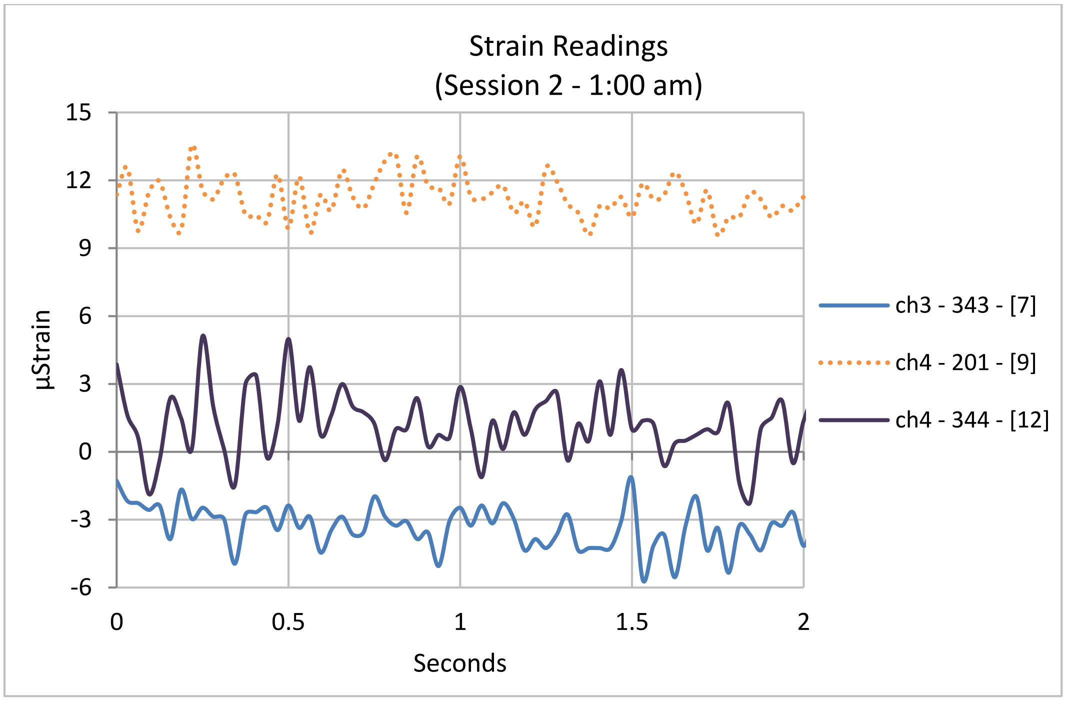

Figure B.20. Sample strain reading Comparison – Session 2- 1:00 am.

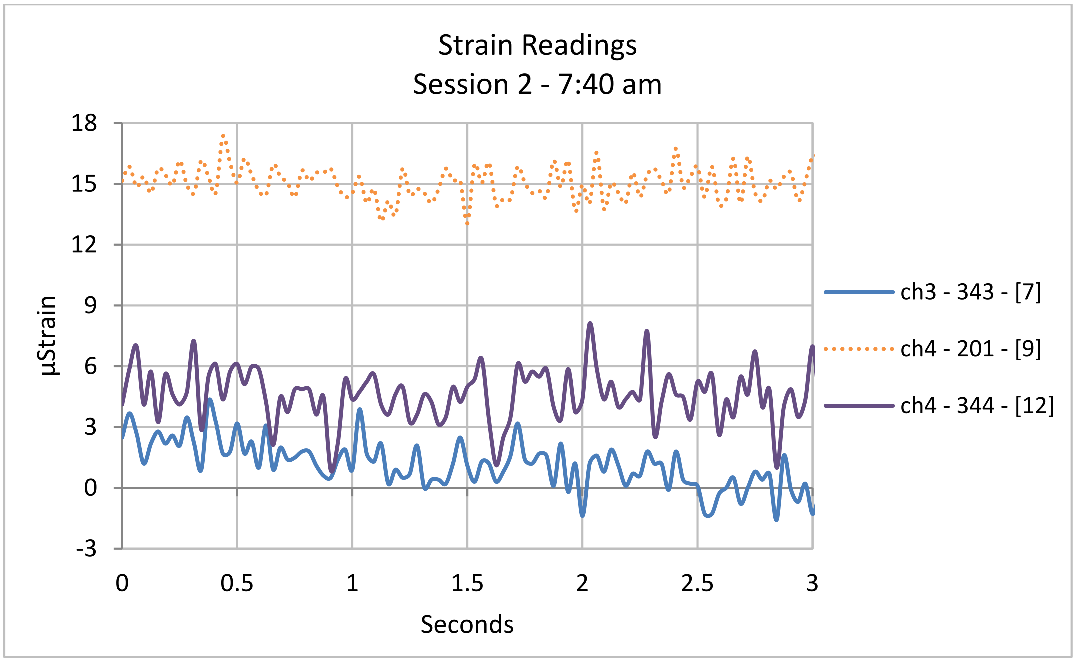

Figure B.21. Sample strain readings comparison – Session 2- 7:40 am.

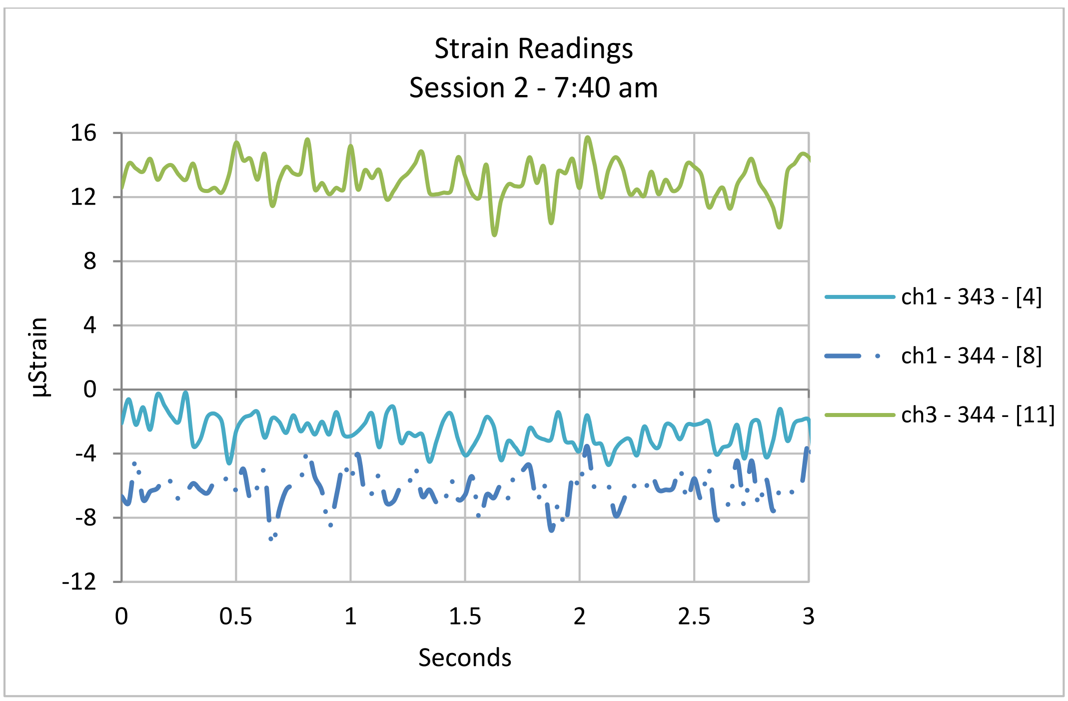

Figure B.22. Sample strain reading comparison – Session 2- 7:40 am.

APPENDIX C

FIELD INSTRAMENTATION HISTOGRAM PLOTS

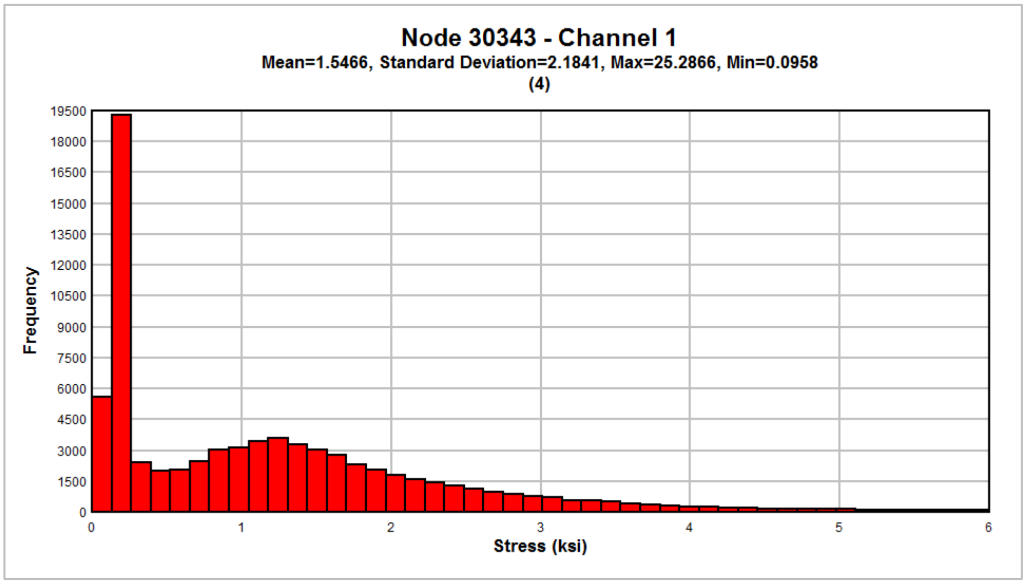

Figure C.1. Strain recordings histogram – Node 30343 – Channel 1 – (Gauge 4).

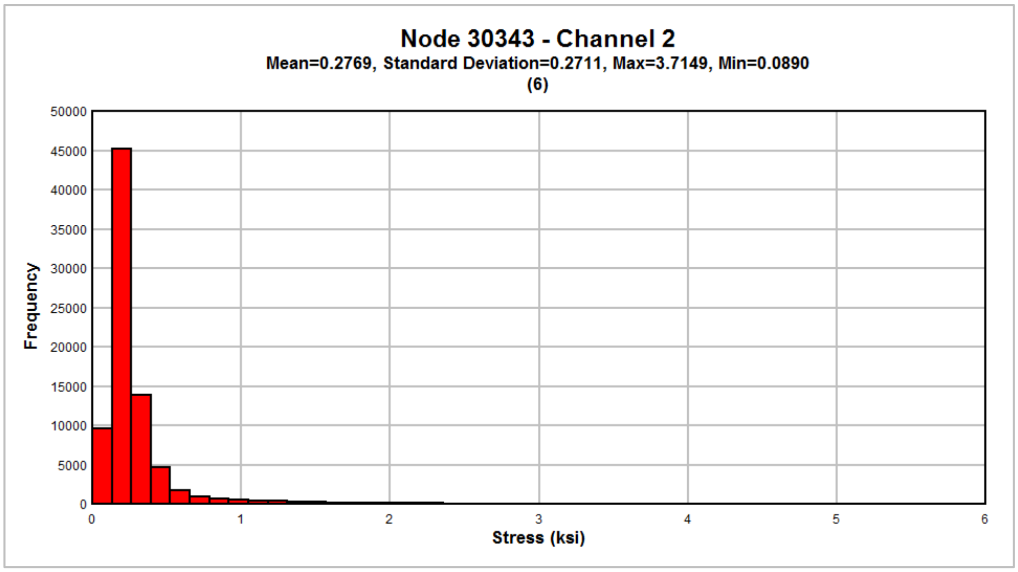

Figure C.2. Strain recordings histogram – Node 30343 – Channel 2 – (Gauge 6).

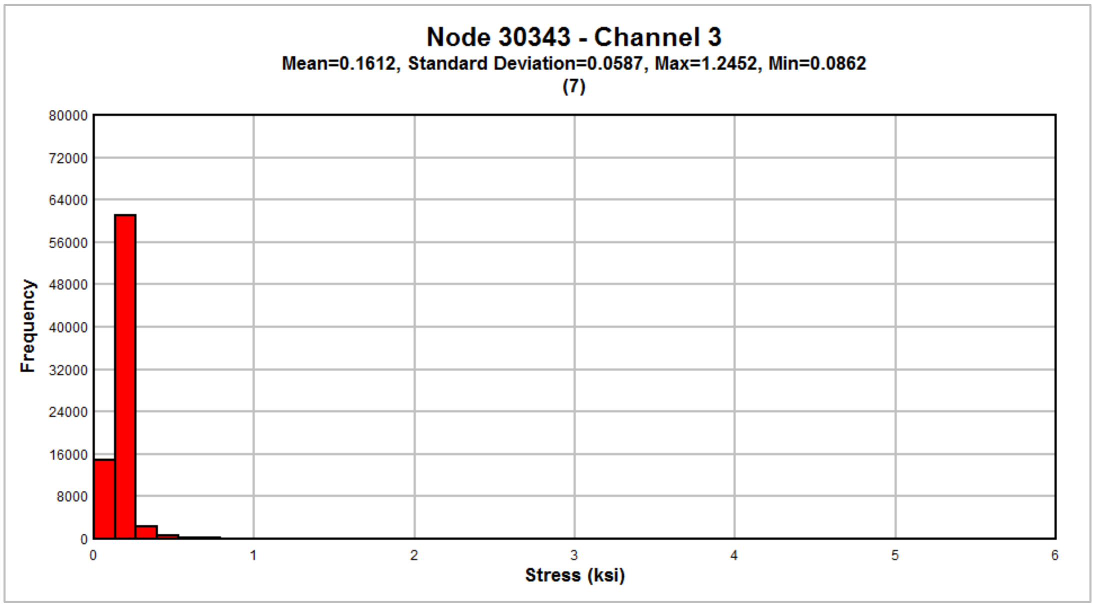

Figure C.3. Strain recordings histogram – Node 30343 – Channel 3 – (Gauge 7).

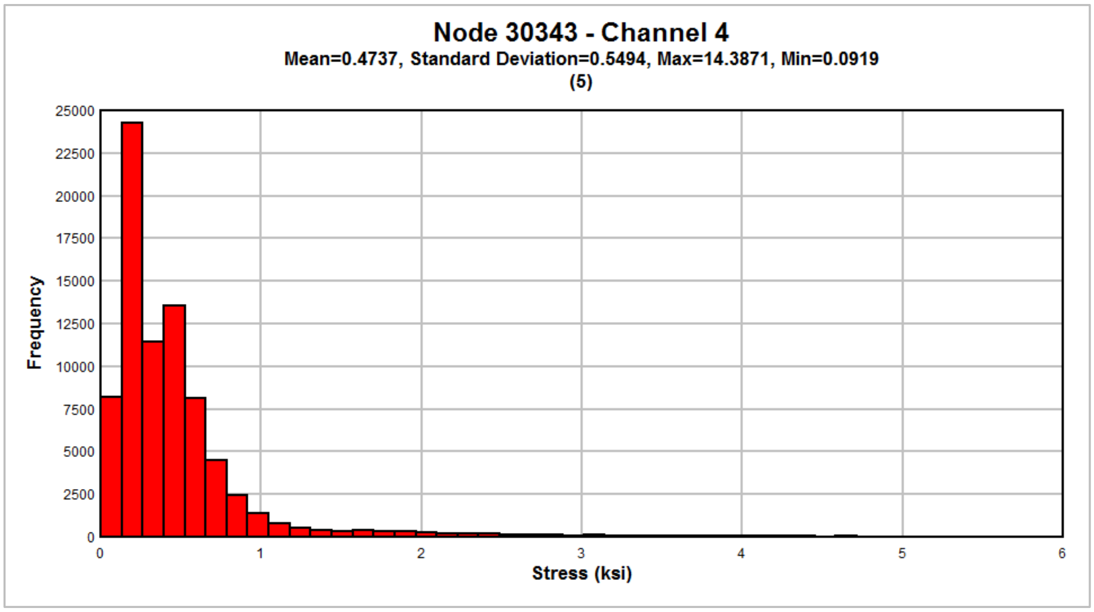

Figure C.4. Strain recordings histogram – Node 30343 – Channel 4 – (Gauge 5).

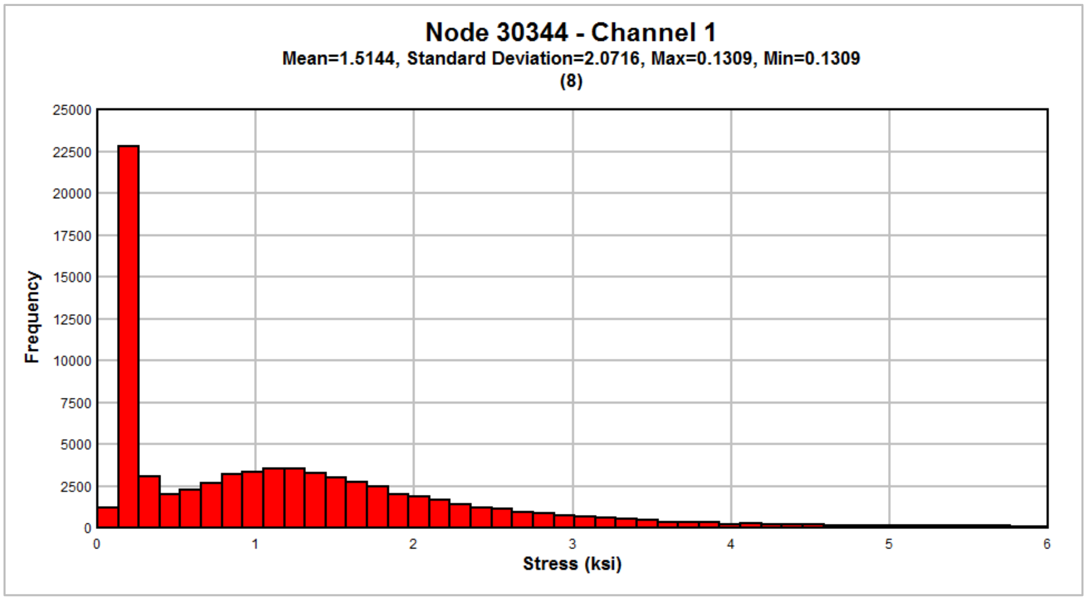

Figure C.5. Strain recordings histogram – Node 30344 – Channel 1 – (Gauge 8).

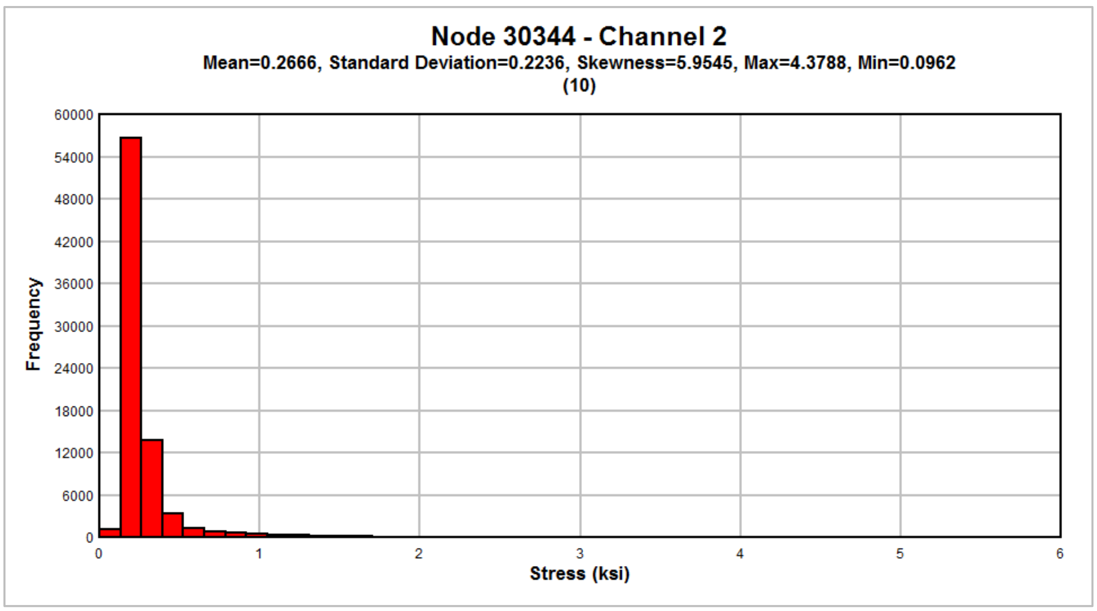

Figure C.6. Strain recordings histogram – Node 30344 – Channel 2 – (Gauge 10).

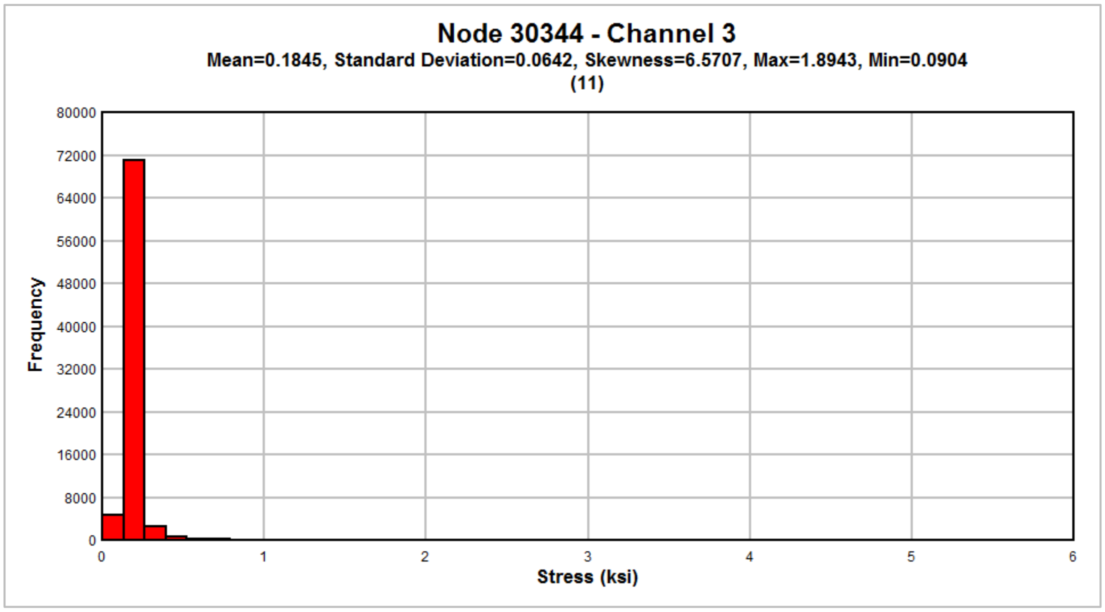

Figure C.7. Strain recordings histogram – Node 30344 – Channel 3 – (Gauge 11).

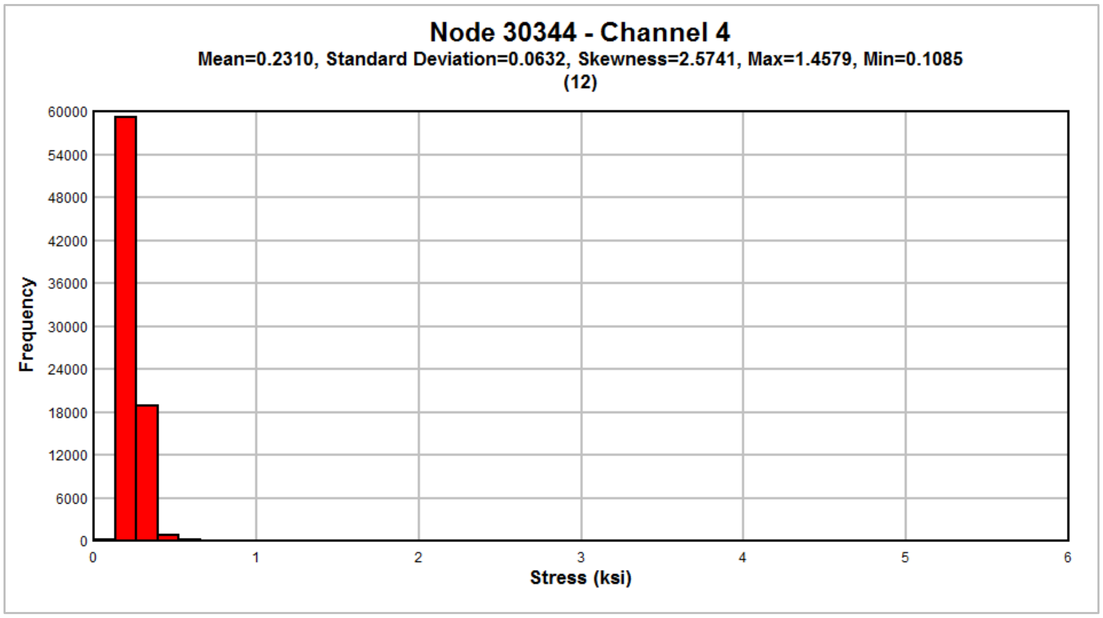

Figure C.8. Strain recordings histogram – Node 30344 – Channel 4 – (Gauge 12).

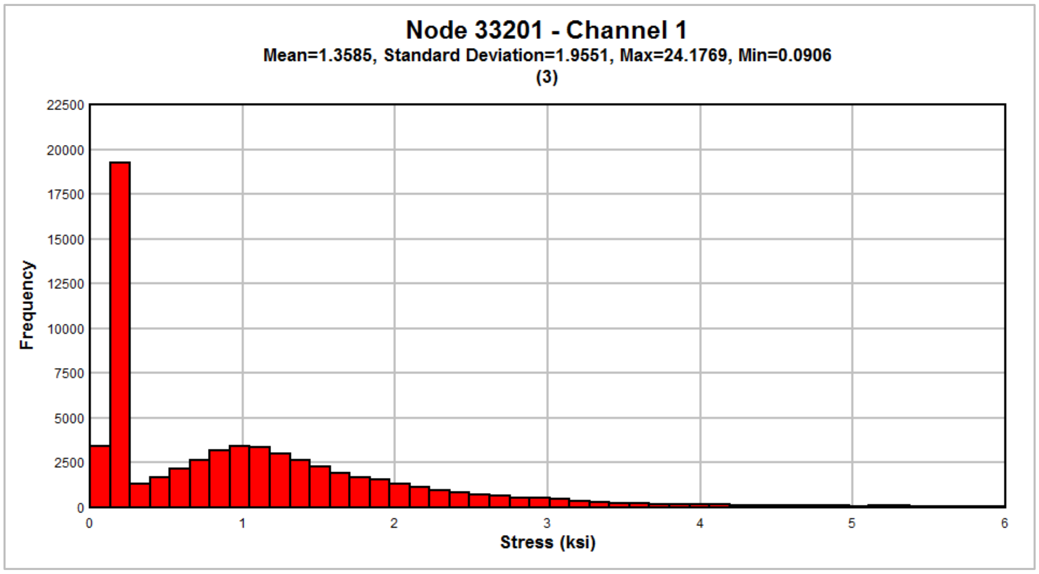

Figure C.9. Strain recordings histogram – Node 33201 – Channel 1 – (Gauge 3).

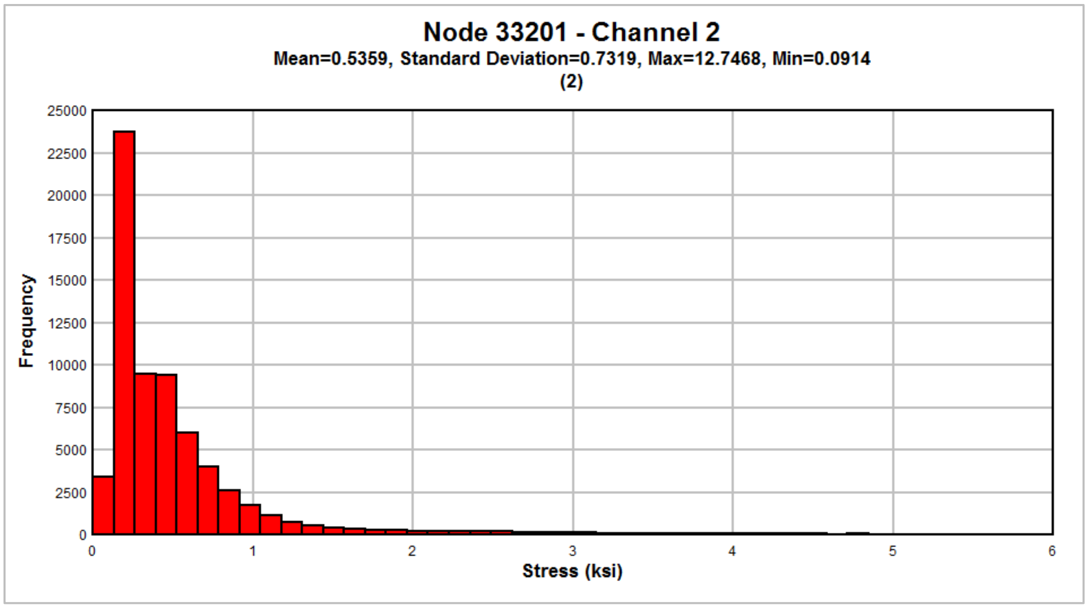

Figure C.10. Strain recordings histogram – Node 33201 – Channel 2 – (Gauge 2).

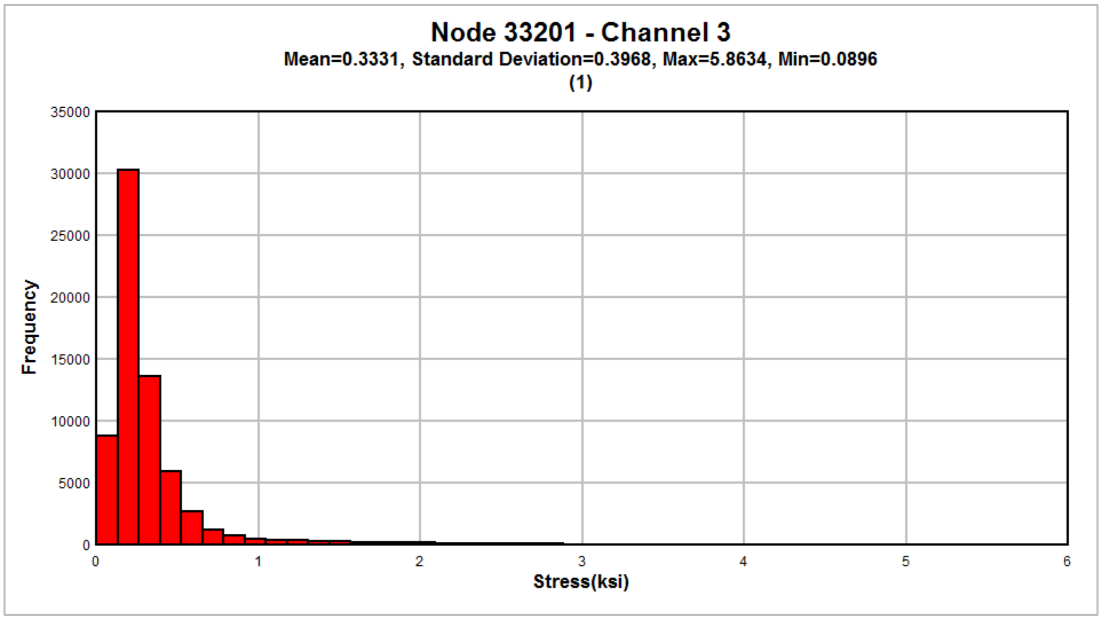

Figure C.11. Strain recordings histogram – Node 33201 – Channel 3 – (Gauge 1).

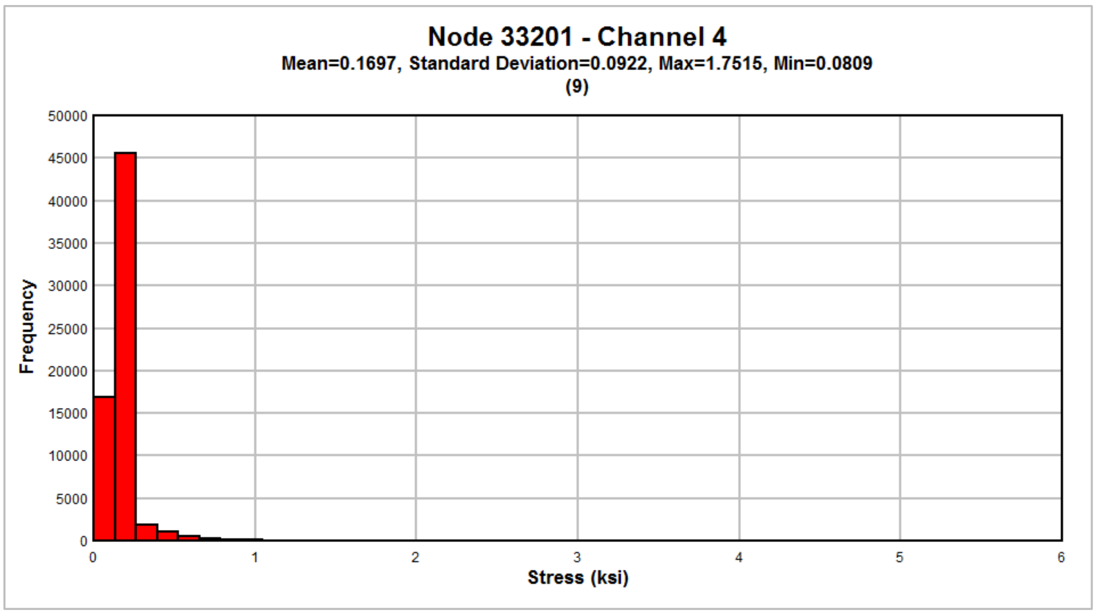

Figure C.12. Strain recordings histogram – Node 33201 – Channel 4 – (Gauge 9).

APPENDIX D

SAMPLE CALCULATIONS

As a result of crack re-initiation on DelDOT 1678-00, multiple crack stop holes have been drilled. As discussed in literature review undersized drilled hole may cause in the continued propagation of fatigue crack. The overall purpose of drilling the hole is to remove the stress concentration permitting the crack to grow. Theoretically, the diameter of the hole required to arrest crack growth can be calculated from a formula developed by Rolfe and Barsom (1977), and later redeveloped by Fisher *et al.* (1980, 1990) and Dexter (2013). For this purposes of this study this formula shown below was utilized in order to calculate the minimum diameter hole required to cease crack growth. This formula was developed based on empirical data by Rolfe and Barsom.

$$D = \frac{S_r \pi a}{8\sigma_y} \geq 1.0 \text{ in}$$ *(Source: Dexter 2013)*

where:
S_r = nominal stress range at crack tip - [24.9 ksi]
a = the half-crack length (inches) - [8.5/2]
σ_y = the yield stress of the material (ksi) – [36 ksi assumed for this study]

Substituting in the values determined for this study, reveals that the minimum hole diameter to arrest hole is 1.154 inches in diameter. The original crack stop hole diameter drilled in 2011 was 1.125 inches; thus is it is not surprising that the crack re-initiated. The subsequent hole drilled in 2013 measures 2 inches in diameter and by these simple calculations it should be sufficient to stop crack growth without implementing the proposed rehabilitation method.

It should be noted that the equation presented above is based on assumptions of a simplified stress field, which may not be representative of the much more distorted and complicated stress field in an actual bridge member.

APPENDIX E

ADDITIONAL LABORATORY TESTING PHOTOS

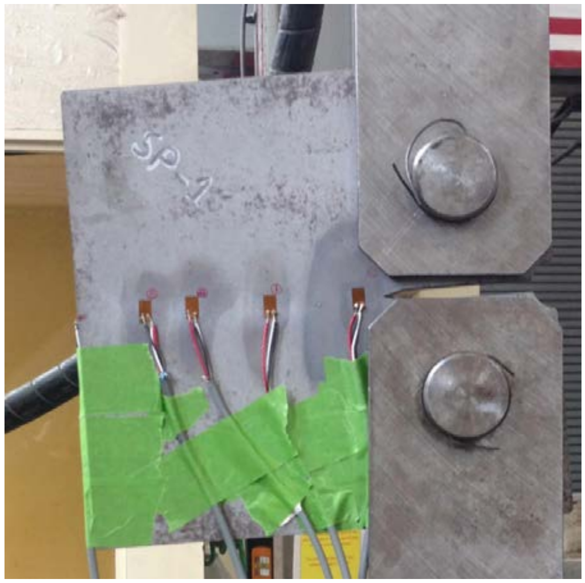

Figure E1. Fatigue testing setup of Specimen #1.

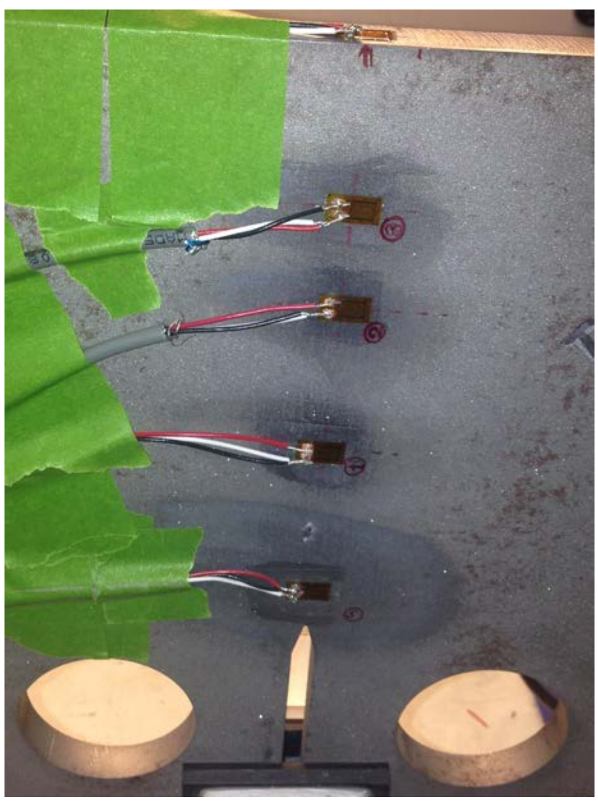

Figure E.2. Strain gauge instrumentation of Specimen #1.

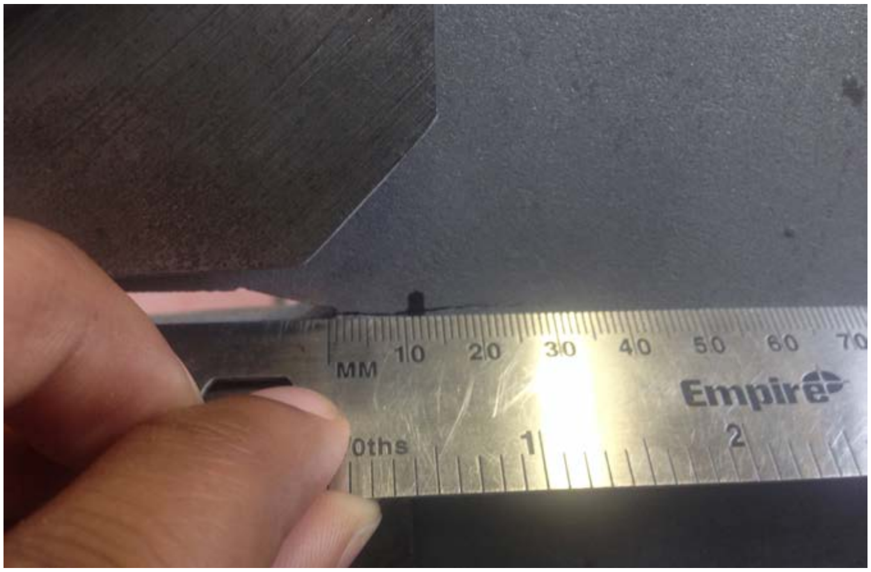

Figure E.3. Specimen #1 measurement after 130k cycles.

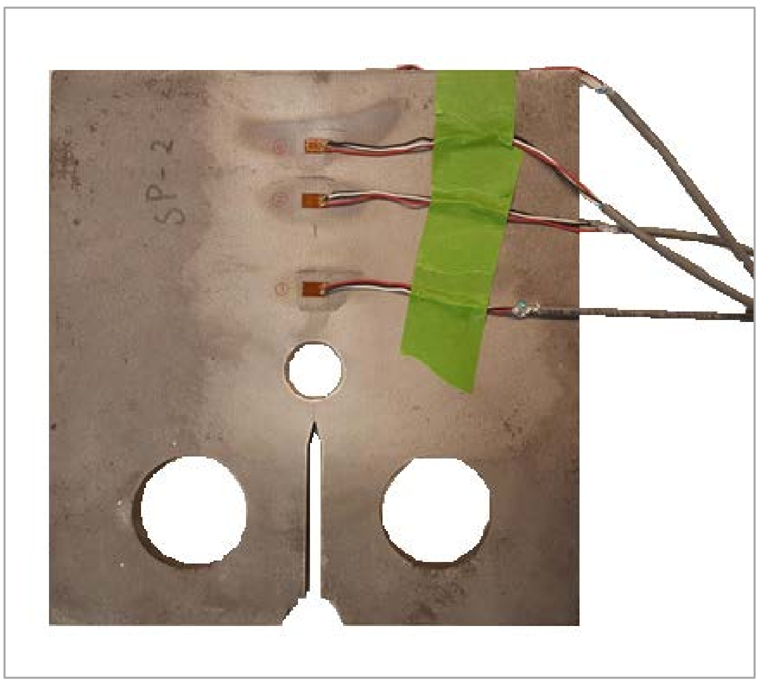

Figure E.4. Photo of instrumented Specimen #2.

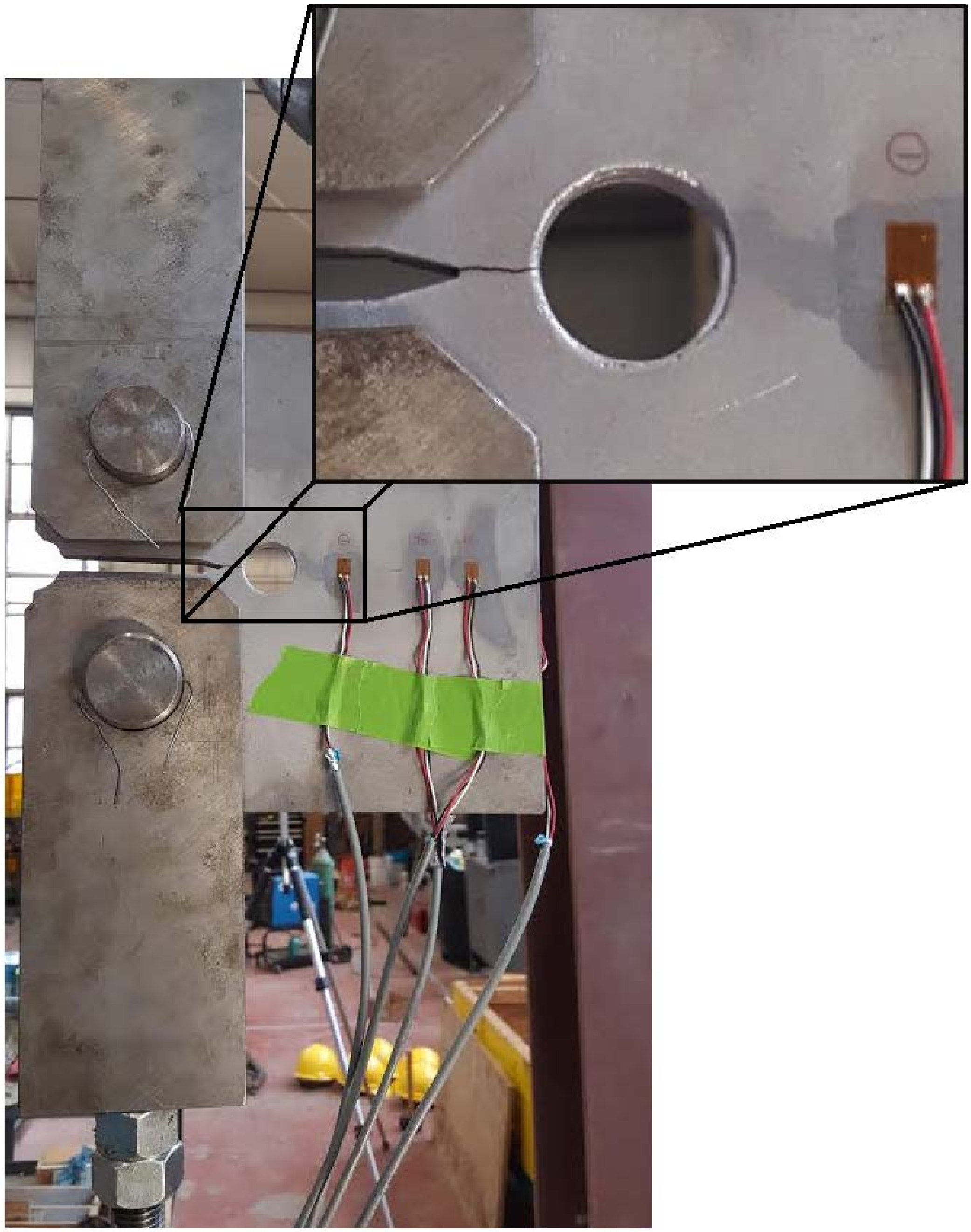

Figure E.5. Fatigue testing setup for Specimen #2.

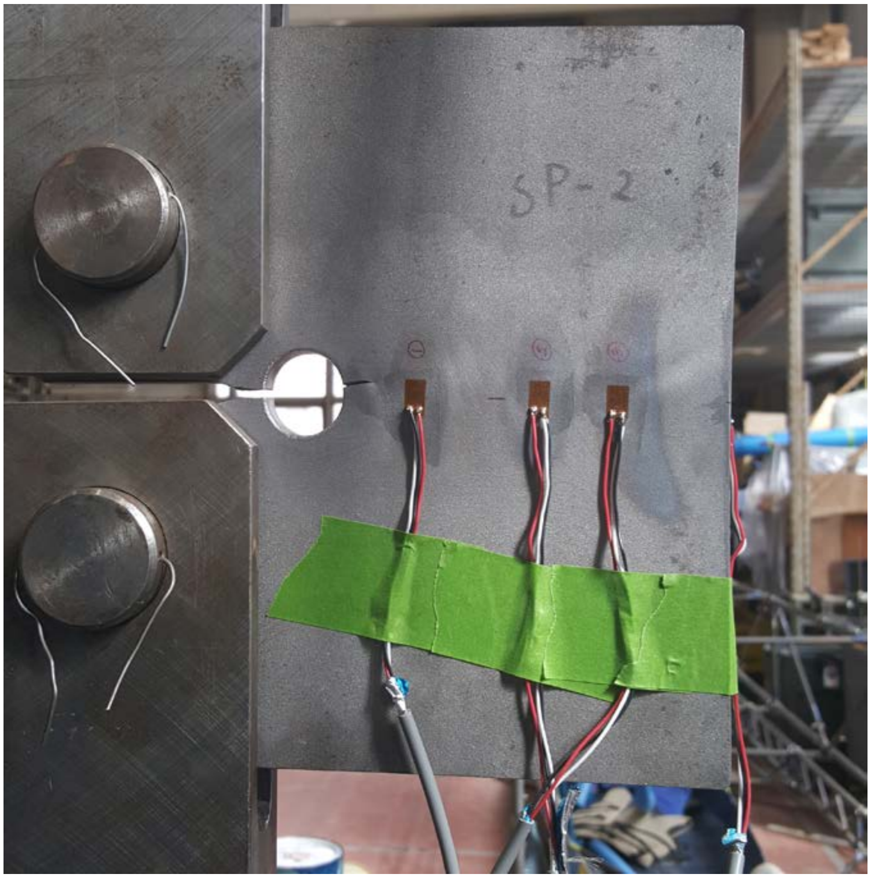

Figure E.6. Specimen #2 after about 160k-165k cycles (assuming 40-45k for pre crack).

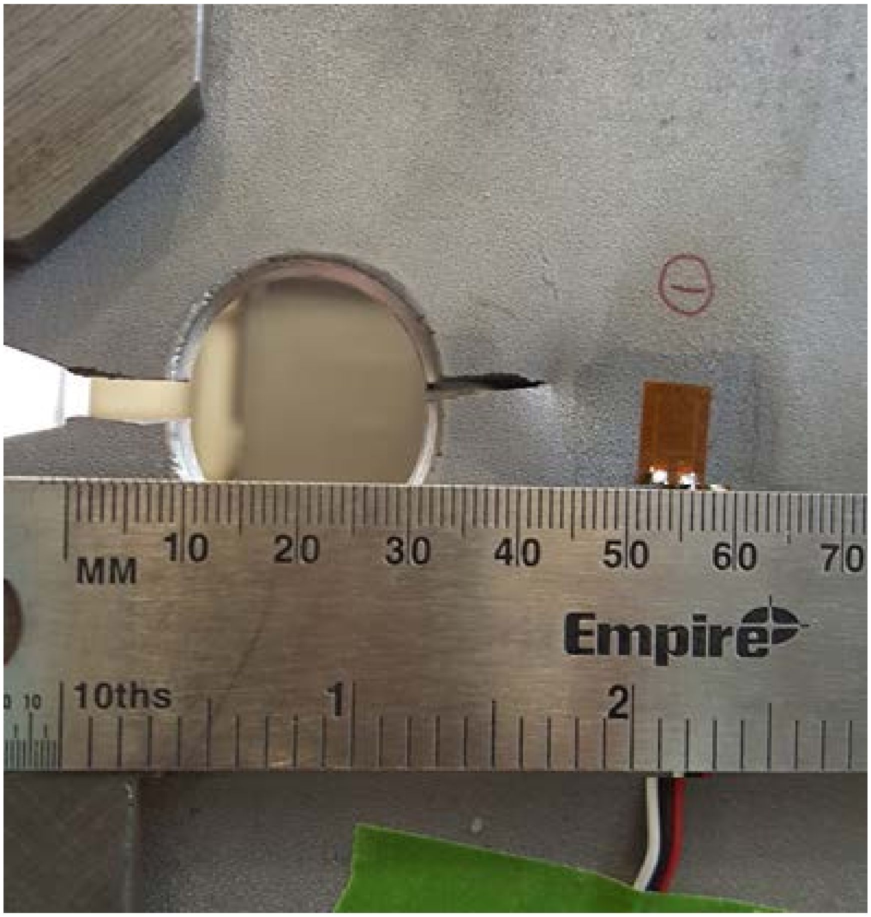

Figure E.7. Specimen #2 measurement after about 160k-165k cycles (assuming 40-45k for pre crack).

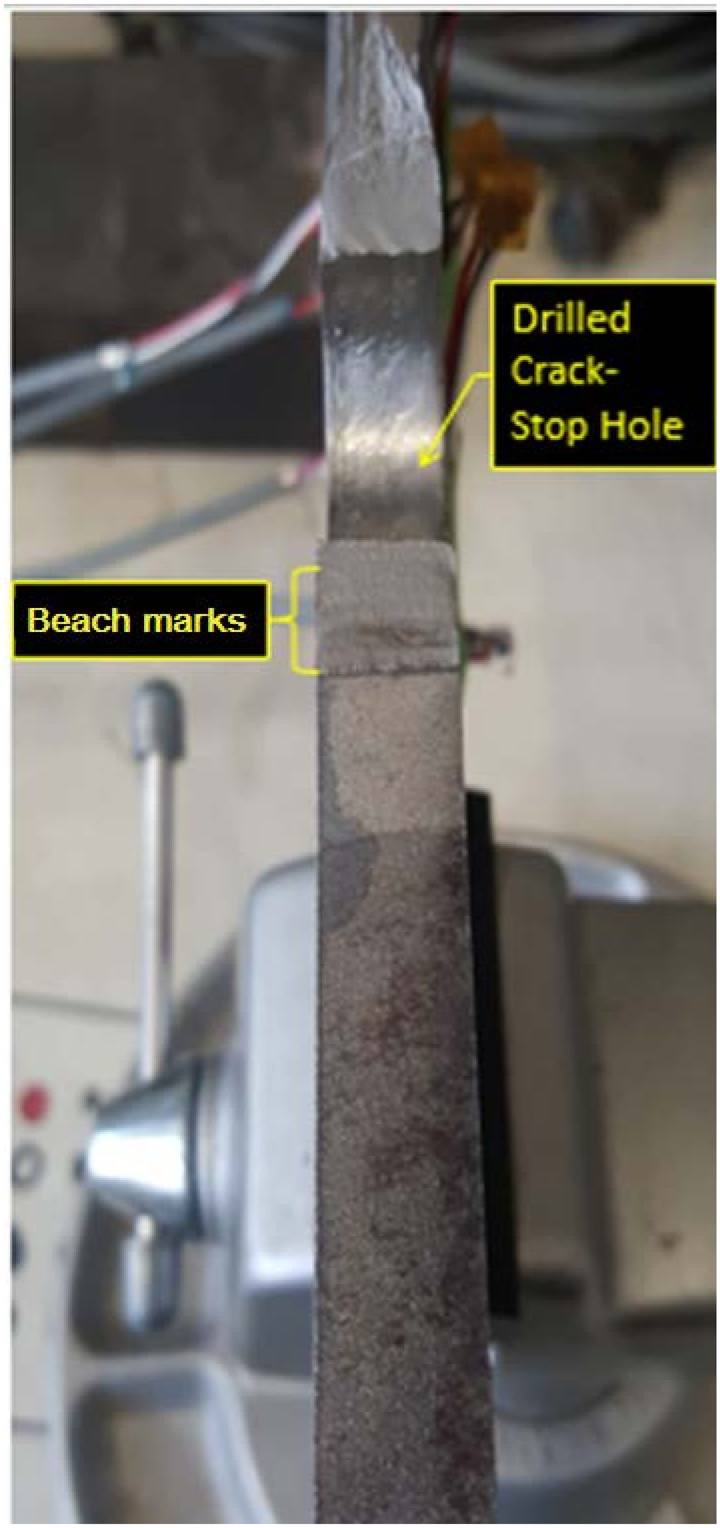

Figure E.8. Cross-section of Specimen #2 with beach marks.

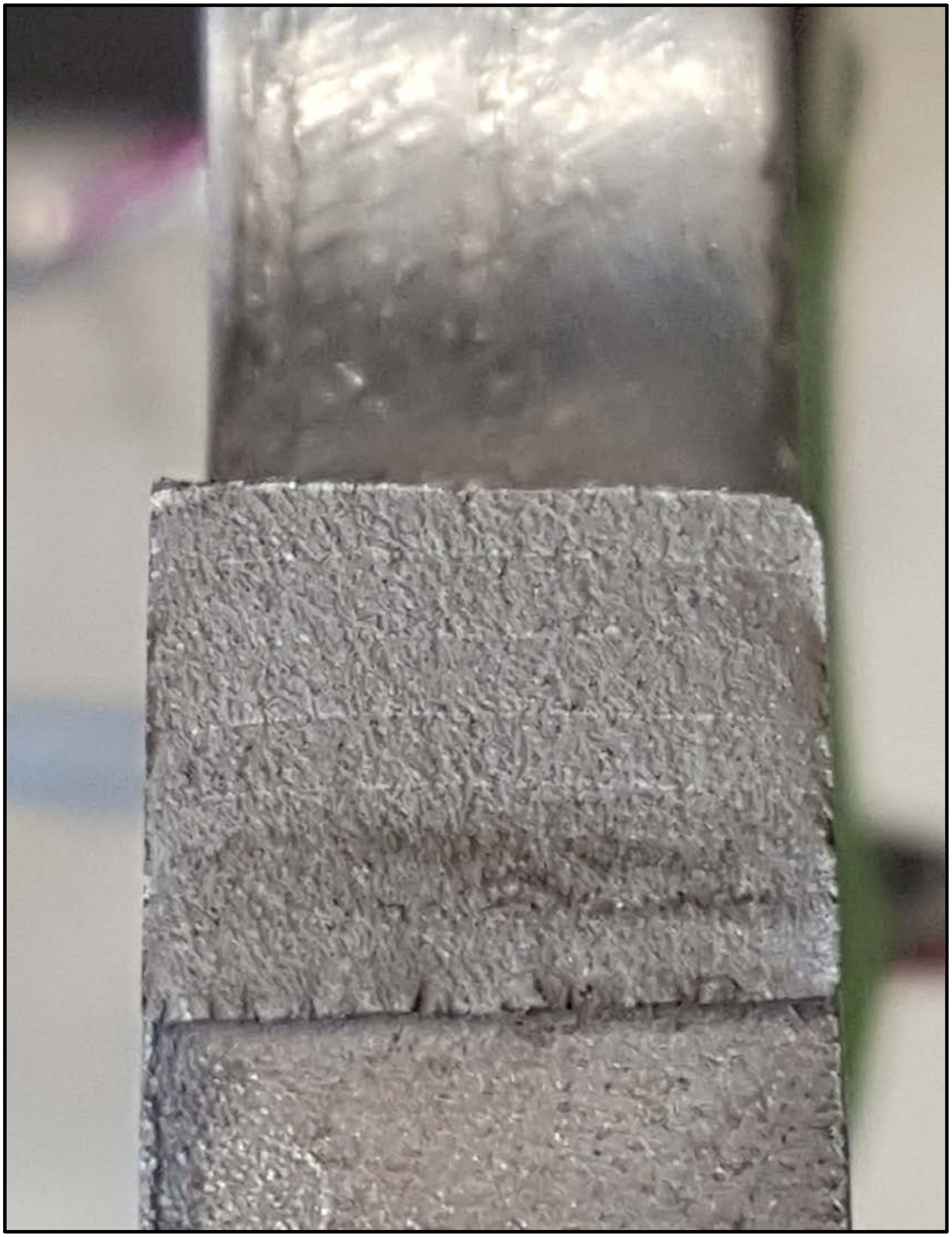

Figure E.9. Close-up view of beach marks – Specimen #2.

Figure E.10. Failed Specimen #3 from different viewing angles.

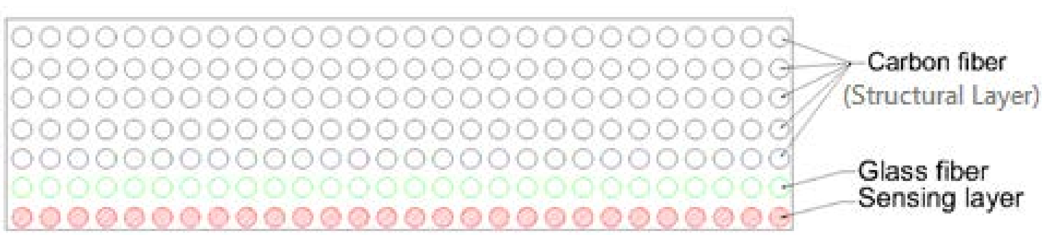

Figure E.11. General ISS composite layout.

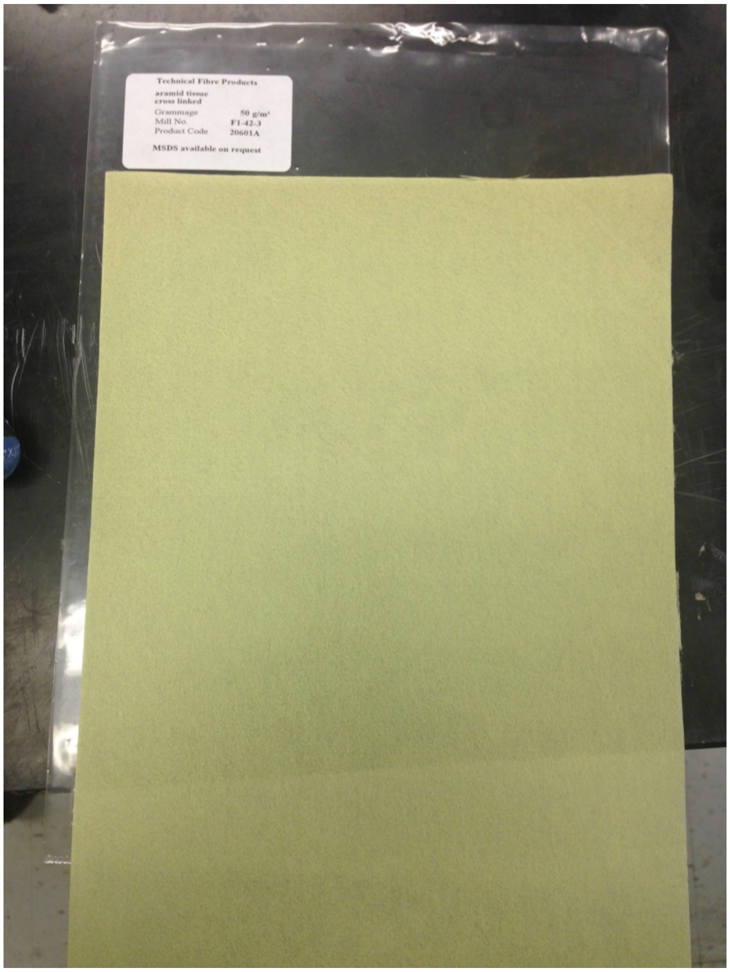

Figure E.12. Fiber sheet prior to soaking in CNT solution.

Figure E.13. CNT-infused fiber sheet.

Figure E.14. Single-ply of M40J composite.

Figure E.15. ASTM E647 steel plate after sandblasting.

Figure E.16. Two-part epoxy paste adhesive.

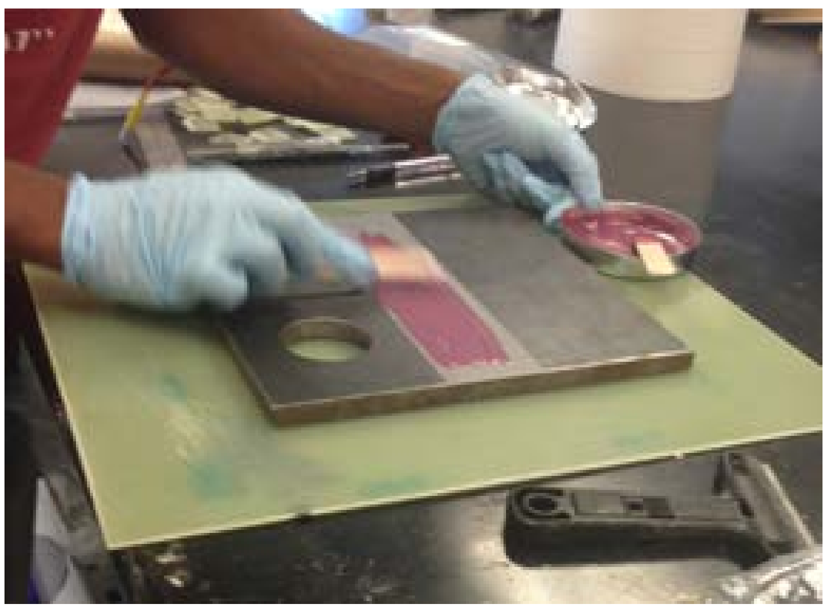

Figure E.17. Application of adhesive to steel plate.

Figure E.18. Specimen after application of adhesive.

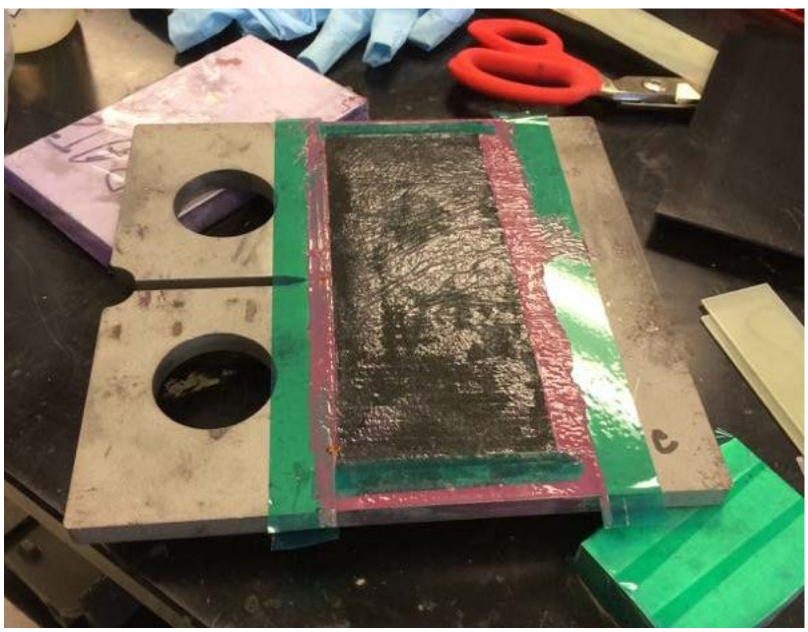

Figure E.19. Placement of CNT sensing layer onto steel specimen.

Figure E.20. Specimen in vacuum prior to placing in oven.

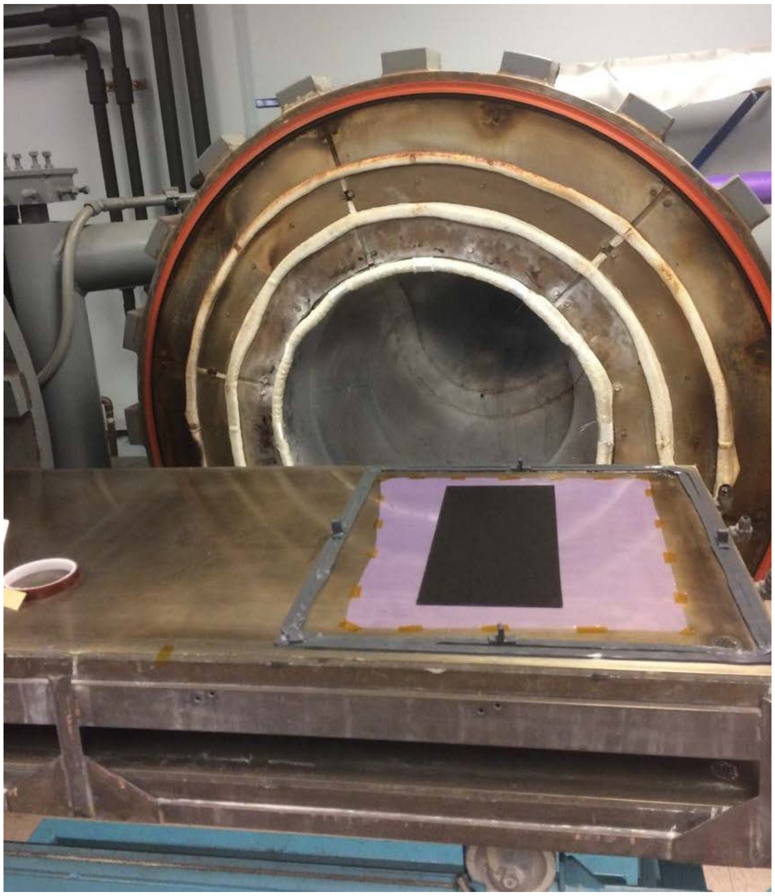

Figure E.21. Composite layer prior to placement in autoclave.

Figure E.22. Placement of composite patch into autoclave.

Delaware Center for Transportation University of Delaware Newark, Delaware 19716

AN EQUAL OPPORTUNITY/AFFIRMATIVE ACTION EMPLOYER

The University of Delaware does not discriminate on the basis of race, color, national origin, sex, disability, religion, age, veteran status, gender identity or expression, or sexual orientation, or any other characteristic protected by applicable law in its employment, educational programs and activities, admissions policies, and scholarship and loan programs as required by Title IX of the Educational Amendments of 1972, the Americans with Disabilities Act of 1990, Section 504 of the Rehabilitation Act of 1973, Title VII of the Civil Rights Act of 1964, and other applicable statutes and University policies. The University of Delaware also prohibits unlawful harassment including sexual harassment and sexual violence. Inquiries or complaints may be addressed to:

Susan L. Groff, Ed. D.
Director, Institutional Equity & Title IX Coordinator
305 Hullihen Hall
Newark, DE 19716
(302) 831-8063
titleixcoordinator@udel.edu

For complaints related to Section 504 of the Rehabilitation Act of 1973 and/or the Americans with Disabilities Act, please contact:

Anne L. Jannarone, M.Ed., Ed.S.
Director, Office of Disability Support Services
Alison Hall, Suite 130,
Newark, DE 19716
(302) 831-4643
OR contact the U.S. Department of Education - Office for Civil Rights (https://wdcrobcolp01.ed.gov/CFAPPS/OCR/contactus.cfm).

Abridged Version – with permission by Title IX coordinator (ex: rack cards, etc.)
The University of Delaware is an equal opportunity/affirmative action employer and Title IX institution. For the University's complete non-discrimination statement, please visit www.udel.edu/aboutus/legalnotices.html